UNIVERSITY OF SOUTHAMPTON

FACULTY OF ENGINEERING SCIENCE AND MATHEMATICS

School of Electronics and Computer Science

Nanoscale Systems Integration Research Group

Suppression of Boron Transient Enhanced and Thermal Diffusion in Silicon and Silicon Germanium by Fluorine Implantation

Huda Abdel Wahab Abdel Rahim El Mubarek

A thesis submitted for the degree of

Doctor of Philosophy

August 2004

UNIVERSITY OF SOUTHAMPTON

ABSTRACT

FACULTY OF ENGINEERING, SCIENCE & MATHEMATICS
SCHOOL OF ELECTRONICS AND COMPUTER SCIENCE

Doctor of Philosophy

SUPPRESSION OF BORON TRANSIENT ENHANCED AND THERMAL DIFFUSION IN SILICON AND SILICON GERMANIUM BY FLUORINE IMPLANTATION

By Huda Abdel Wahab Abdel Rahim El Mubarek

In this thesis a study is made of the growth of buried boron marker layers with sharp and narrow boron profiles and of the effect of fluorine implantation on the diffusion of boron in buried marker layers in silicon and silicon germanium.

Initial experiments investigate the effect of varying F^+ implantation energy on boron thermal diffusion and boron transient enhanced diffusion (TED) in $Si_{1-x}Ge_x$. In samples implanted with 185keV F^+, the fluorine suppresses boron transient enhanced diffusion completely and suppresses thermal diffusion, whereas in samples implanted with 42keV F^+, the fluorine does not reduce boron transient enhanced diffusion. These results indicate that a high energy F^+ implant is much more effective than a low energy implant for suppressing boron diffusion.

The effect of F^+ implantation dose on the diffusion of boron in silicon and silicon germanium is then studied. In silicon samples implanted with P^+ and $2.3\times10^{15}cm^{-2}$ F^+, the fluorine completely suppresses boron transient enhanced diffusion. Reduction of boron thermal diffusion is observed for F^+ doses at and above a dose of $1.4\times10^{15}cm^{-2}$. In $Si_{1-x}Ge_x$ a reduction of boron thermal diffusion is observed for F^+ doses at and above a dose of $9\times10^{14}cm^{-2}$, whereas a suppression of boron transient enhanced diffusion is observed for all F^+ doses. For F^+ doses of $1.4\times10^{15}cm^{-2}$ and $2.3\times10^{15}cm^{-2}$ the fluorine reduces the boron thermal diffusion coefficient by factors of 1.9 and 3.7 in silicon and factors of 2.5 and 3.5 in $Si_{1-x}Ge_x$ respectively. The reduction of boron thermal diffusion correlates with the appearance of shallow fluorine peaks in the silicon and $Si_{1-x}Ge_x$ layers at and above the critical doses of $1.4\times10^{15}cm^{-2}$ and $9\times10^{14}cm^{-2}$ respectively. These shallow fluorine peaks are present in samples with and without boron marker layers in both silicon and $Si_{1-x}Ge_x$ and hence are not due to a chemical interaction between the fluorine and boron.

Transmission electron microscopy (TEM) micrographs show that there are no extended defects in both the silicon and $Si_{1-x}Ge_x$ layers, and hence it is proposed that the shallow fluorine peaks are due to vacancy-fluorine clusters. The reduction in boron thermal diffusion above the critical F^+ dose is then explained by the presence of the vacancy-fluorine clusters, which suppress the interstitial concentration in the silicon and $Si_{1-x}Ge_x$ layers. The suppression of boron transient enhanced diffusion correlates with a deep fluorine peak around the range of the fluorine implant and TEM micrographs show that this peak is due to a band of dislocation loops. The suppression of TED by fluorine is then explained by the influence of the loops in suppressing the backflow of interstitials to the surface. Analysis of the SIMS profiles shows that fluorine is transported from the adjacent silicon into the $Si_{1-x}Ge_x$ layer during anneal, and reaches concentrations that are much higher than observed after implant. This mechanism would give benefits in devices like $Si_{1-x}Ge_x$ heterojunction bipolar transistors (HBTs), since a high fluorine concentration is automatically obtained in the vicinity of the boron profile, which maximises the effect of fluorine in suppressing boron diffusion.

Contents

Acknowledgements

This work wouldn't have been possible without the help of numerous people. I hope that in these few lines I am able to thank them all.

The greatest contribution by far is from my supervisor and teacher Professor Peter Ashburn. My journey with him started many years ago; starting from first year circuit theory through to my final year project and finally to Ph.D. I have learnt a lot from you throughout the years, more than I can list in these lines, but I hope this thesis is a small manifestation of that. Thank you for everything; for giving me this wonderful opportunity of learning and for your support and encouragement throughout its duration. Most of all thank you for teaching me one very important lesson: "*Engineers Must Write*!"

Thank you to Dr. Janet Bonar for teaching me many things and most importantly the running of Epi 1! Thank you to Professor Arthur Willoughby for many useful and enlightening discussions. Thank you to Dr. Mudith Karunaratne for teaching me the ins and out of modelling. Thank you to Dr. Michèle Mitchell who helped me settle in and get started in my first year of Ph. D. Thank you to all the cleanroom staff from whom I learnt a lot about processing. Thank you to Jean for being the first to suggest that I should do a Ph. D. Thank you to all my fellow research students and to all the academic staff and to our wonderful secretaries for providing a great working atmosphere.

Thank you to all my friends for being my family away from my family and making me feel home away from home. Thank you for being there at all times; supporting me, feeding me, encouraging me, believing in me and keeping my company in the long working nights. Without all of you I could have never reached this stage. Thank you all very much indeed.

Thank you to all my family back home and to all my brothers and sisters for believing in me and for being there for me. Thank you for your prayers and for your unfailing support and encouragement. Thank you to my elder sister for walking this marathon first with great stride and resilience, I am but only trying to follow in your path.

Last but not least, all gratitude to my first teachers ever; my beloved parents. Thank you for believing in me and having such great hopes and dreams for me and for helping me reach these goals throughout the years with your everlasting care and support and prayers. It is for you that this thesis is dedicated, for it is the fruit of your nourishment through out the years.

For my beloved parents

First and last all gratitude is to Allah Whom created me and taught me that which I did not know.

In the name of Allah the Most Gracious, the Most Merciful

"Read In the Name of your Lord Who has created (1). He has created man from a clot (2). Read and your Lord is the Most Generous (3).Who has taught by the pen (4). He has taught man that which he knew not (5)."

The Holy Quran: Surah Al-Alaq
(The clot) verses 1-5.

Chapter 1

Introduction

The growth of n-type Si, p-type $Si_{1-x}Ge_x$ and n-type Si layers is needed for the formation of NPN $Si_{1-x}Ge_x$ heterojunction bipolar transistor layers. The growth of these three layers in the same epitaxial step has two main advantages for devices. First, eliminating the requirement for a separate collector epitaxy step and hence reducing the cost and time of processing. Second, the growth interface is buried deep in the collector layer away from the base depletion regions. The dual control of n- and p-type dopants in the same growth step is challenging and requires careful control of the growth parameters in order to control the dopant profiles.

In this thesis (chapter 3) describes the growth of n-type Si, p-type $Si_{1-x}Ge_x$ and n-type Si layers in a single epitaxy step for use in a non-selective $Si_{1-x}Ge_x$ heterojunction bipolar transistor growth process at 700°C. A process is developed to eliminate the edge from the boron profile in the $Si_{1-x}Ge_x$ layer by interrupting the growth with a hydrogen anneal in between the growth of the Si_{1-x} Ge_x and the Si cap layers. This process gives very sharp and narrow boron profiles suitable for the base of a heterojunction bipolar transistor or boron marker layers for diffusion studies.

The minimisation of boron diffusion is vitally important in all types of Si and $Si_{1-x}Ge_x$ devices [1-3]. In NPN Si bipolar transistors and $Si_{1-x}Ge_x$ hetrojunction bipolar transistors (HBTs) the reduced boron diffusion in the base is needed to give narrow base widths and thus high cut off frequencies needed for wireless and optical communications applications [1].

In metal oxide semiconductor field effect transistors (MOSFETs) the minimisation of device dimensions in order to increase the operation speed and the component density results in undesirable effects, referred to as short channel effects. As the channel length L is reduced, the depletion layer widths of the source and drain junctions become comparable to the channel length. When the sum of the depletion layer widths of the source and drain junctions becomes equal to the channel length, punch through occurs. At punch through the two depletion layers merge and the gate loses control of the current. This effect causes a major limitation of short channel MOSFETs. Hence, it is essential to reduce the depletion layer widths of the source and drain junctions and the junction depth in short channel devices in order to reduce short channel effects and improve device performance [4]. In PMOSFETs reduced boron diffusion is required to obtain shallow source and drain junctions as well as sharp halo profiles and hence smaller geometry devices with improved short channel effects required for high density memory applications [3].

When annealing a boron implanted silicon sample at $\approx$800°C, the boron in the tail diffuses very fast $\approx$100× faster than normal thermal diffusion [5]. This enhanced diffusion lasts a while after which the boron diffusion returns to its normal rate and is thus referred to as transient enhanced diffusion (TED) [5]. Boron transient enhanced diffusion has detrimental effects on devices. For example, in $Si_{1-x}Ge_x$ HBTs transient enhanced diffusion of boron from the $Si_{1-x}Ge_x$ base creates parasitic energy barriers [2] that degrade the current gain and limit the value of cut-off frequency that can be achieved. Similarly, in MOSFETs diffusion of boron in the pocket or halo [3] has detrimental consequences on short channel effects and hence limits the scaling of MOSFETs to smaller geometries.

At high anneal temperatures TED lasts a short time and the displacement during TED is small, which implies that if very short (with high ramp rates) high temperature anneals are used TED should be suppressed [5]. The effect of high ramp rates in suppressing boron TED has been studied and shown to be largest for low energy implants [6]. However, it has been reported that this approach is only effective for low implant doses, for which most of the diffusion occurs in the ramp up stage, as the ramp down rate is limited in practice, and that for high doses high ramp up rates reduce TED in the ramp up stage but not in the ramp down stage [6]. This approach is also ineffective for high energy implants, where even when TED is reduced due to high ramp up rates the large as implanted depth obscures the effect [6].

Another approach reported to reduce TED is the use of silicon implantation, which was reported to reduce boron TED significantly both in bulk [7, 8] and SOI [7]. Almost complete suppression of boron TED in SOI substrates was reported and was attributed to the buried oxide isolation of the end of range (EOR) point defects created by the Si^+ implant from the boron layer near the surface [7]. However, this approach also has its disadvantages. Increased boron inactivity in SOI layers compared to bulk silicon has been reported recently [9].

Carbon implantation to reduce TED has been reported in the literature [10-15]. This suppression in TED was attributed to the formation of carbon related damage, which acts as a trap for silicon interstitials [11]. However, this approach also has its disadvantages. It has been reported that for carbon implanted silicon, most of the carbon atoms were not in substitutional lattice sites but formed C-Si self interstitial type complexes. These defects are neutral and reduced electron mobility through scattering mechanisms. They also introduced a band of deep donor levels (electron donating energy levels deep in the band gap further away from the conduction band)

in the band gap with ionization energies in the 0-0.3eV range, which increase leakage by acting as an intermediate electron donating level reducing the thermal energy required for electrons to jump from the valence band to the conduction band. These effects resulted in degradation of p^+-n diodes characteristics [12]. Carbon implantation resulting in enhanced carbon levels inhibiting defect dissolution and degrading electrical properties of junctions has been reported [13]. Incorporation of a buried carbon layer by carbon implantation prior to epitaxy of the $Si_{1-x}Ge_x$/Si base layer has been reported to reduce B TED in the extrinsic base region of $Si_{1-x}Ge_x$ HBTs [14]. Carbon implantation has also been reported to reduce boron TED in Ge^+ preamorphised Si bipolar junction transistors [15] resulting in a steeper base profile and a higher f_T. However, the carbon implantation also resulted in an increase in collector-base and emitter-base leakage currents and a decrease in the transistor breakdown voltage [15].

Substitutional carbon incorporation into silicon by molecular beam epitaxy was reported to suppress boron transient enhanced diffusion caused by a silicon implant fully [16]. Incorporation of a carbon rich buried layer by molecular beam epitaxy has been reported to reduce the TED of boron implanted into preamorphised silicon [17]. Incorporation of substitutional carbon by molecular beam epitaxy into $Si_{1-x}Ge_x$ layers, hence growing $Si_{1-x-y}Ge_xC_y$ layers, has been reported to suppress boron out diffusion significantly and has been used in $Si_{1-x-y}Ge_xC_y$ HBTs and shown to improve f_T and f_{max} by a factor of 2 compared to control $Si_{1-x}Ge_x$ HBTs [18]. The suppression of boron TED and the reduction in boron thermal diffusion in SiC layers compared to Si layers was attributed to the combination of carbon with Si interstitials in preference to boron and hence creating an undersaturation in silicon interstitials and suppressing boron diffusion [19, 20]. A similar explanation was also given to the

suppression of B TED and reduction in boron thermal diffusion in $Si_{1-x-y}Ge_xC_y$ layers compared to $Si_{1-x}Ge_x$ layers [21]. However, carbon incorporation into the base of $Si_{1-x-y}Ge_xC_y$ HBTs is not without disadvantages, for example increased base leakage at higher carbon concentrations [22].

One interesting and simple approach to boron TED suppression is the use of a BF_2^+ implant or a separate F^+ implant. Work on the effects of fluorine from a BF_2^+ implant showed that shallower junctions could be obtained when BF_2^+ was implanted instead of B^+ [23-25]. In later work [26-43] fluorine was implanted separately to the boron to characterise the effect of the fluorine on boron diffusion. This reported work showed that fluorine implantation reduced boron transient enhanced diffusion [26-29, 31, 33, 35, 36, 38, 40-44] and increased boron activity [26]. However, there have also been contradictory reports in the literature, which showed that fluorine implants had little or no effect on boron transient enhanced diffusion [32] and that fluorine enhanced boron diffusion in pre-amorphised silicon [37]. It is clear therefore, that further experimental work is needed to define the conditions under which a F^+ implant suppresses boron TED.

Recently, the use of a separate F^+ implant in MOSFETs was reported [39] to suppress boron TED and produce super sharp boron halo profiles. It was reported that the sharp halo profiles obtained using F^+ implantation resulted in lowered junction capacitance and improved I_{on}–I_{off} characteristics for both NMOS and PMOS transistors [39].

However, there have been no reports in the literature on the effect of fluorine on boron thermal diffusion in silicon or on the effects of fluorine on boron transient enhanced or thermal diffusion in $Si_{1-x}Ge_x$, which are essential for optimisation of boron profiles in both bipolar and MOS transistors. In this thesis the effect of fluorine

implantation energy on boron diffusion in $Si_{1-x}Ge_x$ is studied and results showing that a high energy is more effective in the suppression of boron diffusion are shown in chapter 4. The effect of fluorine implantation dose on boron thermal diffusion in silicon is studied in chapter 5. It is shown that a critical fluorine dose exists above which fluorine suppresses boron thermal diffusion and below which it has no effect. The effect of fluorine implantation dose on boron transient enhanced and thermal diffusion in silicon germanium is studied in chapter 6 and it is shown that fluorine suppresses boron transient enhanced diffusion at all doses and that a critical dose exists above which fluorine suppresses boron thermal diffusion and below which it has no effect; this dose is lower than that in silicon.

Several alternative mechanisms have been proposed in the literature to explain the effect of the fluorine on boron transient enhanced diffusion in silicon [23-38, 44]. A chemical interaction between boron and fluorine has been proposed to explain the suppression of boron transient enhanced diffusion by fluorine [28, 31, 33, 36, 44], in which the fluorine combines with interstitial boron reducing its mobility [28, 33, 36, 44] or reduces the probability of formation of a boron interstitial pair [31, 33]. Alternatively, the formation of vacancy-fluorine clusters has been proposed [35, 38, 40, 45-48], which act as a barrier for boron diffusion [35], or suppress the interstitial concentration and hence reduce boron transient enhanced diffusion in silicon [38]. Finally the interaction of fluorine with silicon interstitials has been widely proposed as a mechanism of suppressing boron transient enhanced diffusion in silicon [24-26, 28-32, 40, 43].

However, to date there is still a debate over the exact mechanism by which fluorine suppresses boron diffusion. In this thesis experiments are performed to identify the mechanisms involved in the suppression of both boron TED and thermal

diffusion in Si and $Si_{1-x}Ge_x$ by fluorine implantation. It is shown that a fluorine-boron chemical interaction can be discounted in both silicon (chapter 5) and silicon germanium (chapter 6). Different mechanisms are shown to operate for boron TED suppression and thermal diffusion reduction. First fluorine-vacancy clusters are formed which suppress the interstitial concentration in the vicinity of the boron marker layers and hence suppress boron thermal diffusion both in silicon (chapter 5) and silicon germanium (chapter 6). Secondly, stable fluorine interstitial type dislocation loops are formed due to F^+ implantation which trap interstitials and hence prevent their back flow to the surface and suppress boron transient enhanced diffusion both in silicon and silicon germanium (chapter 6).

References

1. B. Jagannathan, M. Khater, F. Pagette, J. -S. Rieh, D. Angell, H. Chen, J. Florkey, F. Golan, D. R. Greenberg, R. Groves, S. J. Jeng, J. Johnson, E. Mengistu, K. T. Schonenberg, C. M. Schabel, P. Smith, A. Stricker, D. Ahlgren, G. Freeman, K. Stein, S. Subbanna, "Self aligned SiGe npn transistors with 285GHz f_{max} and 207GHz f_T in a manufacturable technology"; IEEE Electron Device Letters, vol. 23, pp. 258-260, (2002).
2. Md. R. Hashim, R. F. Lever and P. Ashburn, "2D simulation of transient enhanced boron out-diffusion from the base of a SiGe HBT due to an extrinsic base implant"; Solid State Electronics, vol. 43, pp. 131-140, (1999).
3. M. Y. Kwong, R. Kasnavi, P. Griffin, J. D. Plummer, R. W. Dutton, "Impact of lateral source/drain abruptness on device performance"; IEEE Transactions on Electron Devices, vol. 49, pp. 1882-1890, (2002).
4. S. M. Sze, "Semiconductor Devices Physics and Technology"; John Wiley and Sons, (1985).
5. S. C. Jain, W. Schoenmaker, R. Lindsay, P. A. Stolk, S. Decoutere, M. Willander and H. E. Maes, "Transient enhanced diffusion of boron in Si"; Applied Physics Reviews, Journal of Applied Physics, vol. 91 (11), pp. 8919-8941, (2002).
6. A. Agarwal, H. -J. Gossmann and A. T. Fiory, "Ultra-Shallow Junctions by Ion Implantation and Rapid Thermal Annealing: Spike-Anneals, Ramp Rate Effects"; Materials Research Society Symposium Proceedings, vol. 568, pp. 19-30, (1999).

7. A. Nejim and B. J. Sealy, "Retarding transient enhanced diffusion of boron in silicon with high energy silicon co-implants"; Semiconductors Science and Technology, vol. 18, pp. 839-844, (2003).
8. A. Sultan, S. Banerjee, S. List, V. McNeil, "An approach using a subamorphizing threshold dose silicon implant of optimal energy to achieve shallower junctions"; Journal of Applied Physics, vol. 83 (12), pp. 8046-8050, (1998).
9. A. F. Saavedra, K. S. Jones, L. Radic, M. E. Law, K. K. Chan, "Concentration dependence of boron-interstitial cluster (BIC) formation in silicon-on-insulator (SOI)"; Materials Research Society Symposium Proceedings, vol. 810, pp. C8.11.1-C8.11.6, (2004).
10. S. Nishikawa, A. Tanaka and T. Yamaji, "Reduction of transient boron diffusion in preamorphized Si by carbon implantation"; Applied Physics Letters, vol. 60 (18), pp. 2270-2272, (1992).
11. A. Cacciato, J. G. E. Klappe, N. E. Cowern, W. Vandervost, L. P. Biro, J. S. Custer and F. W. Saris, "Dislocation formation and B transient diffusion in C coimplanted Si"; Journal of Applied Physics, vol. 79 (5), pp. 2314-2325, (1996).
12. S. Lombardo, A. Cacciato, K. K. Larsen, V. Raineri, F. la Via, V. Privitera and S. U. Campisano, "High temperature annealing effects on the electrical characteristics of C implanted Si"; Journal of Applied Physics, vol. 79 (7), pp. 3464-3469, (1996).
13. M. Craig, A. Sultan and S. Banerjee, "Carbon Co-Implantation for Ultra-Shallow P^+-N Junction Formation"; Proceedings of the International Conference on Ion Implantation Technology, pp. 665-667, (1996).

14. S. Jouan, H. Baudry, D. Dutartre, C. Fellpus, M. Laurens, D. Lenoble, M. Marty, A. Monroy, A. Perrotin, P. Ribot, G. Vincent and A. Chantre, "Investigation of the effectiveness of a buried carbon layer to suppress transient enhanced diffusion effects in SiGe HBTs"; Proceedings of the European Solid State Device Research Conference ESSDERC, pp. 556-559, (2000).

15. P. H. C Magnée, A. L. A. M. Kemmeren, N. E. B. Cowern, J. W. Slotboom, R. J. Havens and H. G. A. Huizing, "Ultra shallow boron base profile with carbon implantation"; The Bipolar/BiCMOS Circuits and Technology Meeting BCTM, pp. 64-67, (2001).

16. P. A. Stolk, D. J. Eaglesham, H. -J. Gossmann and J. M. Poate, "Carbon incorporation in silicon for suppressing interstitial-enhanced boron diffusion"; Applied Physics Letters, vol. 66 (11), pp. 1370-1372, (1995).

17. E. Napolitani, A. Coati, D. De Salvador, A. Carnera, S. Mirabella, S. Scalese and F. Priolo, "Complete suppression of the transient enhanced diffusion of B implanted in preamorphized Si by interstitial trapping in a spatially separated C-rich layer"; Materials Research Society Symposium Proceedings, vol. 717, C5.4.1-C5.4.6, (2002).

18. H. J. Osten, R. Bath, G. Fischer, B. Heinemann, D. Knoll, G. Lippert, H. Rücker, P. Schley and W. Röpke, "Carbon-containing group IV heterostructures on Si: properties and device applications"; Thin Solid Films, vol. 321, pp. 11-14, (1998).

19. H. Rücker, B. Heinemann, W. Röpke, G. Fischer, G. Lippert, H. J. Osten and R. Kurps, "Modeling the effect of carbon on boron diffusion"; International

Conference on Simulation of Semiconductor Processes and Devices, SISPAD, pp. 281-284, (1997).

20. H. Rücker, B. Heinemann, D. Bolze, D. Knoll, D. Krüger, R. Kurps, H. J. Osten, P. Schley, B. Tillack, P. Zaumseil, "Dopant diffusion in C-doped Si and SiGe: physical model and experimental verification"; Technical Digest of the International Electron Devices Meeting IEDM, pp. 345-348, (1999).
21. K. Rajendran and W. Schoenmaker, "Modeling of complete suppression of boron pout-diffusion in $Si_{1-x}Ge_x$ by carbon incorporation"; Solid State Electronics, vol. 45, pp. 229-233, (2001).
22. P. Chevalier, C. Fellous, B. Martinet, F. Leverd, F. Saguin, D. Dutartre and A. Chantre, "180GHz f_T and f_{max} self-aligned SiGeC HBT using selective epitaxial growth of the base"; Proceedings of the European Solid State Device Research Conference, pp. 299-302, (2003).
23. R.G. Wilson, "Boron, fluorine and carrier profiles for B and BF_2 implants into crystalline and amorphous Si"; Journal of Applied Physics, vol. 54 (12), pp. 6879-6889, (1983).
24. D. F. Downey, J. W. Chow, E. Ishida, K. S. Jones, "Effect of fluorine on the diffusion of boron in ion implanted silicon"; Applied Physics Letters, vol. 73 (9), pp. 1263-1265, (1998).
25. Y-J. Park and J. –J. Kim, "Fluorine implantation effect on boron diffusion in Si"; Journal of Applied Physics, vol. 85 (2), pp. 803-806, (1999).
26. K. Ohyu, T. Itoga and N. Natsuaki, "Advantages of fluorine introduction in boron implanted shallow p+/n junction formation"; Japanese Journal of Applied Physics, vol. 29, pp. 457-462, (1990).

27. D. Fan, J. M. Parks and R. J. Jaccodine, "Effect of fluorine on the diffusion of through-oxide implanted boron in silicon"; Applied Physics Letters, vol. 59 (10), pp. 1212-1214, (1991).

28. L. Y. Krasnobaev, N. M. Omelyanovskaya, V. V. Makarov, "The effect of fluorine on the redistribution of boron in ion implanted silicon"; Journal of Applied Physics, vol. 74 (10), pp. 6020-6022, (1993).

29. T. H. Huang, H. Kinoshita, D. L. Kwong, "Influence of fluorine preamorphization on the diffusion and activation of low energy implanted boron during rapid thermal annealing"; Applied Physics Letters, vol. 65 (14), pp. 1829-1831, (1994).

30. H. -H. Vuong, H. -J. Gossmann, C. S. Rafferty, H. S. Luftman, F. C. Unterwald, D. C. Jacobson, R. E. Ahrens, T. Boone, P. M. Zeitzoff, "Influence of fluorine implant on boron diffusion: determination of process modelling parameters"; Journal of Applied Physics, vol. 77 (7), pp. 3056-3060, (1995).

31. J. Liu, D. F. Downey, K. S. Jones and E. Ishida, "Fluorine effect on boron diffusion: chemical or damage?"; Proceedings of the International Conference on Ion Implantation Technology, vol. 2, pp. 951-954, (1999).

32. E. Ishida, D. F. Downey, K. S. Jones and J. Liu, "The chemical effect of fluorine on boron transient enhanced diffusion"; Proceedings of the International Conference on Ion Implantation Technology, vol. 2, pp. 909-912, (1999).

33. L. S. Robertson, P. N. Warnes, K. S. Jones, S. K. Earles, M. E. Law, D. F. Downey, S. Falk and J. Liu, "Junction depth reduction of ion implanted boron in silicon through fluorine ion implantation"; Materials Research Society Symposium Proceedings, vol. 610, pp. B4.2.1-B4.2.6, (2000).

34. N. Ohno, T. Hara, Y. Matsunaga, M. I. Current, M. Inoue, "Diffusion of ion implanted boron impurities into pre-amorphised silicon"; Materials Science in Semiconductor Processing; vol. 3, pp. 221-225, (2000).

35. T.S. Shano, R. Kim, T. Hirose, Y. Furuta, H. Tsuji, M. Furuhashi and K. Taniguchi, "Realization of ultra-shallow junction: suppressed boron diffusion and activation by optimised fluorine co-implantation"; Technical Digest of the International Electron Devices Meeting IEDM, pp. 37.4.1-37.4.4, (2001).

36. A. Mokhberi, R. Kasnavi, P. B. Griffin, J. D. Plummer, "Fluorine interaction with point defects, boron and arsenic in ion implanted Si"; Applied Physics Letters, vol. 80 (19), pp. 3530-3532, (2002).

37. J. M. Jacques, L. S. Robertson, K. S. Jones, J. Bennett and M. Rendon, "Effect of fluorine on the diffusion of boron in amorphous silicon"; Materials Research Society Symposium Proceedings; vol. 717, pp. C4.6.1-C4.6.6, (2002).

38. M. Diebel, S. Chakravarthi, C. F. Machala, S. Ekbote, A. Jain and S. T. Dunham, "Investigation and modelling of fluorine co-implantation effects on dopant redistribution"; Materials Research Society Symposium Proceedings, vol. 765, pp. D6.15.1-D6.15.6, (2003).

39. K. Liu, J. Wu, J. Chen, A. Jain, "Fluorine assisted super-halo for sub-50nm transistors"; IEEE Electron Device Letters; vol. 24, pp. 180-182, (2003).

40. G. Impellizzeri, J. H. R. dos Santos, S. Mirabella and F. Priolo, E. Napolitani and A. Carnera, "Role of fluorine in suppressing boron transient enhanced diffusion in preamorphized Si"; Applied Physics Letters, vol. 84 (11), pp. 1862-1864, (2004).

41. A. Halimaoui, J. M. Hartmann, C. Laviron, R. El-Farhane and F. Laugier, "Investigation of fluorine effect on the boron diffusion by mean of boron redistribution in shallow delta-doped layers"; Materials Research Society Symposium Proceedings, vol. 810, pp. C3.10.1-C3.10.6, (2004).

42. H. Graoui, M. Hilkene, B. McComb, M. Castle, S. Felch, N. E. B. Cowern, A. Al-Bayati, A. Tajandra and M. A. Foad, "Optimization of fluorine co-implantation for PMOS source and drain extension formation to meet the 65nm technology node"; Materials Research Society Symposium Proceedings, vol. 810, pp. C5.8.1-C5.8.6, (2004).

43. G. Impellizzeri, J. H. R. dos Santos, S. Mirabella, F. Priolo, E. Napolitani and A. Carnera, "Suppression of Boron transient enhanced diffusion by fluorine in preamorphized Silicon"; Materials Research Society Symposium Proceedings, vol. 810, pp. C5.9.1-C5.9.6, (2004).

44. A. Dusch, J. Marcon, K. Masmoudi, K. Ketata, F. Olivie, M. Benzohra and M. Ketata, "Influence of fluorine on the simulation of the transient enhanced diffusion of 15keV BF_2^+ ion implantation into silicon"; Nuclear Instruments and Methods in Physics Research B; vol. 186, pp. 360-365, (2002).

45. H. Fukutome, Y. Morniyama, H. Nakao, T. Aoyama, H. Arimoto, "Fluorine implantation impact in extension region on the electrical performance of sub-50nm P-MOSFETS"; Technical Digest of the International Electron Devices Meeting, pp. 20.2.1-20.2.4, (2003).

46. X. D. Pi, C. P. Burrows and P. G. Coleman, "Fluorine in silicon: diffusion, trapping and precipitation"; Physical Review Letters, vol. 90 (15), pp.155901-1 - 155901-4, (2003).

47. R. R. Robinson, M. E. Law, "Fluorine diffusion: models and experiments"; Technical Digest International Electron Devices Meeting, pp. 883-886, (2002).

48. M. Diebel and S. T. Dunham, "Ab-initio calculations to model anomalous fluorine behaviour"; Materials Research Society Symposium Proceedings, vol. 717, pp. C4.5.1-C4.5.6, (2002).

Chapter 2

Theory

2.1 Material Properties of $Si_{1-x}Ge_x$ layers: Lattice Constant and Critical thickness

$Si_{1-x}Ge_x$ is an alloy of Si and Ge. The material properties of a $Si_{1-x}Ge_x$ layer, such as the lattice constant and bandgap, vary with the germanium content in the layer. The lattice constant of germanium is larger than that of silicon by 4.17% [1]. When a $Si_{1-x}Ge_x$ layer is grown over a silicon substrate, which has a smaller lattice constant, the two layers adjust to bond together and the deposited $Si_{1-x}Ge_x$ layer is strained. There is considerable elastic strain stored in the deposited $Si_{1-x}Ge_x$ layer which is forced to adopt the lattice constant of the underlying silicon substrate. At a characteristic layer thickness termed the critical thickness h_c it becomes energetically favourable for interfacial dislocations to relax towards its bulk lattice parameters [2].

If the grown $Si_{1-x}Ge_x$ layer thickness is less than a critical thickness h_c, then the layers are biaxially compressed, strained, with no defects created as shown in figure 2.1(a). The $Si_{1-x}Ge_x$ layer formed is called a pseudomorphic layer. If the grown $Si_{1-x}Ge_x$ layer thickness is greater than the critical thickness h_c, then the larger volume is accommodated by a slip of the lattice plane as shown in figure 2.1(b). The lattice then relaxes and a misfit dislocation is formed as shown in figure 2.1(c).

The critical thickness of the $Si_{1-x}Ge_x$ grown layer varies with the germanium concentration in the layer. The growth of a Si cap layer above the $Si_{1-x}Ge_x$ layer doubles the critical thickness in comparison with uncapped layers [1]. The critical

thickness of $Si_{1-x}Ge_x$ super-lattices grown by Ultra High Vacuum Chemical Vapour Deposition (UHV CVD) at 750°C has been measured experimentally by Kasper and Herzog [2]. Figure 2.2 shows the critical thickness versus germanium percentage graph plotted using the data of Kasper and Herzog [3]. The critical thickness decreases as the germanium percentage increases. The critical thickness for a $Si_{1-x}Ge_x$ layer with 10% Ge is 60nm from this graph.

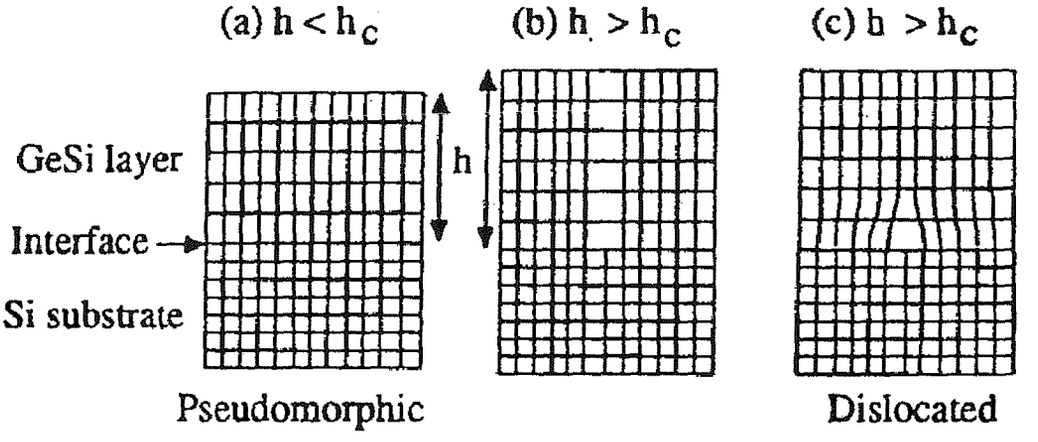

Figure 2.1: An Illustration of the lattice structures of $Si_{1-x}Ge_x$ layers, grown on a Si substrate: (a) $h<h_c$ a pseudomorphic $Si_{1-x}Ge_x$ layer, (b) $h>h_c$ a slip of the lattice plane and (c) $h>h_c$ formation of a dislocation, after S.C Jain [1].

2.2 Basic Diffusion Theory

One of the main challenges in designing a semiconductor device is the accurate control of active dopants regions. Dopant diffusion is a consequence of thermal processing stages used in semiconductor processing. Hence, a good understanding of dopant diffusion is needed in order to design front–end devices.

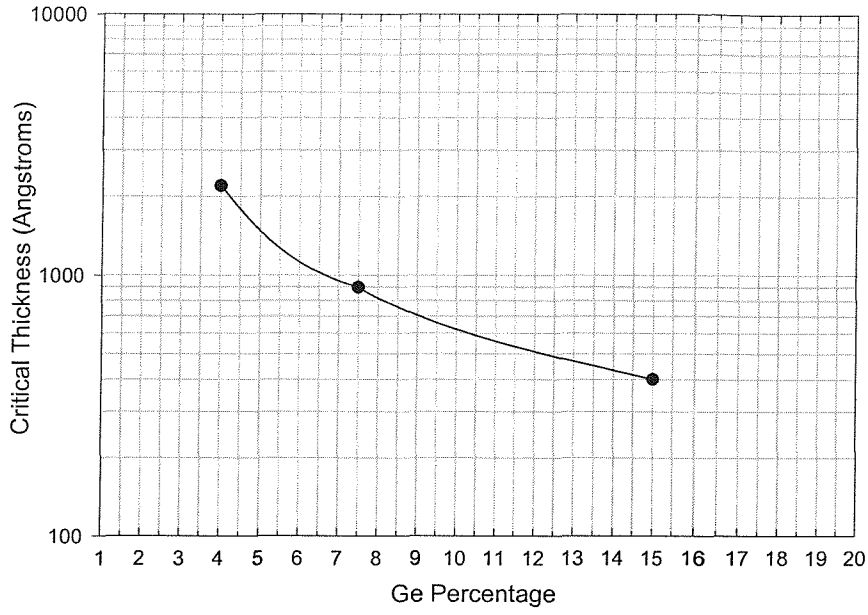

Figure 2.2: Critical Thickness versus Ge percentage content obtained experimentally for $Si_{1-x}Ge_x$ layers grown at 750°C by UHV CVD after Kasper and Herzog [3].

2.2.1 Fick's First Law

One of the simplest theories describing dopant diffusion is Fick's first law which is mathematically described in (equation 2.1) [4].

$$F = -D\frac{\partial C}{\partial x} \tag{2.1}$$

Where F is the flux (atoms $cm^{-2}sec^{-1}$), D is the diffusivity ($cm^{-2}sec^{-1}$) and $\partial C/\partial x$ is the concentration gradient. This law says that there will be a flow of material due to the concentration variation, with material flowing from higher concentration regions to low concentration regions. This law also states that the flow is proportional to the

concentration gradient, such that if there is no difference in concentration ($\frac{\partial C}{\partial x} = 0$) there is no flow ($F = 0$).

2.2.2 Fick's Second Law

A more useful description of dopant diffusion is Fick's second law, which relates the concentration to both time and space variables. It is a fundamental conservation law for matter, mathematically described in equation 2.2 [4].

$$\frac{\partial C}{\partial t} = \frac{\partial}{\partial x}\left(D\frac{\partial C}{\partial x}\right) \tag{2.2}$$

2.2.3 Delta Layer Solution of Fick's Second Law

Considering the case where we introduce a dopant marker layer in the centre of a lightly doped region, such as obtained via epitaxy, which approximates a delta function as shown in figure 2.3 [4].

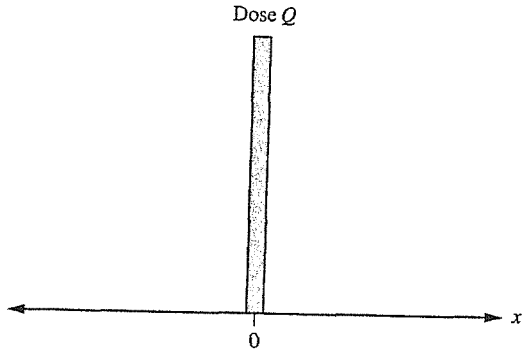

Figure 2.3: A dopant with a dose Q in the form of a delta function before and after diffusion after [4].

Taking the origin at the peak of the delta function, the boundary conditions are:

$$C \rightarrow 0 \text{ as } t \rightarrow 0 \text{ for } x > 0$$

$$C \rightarrow \infty \text{ as } t \rightarrow 0 \text{ for } x = 0 \tag{2.3}$$

and $$\int_{-\infty}^{\infty} C(x,t)dx = Q \tag{2.4}$$

where Q is the total dose of the dopant contained in the profile. The solution of Fick's second law which satisfies these boundary conditions is given by equation 2.5.

$$C(x,t) = \frac{Q}{2\sqrt{\pi Dt}} \exp\left(-\frac{x^2}{4Dt}\right) = C(0,t)\exp\left(-\frac{x^2}{4Dt}\right) \tag{2.5}$$

This equation describes a Gaussian profile, which is symmetrical about the origin and evolves with time retaining the same Gaussian form. The time evolution of a Gaussian profile is plotted in figure 2.4 on both linear (a) and logarithmic (b) scales. The point at which the surface concentration falls by 1/e is at a distance $x = 2\sqrt{Dt}$ from the origin as is easily seen by substituting $x = 2\sqrt{Dt}$ in equation 2.5. The factor $x = 2\sqrt{Dt}$ is a convenient measure of the extent of diffusion of a profile and is often referred to as the diffusion length. Ion implanted profiles are, to the first order, Gaussian profiles and dopant marker layers grown by epitaxy can be approximately represented by delta functions and hence equation 2.5 can often be used to make approximate predictions of the evolution of such profiles during thermal treatment cycles.

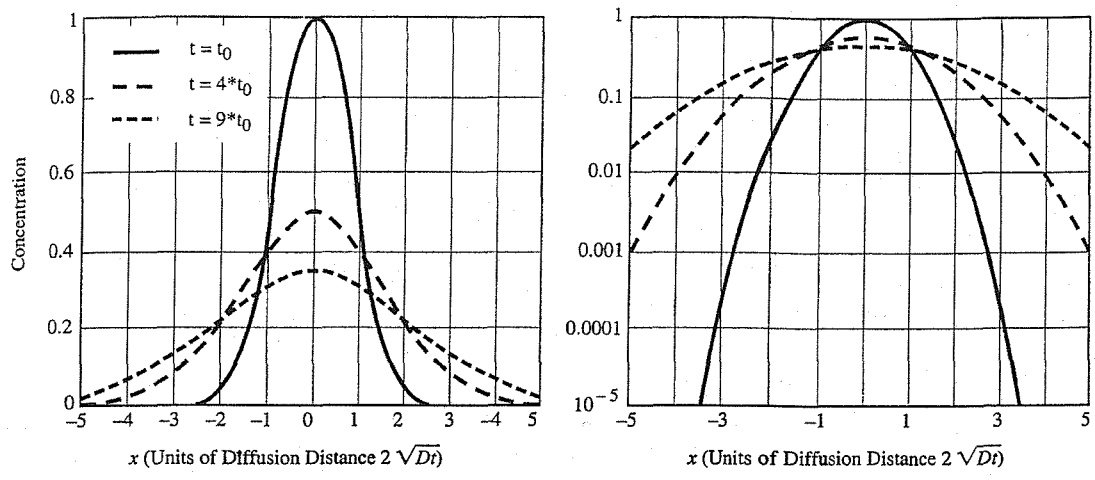

(a) (b)

Figure 2.4: Time evolution of a Gaussian diffusion profile (a) linear scale, (b) logarithmic scale after [4].

2.3 Atomistic Diffusion Mechanisms

In order to progress further we need to understand more about how dopants diffuse in an atomic scale. The understanding of atomic scale diffusion forms the physical basis of the models used in most process simulation programs used today.

Point defects and dopant diffusion are closely linked in an atomic scale. Point defects are either intrinsic or extrinsic. Intrinsic point defects occur when the lattice atoms leave their regular lattice sites during continuous vibrations around their equilibrium lattice positions. An absence of an atom from a regular lattice site is called a vacancy (V) and the presence of a self atom out of a regular lattice site is called a self interstitial (I) as shown in figure 2.5. A pair of vacancy and self interstitial is called a *Frenkel pair* and can be easily annihilated due to thermally activated movement. The intrinsic point defects may also exist in various charge states by acquiring or losing electrons. However, the probability of point defects having a

charge state higher than two is small. Extrinsic point defects occur when impurities or dopants are introduced in the lattice such as by ion implantation. These impurity or dopant atoms can occupy either regular lattice sites (substitutional) or interstitial sites. They can be easily ionised and can interact with native defects in the lattice, known as *coloumbic interaction*, forming defect-dopant complexes which affect diffusion.

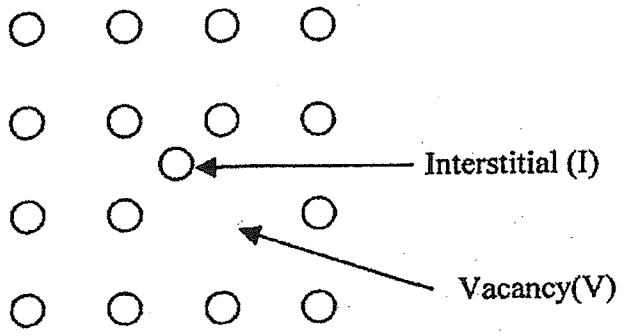

Figure 2.5: Intrinsic point defects in a crystal lattice after [5].

2.3.1 Direct Diffusion Mechanisms

Atomistic diffusion mechanisms have been classified as direct and indirect according to whether or not they require intrinsic point defects to diffuse [6]. In the simplest case of an ideal crystal where all the lattice sites are occupied, the only method by which they can diffuse is if they exchange their positions. This mechanism is referred to as *direct exchange mechanism* and requires a high energy due to the lattice distortion associated with it and is hence less probable. See (1) in figure 2.6 for an illustration of this mechanism.

Atoms which have interstitial equilibrium positions can jump from one interstice to another this is referred to as an *interstitial mechanism*. Atoms which diffuse via this mechanism diffuse very fast as the process requires small amount of

energy and the probability of a jump site being empty is very high. See (2) in figure 2.6 for an illustration of this mechanism.

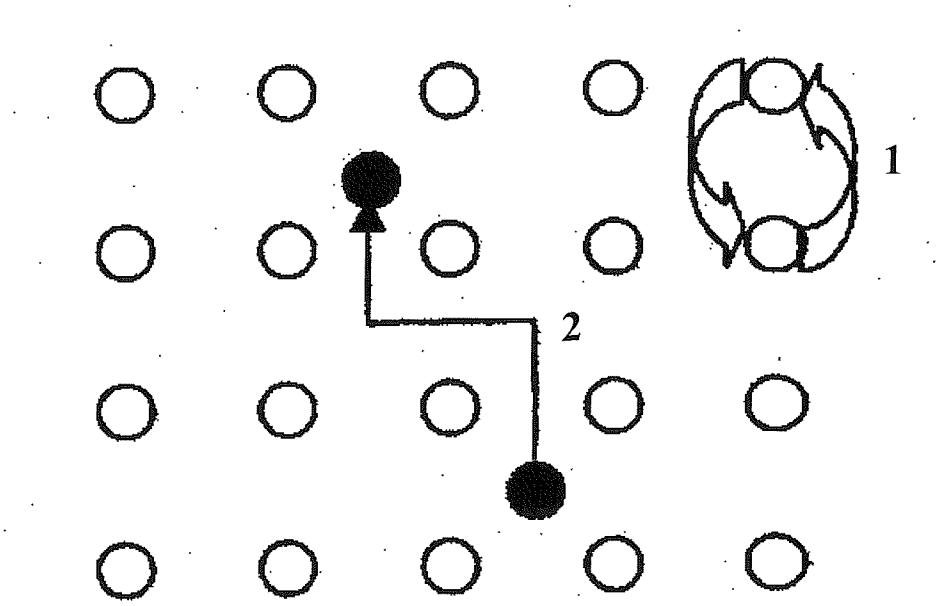

Figure 2.6: Direct diffusion mechanisms; (1) direct exchange mechanism, (2) interstitial mechanism after [5].

2.3.2 Indirect Diffusion Mechanisms

Indirect diffusion mechanisms require intrinsic defects as vehicles. One of these mechanisms is the *Vacancy mechanism* as illustrated in figure 2.7. A vacancy mechanism occurs when a substitutional self or impurity atom jumps to an adjacent vacant lattice site. This mechanism involves only one atom and is thus energetically favoured to the direct exchange mechanism.

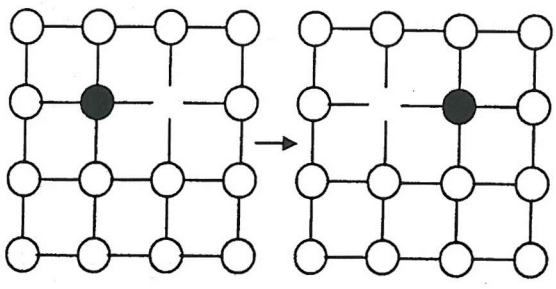

Figure 2.7: A Schematic of a vacancy mediated diffusion mechanism after [7].

Another is the *interstitialcy mechanism*, which occurs when a dopant atom and a self atom share a lattice site and jump as a pair from one interstitial position to another. The difference between this mechanism and the previous *interstitial mechanism* is that this mechanism unlike the previous one involves the pairing of a dopant with a self interstitial. This mechanism is illustrated in figure 2.8 (a).

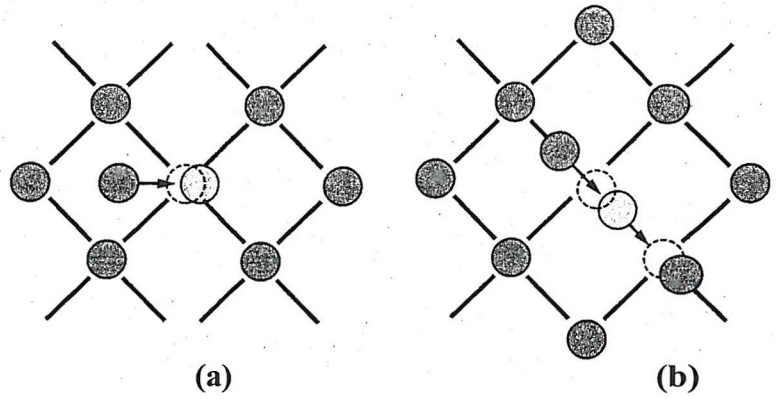

Figure 2.8: A schematic illustration of the *interstitialcy* (a) and *kick out* (b) diffusion mechanisms after [4].

Finally the *kick out mechanism* occurs when a self interstitial kicks out a dopant from a substitutional lattice site to an interstitial site after which the dopant atom diffuses quickly through interstitial sites until it finally resides in a substitutional site by kicking out a self atom from its position as illustrated in figure 2.8 (b).

A summarised illustration of the possible indirect diffusion mechanisms of an impurity atom after [8] is shown in figure 2.9. The mechanism shown in figure 2.9 (a) is the *vacancy assisted mechanism*, when a substitutional impurity atom combines with a vacancy forming a pair as described by equation 2.6.

$$A_s + V \Leftrightarrow AV \tag{2.6}$$

The mechanism shown in figure 2.9 (b) is the *interstitialcy mechanism* when a substitutional impurity atom combines with a self interstitial forming a pair as described by equation 2.7.

$$A_s + I \Leftrightarrow AI \tag{2.7}$$

The mechanism shown in figure 2.9 (c) is the *kick out mechanism* in which the substitutional impurity atom is kicked out by a self interstitial into an interstitial position as described by equation 2.8.

$$A_s + I \Leftrightarrow A_I \tag{2.8}$$

Finally the mechanism illustrated in figure 2.9(d) is the *dissociative or Frank-Turnbull mechanism* in which a substitutional impurity atom dissociates forming a vacancy and an interstitial impurity atom as described by equation 2.9

$$A_s \Leftrightarrow A_I + V \tag{2.9}$$

The diffusion of boron and phosphorus in silicon is believed to be mainly via interstitial mediated mechanisms [4].

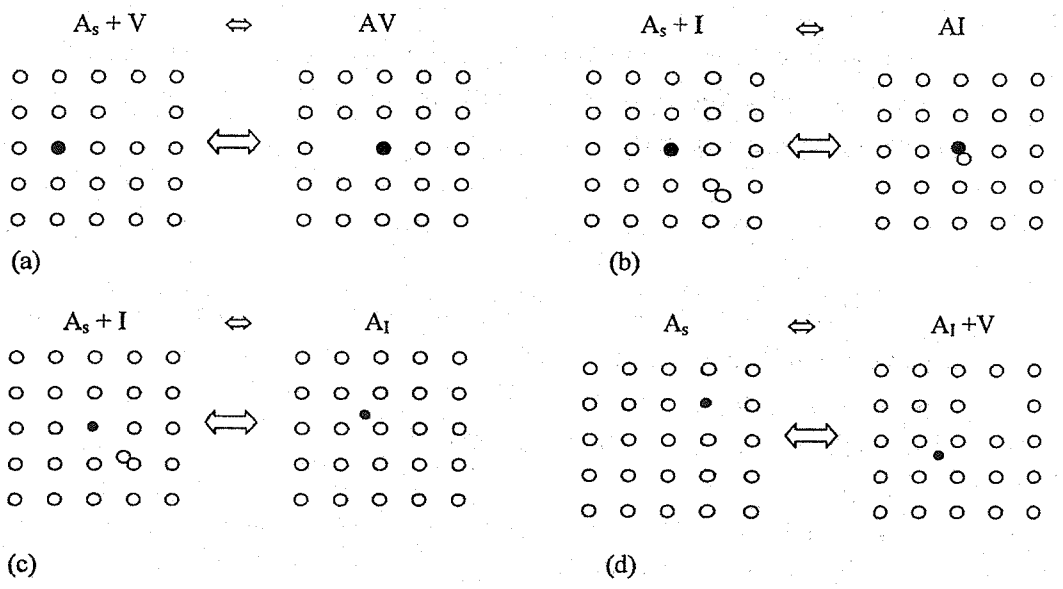

Figure 2.9: A schematic summarising indirect dopant diffusion mechanisms in silicon after [8]: (a) *vacancy assisted mechanism*, (b) *interstitialcy mechanism*, (c) *kick out mechanism* and (d) *dissociative or Frank-Turnbull mechanism*.

2.4 Boron Transient Enhanced Diffusion in Silicon

If an excess concentration (supersaturation) of Si self-interstitials is present in a silicon layer, diffusion of both boron and phosphorus in this layer is enhanced [8]. These excess interstitials can be induced by implanting Si with Si^+ or with dopant ions or by oxidation of the Si surface [8]. A self interstitial I reacts with a substitutional boron atom A_s to form a highly mobile complex B-I or to kick out the boron atom to a mobile interstitial position A_I [8]. After the interstitial boron atom A_I or the B-I pair migrates a few lattice sites the boron becomes substitutional again [8]. This results in an enhanced diffusion which lasts for a limited period of time. The enhanced diffusion ends as soon as the supersaturation of interstitials decays to its equilibrium thermal value and is thus referred to as Transient Enhanced Diffusion (TED) [8].

Typically the displacement in the tail region of a 30keV, $1\times10^{14}cm^{-2}$ B^+ implanted profile after an anneal at 800°C is > 700Å [8]. The equilibrium boron diffusion length under these conditions is only ≈25Å [9]. The peak of the boron profile (at a boron concentration > $10^{18}cm^{-3}$) remains static during TED and is electrically inactive [8]. If a silicon layer containing a buried boron marker layer which is incorporated by epitaxy is implanted by Si^+ TED of the boron marker layer is observed [10, 11]. The boron peak is static during TED and electrically inactive and the boron tail out diffuses with a displacement which is 2 orders of magnitude greater than thermal diffusion [10, 11].

The static boron peaks are observed when there are high concentrations of both boron and interstitials [8]. These static boron peaks have been explained to be due to clusters containing both boron and Si interstitials [8]. However, these clusters can not be observed by transmission electron microscopy and are thus consisting of a small number of atoms [8]. A model has been proposed which assumes that in the initial annealing stages when there is a high interstitial supersaturation, clusters with high interstitials content are formed (i.e. BI_2 clusters) [12]. At later annealing stages when the interstitial supersaturation is low these clusters decay and give rise to low interstitial content clusters (i.e. B_3I, B_4I clusters) [12].

At an annealing temperature of 800°C TED lasts more than 1 hour [13]. However, at annealing temperatures > 800°C TED lasts for a few tens of seconds or a few minutes and the displacement during TED is small compared to lower anneal temperatures [8].

The large time during which TED lasts at an anneal temperature of 800°C is due to the formation of small and extended defect clusters [8]. With a high supersaturation of Si interstitials and annealing at 800°C, extended {311} defects

nucleate and grow [14, 15]. These defects are rod like defects existing in the {311} habit plane and consist of condensates of Si self-interstitials forming five and seven member rings [14]. At large doses and very high implantation energies dislocation loops are formed [8]. When the supersaturation of interstitials decreases these extended defect clusters start dissolving, emitting interstitials which sustain TED for longer durations. If the anneal temperature is > 950°C the {311} defect unfaults to form perfect dislocations [8]. The {311} defects are unstable at high anneal temperatures and hence the short duration of TED at these temperatures. At annealing temperatures of > 800°C the estimated time for the interstitials to migrate and annihilate at the surface is of the order of a few tens of seconds to a few minutes and hence the short duration of TED at these temperatures [8].

The rate of growth and dissolution of defects is controlled by a process referred to as *Ostwald ripening* [11, 14, 15, 16]. This process results in the small defects shrinking and finally disappearing, while the large defects grow and become larger [16]. TEM experiments show that on annealing a sample containing extended defects, small defects shrink and large defects grow larger [17]. The simulation of the rates of evolution of TED agrees with the observed rates if Ostwald ripening is included in the simulations [11]. However, recently it has been shown that TED experiments can also be explained without including Ostwald ripening of the {311} defects in the simulations [18].

However, there is still future work needed to fully understand and model B TED in silicon. Although Ostwald ripening is widely used in simulations to interpret TED, a theory for the ripening of the {311} defect does not exist and is urgently needed [8]. More work is required to determine the importance of Ostwald ripening in the growth and dissolution of {311} defects and the evolution of TED [8]. Although

TED experiments suggest that the B_mI_n clusters are responsible for the static boron peak, optical experiments show only one small cluster I_3 consisting of Si interstitial atoms. Further work is thus needed to verify whether or not both I_3 clusters and B_mI_n clusters coexist and participate in TED and hence to modify existing models, which only use B-I clusters to interpret the static boron peak [8].

2.5 Boron Diffusion in $Si_{1-x}Ge_x$ and $Si_{1-x-y}Ge_xC_y$

As mentioned earlier in the chapter boron is believed to diffuse in silicon predominantly via interstitials. However, there is still debate in the literature about the mechanisms by which boron diffuses in $Si_{1-x}Ge_x$. The consensus in the literature is that boron diffusion in $Si_{1-x}Ge_x$ is less than that in silicon [19-31]. Kuo *et al.* [19] studied the diffusion of boron in relaxed $Si_{1-x}Ge_x$ layers with Ge contents up to 55% and showed that boron diffusion in the relaxed $Si_{1-x}Ge_x$ layer was retarded compared to Si layers up to a Ge content of 40% after which it seems to increase. The reduction in boron diffusion was attributed to a B-Ge pairing mechanism. As Ge diffuses slowly in Si, it was suggested that B pairing with Ge forming B-Ge pairs will thus diffuse slower in $Si_{1-x}Ge_x$ layers. In other studies boron was shown to diffuse slower in strained $Si_{1-x}Ge_x$ layers compared to Si layers [20, 21]. In a recent study of Zangenberg *et al.* [22], it was reported that there was no reduction in boron diffusion with increasing Ge content in Si rich relaxed $Si_{1-x}Ge_x$ layers. It was suggested that an enhancement due to a chemical effect could be counterbalanced by a retardation due to the pairing effect. They also studied the effect of strain on boron diffusion and it was shown that boron diffusion was retarded in compressively strained $Si_{1-x}Ge_x$ layers but enhanced in tensile strained Si layers [22].

Figure 2.10 shows a summary of extracted boron diffusion coefficients in $Si_{1-x}Ge_x$ alloys versus Ge content reported in the literature after [5]. Data is presented for strained $Si_{1-x}Ge_x$ alloys measured at 860°C after Kuo *et al.* [23] and Fang *et al.* [20]. This data shows reduction in boron diffusion coefficient in $Si_{1-x}Ge_x$ with increasing germanium content. The data presented for relaxed $Si_{1-x}Ge_x$ alloys measured at 800°C after Kuo *et al.* [19] also shows reduction in boron diffusion coefficient in $Si_{1-x}Ge_x$ with increasing germanium content. However, the data presented presented for relaxed $Si_{1-x}Ge_x$ alloys measured at 800°C after Zangenberg [22] shows no variation in boron diffusion coefficient with increasing germanium content. The data presented after Dunlap [24] and Meer *at al.* [25] show much greater boron diffusion in germanium compared to $Si_{1-x}Ge_x$ alloys.

The progressive reduction in boron diffusion in $Si_{1-x}Ge_x$ with increasing Ge content, was attributed to a bandgap narrowing effect, which alters the charged point defect concentration and hence retards born diffusion [26, 27]. However, Cowern *et al.* [28] argued that this effect is not large enough to explain the observed reduction. Cowern *et al.* [28] proposed that the observed reduction is due to a decrease in the self-interstitial concentration caused by the long-range strain in the $Si_{1-x}Ge_x$ layer. Fang *et al.* [29] rejected this idea and attributed the reduction to a decrease in mobile boron diffusivity rather than the self-interstitial concentration. Defect injection studies have shown that boron diffusion in silicon and strained $Si_{1-x}Ge_x$ up to 20% Ge is largely interstitial mediated [20, 30].

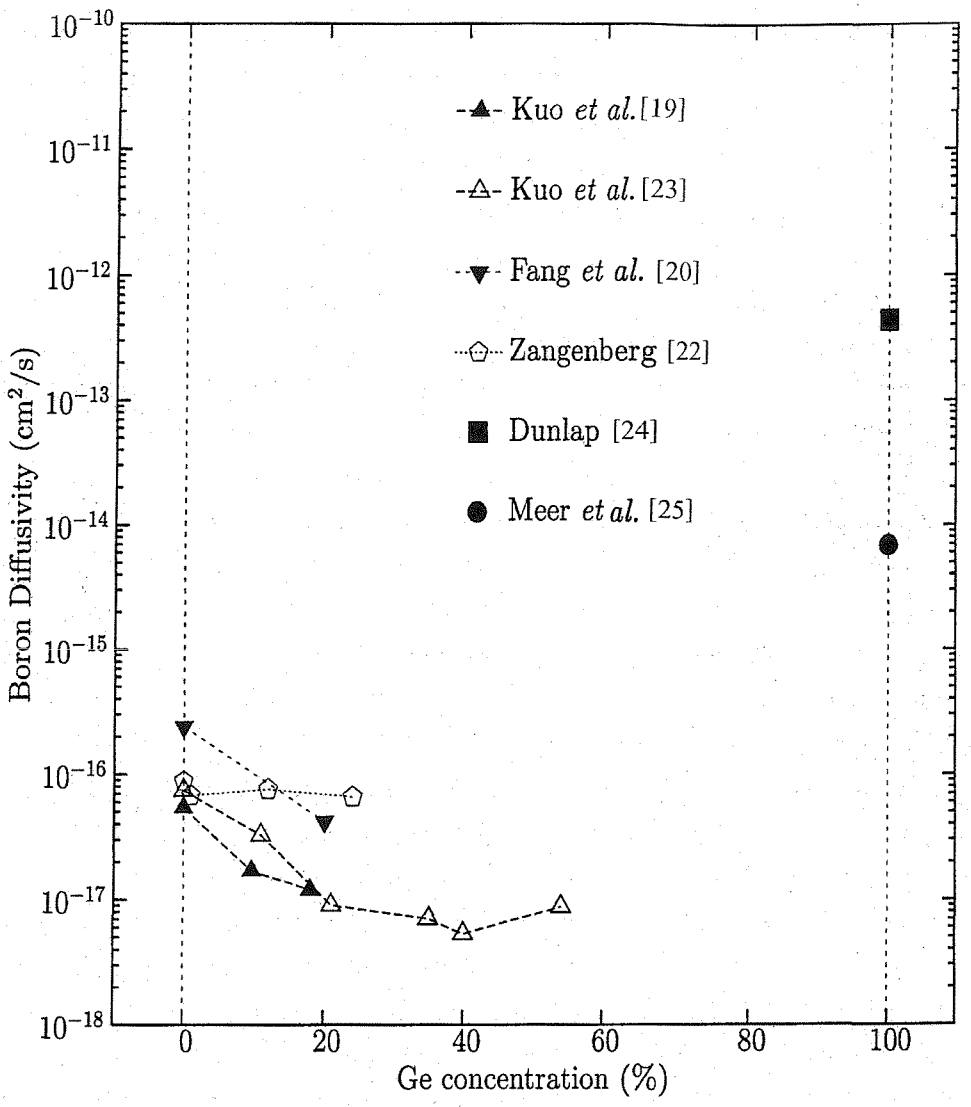

Figure 2.10: Extracted Boron diffusion coefficients in $Si_{1-x}Ge_x$ alloys versus Ge content values from the literature after [5]. Data is presented from the work reported by several authors; solid triangles: in relaxed $Si_{1-x}Ge_x$ alloys measured at 800°C after Kuo *et al.* [19], open triangles: in strained $Si_{1-x}Ge_x$ alloys measured at 860°C after Kuo *et al.* [23], inverted solid triangles: in strained $Si_{1-x}Ge_x$ alloys measured at 860°C after Fang *et al.* [20], open pentagons: in relaxed $Si_{1-x}Ge_x$ alloys measured at 800°C after Zangenberg [22]. Boron diffusion coefficients in germanium measured at 800°C are also included after Dunlap [24] and Meer *et al.* [25].

Boron diffusion in $Si_{1-x-y}Ge_x C_y$ layers is reported to be less than in $Si_{1-x}Ge_x$ layers [31-33]. In the reported models it was assumed that boron diffuses in $Si_{1-x}Ge_x$ and $Si_{1-x-y}Ge_x C_y$ mainly via interstitials [31-33]. Carbon was reported to diffuse very quickly via a kick-out mechanism combining with the self interstitials and creating a vacancy super-saturation and an interstitial under-saturation which results in the retarded boron diffusion [31-33].

Figure 2.11 shows a plot of modelled intrinsic B diffusion coefficients in $Si_{1-x-y}Ge_xC_y$ layers as a function of annealing temperature for three carbon concentrations ($5\times10^{17}cm^{-3}$, $5\times10^{18}cm^{-3}$ and $5\times10^{19}cm^{-3}$) after Rajendran *et al.* [32]. Measured B diffusion coefficients in $Si_{1-x-y}Ge_xC_y$ layers with carbon contents of $<5\times10^{17}cm^{-3}$and $1\times10^{20}cm^{-3}$ are also shown in the plot. The values in the plot show a strong increase in reduction of boron diffusivity with the increase in carbon content and reasonable agreement between measured and modelled values.

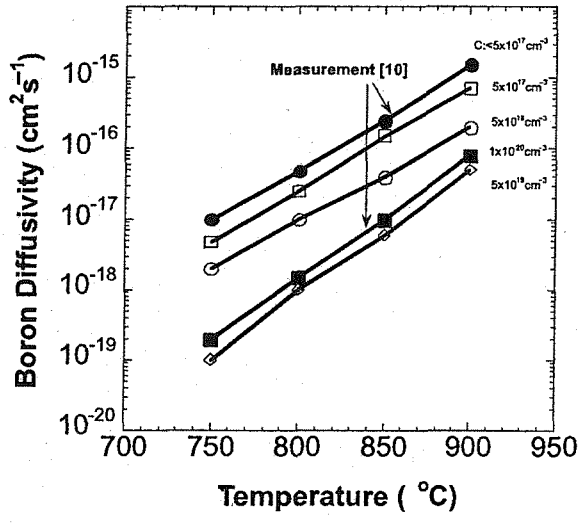

Figure 2.11: Modelled (open) and measured (solid) boron diffusivities versus temperature in $Si_{1-x-y}Ge_xC_y$ for different carbon concentrations: $5\times10^{17}cm^{-3}$, $5\times10^{18}cm^{-3}$, $5\times10^{19}cm^{-3}$ and $1\times10^{20}cm^{-3}$, after Rajendran *et al.* [32].

2.6 Athena Diffusion Models

Diffusion of dopants and point defects in SSUPREM4 (program installed in Athena) is described by a number of user-specifiable models, the three most basic of which are [34]:

1. The fermi diffusion model
2. The two dimensional diffusion model
3. The fully coupled diffusion model

All of the three above models rely on the concept of pair diffusion, which says that a dopant atom can not diffuse on its own and it needs the assistance of a point defect (silicon self-interstitial or vacancy) in the near vicinity as a diffusion vehicle. A dopant's diffusion is then actually the diffusion of the dopant-point defect pair. The point defect can diffuse freely or as a dopant-defect pair. The models are natural extensions of one another, in the sense that the fermi model is incorporated in the two dimensional model which in turn is included in the fully-coupled model. The most significant difference between them is the way point defects are represented and treated throughout the simulation and how the specific dopant diffusion is formulated.

2.6.1 Fermi Diffusion Model

The point defect populations are assumed to be in thermodynamical equilibrium and thus need no direct representation. All the effects of point defects on dopant diffusion are built into the pair diffusivities. The advantage of using fermi diffusion model is fast execution. This is because since point defects are not directly represented only the diffusion of dopants needs to be simulated.

In the fermi model each dopant obeys a continuity equation of the form shown in equation 2.10.

$$\frac{\partial C_A}{\partial t} = \nabla.\left[(D_{AV} + D_{AI}) C_{A+} \nabla \ln\left(C_{A+} \left(\frac{n}{n_i} \right)^z \right) \right] \tag{2.10}$$

where the factor $\frac{n}{n_i}$ inside the logarithm accounts for the electric field effect. The intrinsic carrier concentration n_i is calculated as:

$$n_i = n_{i_0} \cdot \exp\left(\frac{-n_{i_E}}{kT} \right) T^{n_{ipow}} \tag{2.11}$$

where n_{i0}, n_{iE} and T^{nipow} are specified in the MATERIAL statement by the parameters NI.0, NI.E and NI.POW respectively. Z accounts for the direction of the electrical force vector on diffusing particle and should be +1 for donors or -1 for acceptors. D_{AV} and D_{AI} are the joint contributors to the dopant diffusivity from dopant-vacancy and dopant-interstitial pairs in different charge states. The terms depend on both the position of the Fermi level as well as the temperature and are expressed as:

$$D_{AV}\left(T, \frac{n}{n_i} \right) = D_{AV}^{x} + D_{AV}^{-}\left(\frac{n}{n_i} \right)^1 + D_{AV}^{=}\left(\frac{n}{n_i} \right)^2 + D_{AV}^{+}\left(\frac{n}{n_i} \right)^{-1} + D_{AV}^{++}\left(\frac{n}{n_i} \right)^{-2} \tag{2.12}$$

$$D_{AI}\left(T, \frac{n}{n_i} \right) = D_{AI}^{x} + D_{AI}^{-}\left(\frac{n}{n_i} \right)^1 + D_{AI}^{=}\left(\frac{n}{n_i} \right)^2 + D_{AI}^{+}\left(\frac{n}{n_i} \right)^{-1} + D_{AI}^{++}\left(\frac{n}{n_i} \right)^{-2} \tag{2.13}$$

where the temperature dependency is embedded in the intrinsic pair diffusivities, which are specified by arrhenius expressions of the type:

$$D_{AX}^{c} = D_{AX_0}^{c} \cdot \exp\left(\frac{-D_{AX_E}^{c}}{kT} \right) \tag{2.14}$$

where: A is the dopant, x is the neutral charge state, c is the charge state and could be neutral x, negative – or positive + and X is the point defect interstitial I or vacancy V.

2.6.2 Two Dimensional Diffusion Model

In this model the point defect populations are explicitly represented and evolved in time. If there is a super saturation of point defects it will affect the dopant diffusivity through a simple scale factor, which goes to unity as the actual defect concentration approaches the equilibrium defect concentration. Hence, with equilibrium defect concentrations the two dimensional model merely reproduces the fermi model. In this model it is assumed that the diffusion of dopants is highly influenced by the diffusion of point defects, while the diffusion of point defects is considered to be independent of dopant diffusion.

2.6.3 Fully Coupled Diffusion Model

The fully coupled diffusion model is very similar to the two dimensional model with one difference that now the diffusion of point defects is considered to be dependant on the dopant diffusion. Thus in this model there is a true two way interaction between the diffusion of dopants and point defects and hence the name fully coupled diffusion.

The reader is referred to SILVACO ATHENA users Manual [34] for details of the mathematical representations of both the two dimensional and fully coupled models.

References

1. S. C. Jain, "Germanium-Silicon Strained Layers and Heterostructures"; Academic Press, Boston, USA, (1994).
2. R. Hull, J. C. Bean, D. Bahnck, J. M. Bonar and C. Buescher, "In-situ electron microscope studies of misfit dislocation introduction into Ge_xSi_{1-x}/Si hetrostructures"; in Evaluation of Advanced Semiconductor Materials By Electron Microscopy, pp. 381-394, Plenum Publishing Corporation, (1990).
3. E. Kasper and H. -J. Herzog, "Elastic strain and misfit dislocation density in $Si_{0.92}Ge_{0.08}$ films on silicon substrates"; Thin Solid Films, vol. 44, pp. 357-370, (1977).
4. J. D. Plummer, M. D. Deal and P. B. Griffin, "Dopant Diffusion"; in Silicon VLSI Technology Fundamentals, Practice and Modeling, Prentice Hall Inc., New Jersey, USA, pp. 371-449, (2000).
5. S. Uppal, "Diffusion of Boron and Silicon in Germanium"; Ph.D. thesis, Materials Research Group, School of Engineering Sciences, University of Southampton, United Kingdom, September (2003).
6. W. Frank, U, Gösele, H. Mehrer and A. Seeger, "Diffusion in silicon and germanium"; in Diffusion in crystalline solids, Academic Press, New York, USA, pp. 63-142, (1984).
7. M. J. Mitchell, "Fabrication and Characterisation of SiGe Heterojunction Bipolar Transistors formed by Germanium Implantation"; Ph.D. thesis, Microelectronics Research Group, School of Electronics and Computer Science, University of Southampton, United Kingdom, August (2001).
8. S. C. Jain, W. Schoenmaker, R. Lindsay, P. A. Stolk, S. Decoutere, M. Willander and H. E. Maes, "Transient enhanced diffusion of boron in Si";

Applied Physics Reviews, Journal of Applied Physics, vol. 91 (11), pp. 8919-8941, (2002).

9. P. M. Fahey, P. B. Griffin and J. D. Plummer, "Point defects and dopant diffusion in silicon"; Reviews of Modern Physics, vol. 61, pp. 289-384, (1989).
10. P. A. Stolk, H. -J. Gossmann, D. J. Eaglesham, D. C. Jacobson, H. S. Luftman and J. M. Poate, "Understanding and controlling transient enhanced dopant diffusion in silicon"; Materials Research Society Symposium Proceedings, vol. 354, p. 307, (1995).
11. N. Cowern and C. Rafferty, "Enhanced diffusion in silicon processing"; Materials Research Society Bulletin, vol. 25, pp. 39-44, (2000).
12. L. Pelaz, G. H. Gilmer, H.-J. Gossmann, C. S. Rafferty, M. Jaraiz and J. Barbolla, "B cluster formation and dissolution in Si: A scenario based on atomistic modeling"; Applied Physics Letters, vol. 74 (24), pp. 3657-3659, (1999).
13. A. E. Michel, W. Rausch, P. A. Ronsheim and R. H. Kastl, "Rapid annealing and the anomalous diffusion of ion implanted boron into silicon"; Applied Physics Letters, vol. 50 (7), pp. 416-418, (1987).
14. D. J. Eaglesham, V. C. Venezia, H. –J. Gossmann and A. Agarwal, "Quantitative TEM of point defects in Si"; Journal of Electron Microscopy, vol. 49, pp. 293-298, (2000).
15. D. J. Eaglesham, P. A. Stolk, H. J. Gossmann and J. M. Poate, "Implantation and transient B diffusion in Si: The source of the interstitials"; Applied Physics Letters, vol. 65 (18), pp. 2305-2307, (1994).

16. S. C. Jain and A. E. Hughes, "Ostwald ripening and its application to precipitates and colloids in ionic crystals and glasses"; Journal of Materials Science, vol. 13 (8), pp. 1611-1631, (1978).

17. K. Moller, K. S. Jones and M. E. Law, "Cross-sectional transmission electron microscopy analysis of {311} defects from Si implantation into Silicon"; Applied Physics Letters, vol. 72 (20), pp. 2547-2549, (1998).

18. M. E. Law and K. S. Jones, "A new model for {311} defects based on in situ measurements"; Technical Digest of the International Electron Devices Meeting IEDM, pp. 511-514, (2000).

19. P. Kuo, J. L. J. L. Hoyt, J. F. Gibbons, J. E. Turner and D. Lefforge, "Boron Diffusion in Si and Si_{1-x} Ge_x"; Materials Research Society Symposium Proceedings, vol. 379, pp. 373-378, (1995).

20. T. T. Fang, W. T. C. Fang, P. B. Griffin and J. D. Plummer, "Calculation of the fractional interstitial component of boron diffusion and segregation coefficient of boron in $S_{0.8}$ $Ge_{0.2}$"; Applied Physics Letters, vol. 68 (6), pp. 791-793, (1996).

21. K. Rajendran and W. Schoenmaker, "Studies of boron diffusivity in strained Si_{1-x} Ge_x epitaxial layers"; Journal of Applied Physics, vol. 89 (2), pp. 980-987, (2001).

22. N. R. Zangenberg, "Defect and diffusion studies in Si and SiGe"; Ph.D. dissertation, University of Aahrus, Denmark, (2003).

23. P. Kuo, J. L. Hoyt, J. F. Gibbons, J. E. Turner and D. Lefforge, "Effects of Si thermal oxidation on boron-diffusion in Si and strained $Si_{1-x}Ge_x$ layers"; Applied Physics Letters, vol. 67 (5), pp. 706-708, (1995).

24. W. C. Dunlap, Jr., "Diffusion of impurities in germanium"; Physical Review, vol. 94, pp. 1531-1540, (1954).

25. W. Meer and D. Pommerring "Diffusion von aluminium und bor in germanium"; Zeitschrift für Angewandte Physik, vol. 23, pp. 369-372, (1967).

26. N. Moriya, L. C. Feldman, C. A. King, J. Bevk and B. Freer, "Boron diffusion in strained $Si_{1-x}Ge_x$ epitaxial layers"; Physical Review Letters, vol. 71, pp. 883-886, (1993).

27. C. Chen, U. M. Gösele and T. Y. tan, "Dopant diffusion and segregation in semiconductor heterostructures: Part2. B in Ge_xSi_{1-x}/Si structures"; Applied Physics A: Material Science and Processing, vol. 68, pp. 19-24, (1999).

28. N. E. Cowern, P. C. Zalm, P. V. Sluis, D. J. Gravestijn and W. B. de Boer, "Diffusion in strained Si(Ge)"; Physical Review Letters, vol. 72, pp. 2585-2588, (1994).

29. W. T. C. Fang, P. B. Griffin and J. D. Plummer, "Implant enhanced diffusion of boron in silicon germanium"; Materials Research Society Proceedings, vol. 379, pp. 379-384, (1995).

30. J. M. Bonar, B. M. McGregor, N. E. B. Cowern, A. H. Dan, G. A. Cokke and A. F. W. Willoughby, "Furnace and RTA injection of point defects into cvd grown b doped Si and SiGe"; Materials Research Society Symposium Proceedings, vol. 610, pp. B4.9.1-B4.9.6, (2000).

31. H. J. Osten, D. Knoll and H. Rűcker, "Dopant Diffusion control by adding carbon into Si and SiGe: principles and device applications"; Materials Science and Engineering, vol. B87, pp. 262-270, (2001).

32. K. Rajendran, W. Schoenmaker, "Modeling of complete suppression of boron out-diffusion in $Si_{1-x}Ge_x$ by carbon incorporation"; Solid-State Electronics, vol. 45, pp. 229-233, (2001).

33. R. Scholz, U. Gösele, J. –Y. Huh and T. Y. Tan, "Carbon-induced undersaturation of silicon self interstitials"; Applied Physics Letters, vol. 72 (2), pp. 200-202, (1998).

34. "SSUPREM4 Models" in ATHENA USER Manual, SILVACO.

Chapter 3

Growth of Sharp Boron Profiles in n-type Si, p-type $Si_{1-x}Ge_x$ and n-type Si Layers at 700°C with Dual Control of n- and p-type Dopants

3.1 Introduction

The growth of n-type Si, p-type $Si_{1-x}Ge_x$ and n-type Si layers is needed for the formation of NPN $Si_{1-x}Ge_x$ heterojunction bipolar transistor layers. The dual control of n- and p-type dopants in the same growth step is challenging and requires careful control of the growth parameters in order to control the dopant profiles.

This chapter describes the growth of n-type Si, p-type $Si_{1-x}Ge_x$ and n-type Si layers in a single epitaxy step for use in a non-selective $Si_{1-x}Ge_x$ heterojunction bipolar transistor growth process at 700°C. A process is developed to eliminate the edge from the boron profile in the $Si_{1-x}Ge_x$ layer by interrupting the growth with a hydrogen anneal in between the growth of the $Si_{1-x}Ge_x$ and the Si cap layers. This process gives very sharp and narrow boron profiles suitable for the base of a heterojunction bipolar transistor or boron marker layers for diffusion studies. Control of the n-type dopant concentration in the starter Si layer is developed by varying the growth conditions. The layer thicknesses are compared using three different analytical

techniques; Secondary Ion Mass Spectroscopy (SIMS), Transmission Electron Microscopy (TEM) and Spectroellipsometry (SE) and a good agreement is obtained for the three different methods.

3.2 Experimental Procedure

N-type Si, p-type $Si_{1-x}Ge_x$ and n-type Si layers similar to those suitable for $Si_{1-x}Ge_x$ heterojunction bipolar transistors were grown using a single wafer low pressure chemical vapour deposition (LPCVD) system. Half masked wafers, in which the left half of the wafer was covered with a 600nm thick deposited oxide layer, were used for growth. The ex-situ wafer clean consisted of a standard RCA clean followed by a brief dip in a dilute HF solution (H_2O: HF, 100:1) to thin the RCA oxide. The in-situ clean was a hydrogen bake at 1Torr (133Pa) and 950°C for 5 minutes to desorbe the oxide remaining on the wafer surface. The wafer was then cooled in hydrogen to the initial layer growth temperature (800°C) at which a 10nm Si starter layer was grown after which it was cooled again in hydrogen to the structure growth temperature (700°C) and the pressure was set to 0.5Torr (67Pa). The growth was non-selective, hence polysilicon was deposited over the oxide and single crystal layers were deposited over the exposed silicon during growth. The growth started with a phosphorus doped silicon starter layer, followed by an undoped, $Si_{1-x}Ge_x$ spacer layer, a p-type $Si_{1-x}Ge_x$ layer and an undoped $Si_{1-x}Ge_x$ spacer layer. Finally, a phosphorus doped, silicon cap layer, was grown. Figure 3.1 shows a schematic of the structure of the growth layers. Silane (SiH_4) and germane (GeH_4) were used as source gases with hydrogen as the carrier gas. Diborane (B_2H_6) and phosphine (PH_3) diluted in hydrogen were used for doping. The $Si_{1-x}Ge_x$ layer growth time was varied to control the boron and germanium profiles. The effect of growth interrupts with 7 minutes and 5 minutes

hydrogen anneals (hydrogen flow of 350sccm) in between the growth of the $Si_{1-x}Ge_x$ and the Si starter and cap layers respectively was investigated in order to eliminate the boron tailing edge into the Si cap layer and reduce the n-type dopant on the surface after the growth of the Si starter layer. Several growth were done in which the growth temperature of the Si starter layer and the phosphine gas flow were varied to investigate the control of the n-type dopant concentration. Table 3.1 summarises the details of the growth conditions for the different growth runs. The hydrogen anneal growth interrupts are indicated in the table with small H label boxes in table 3.1.

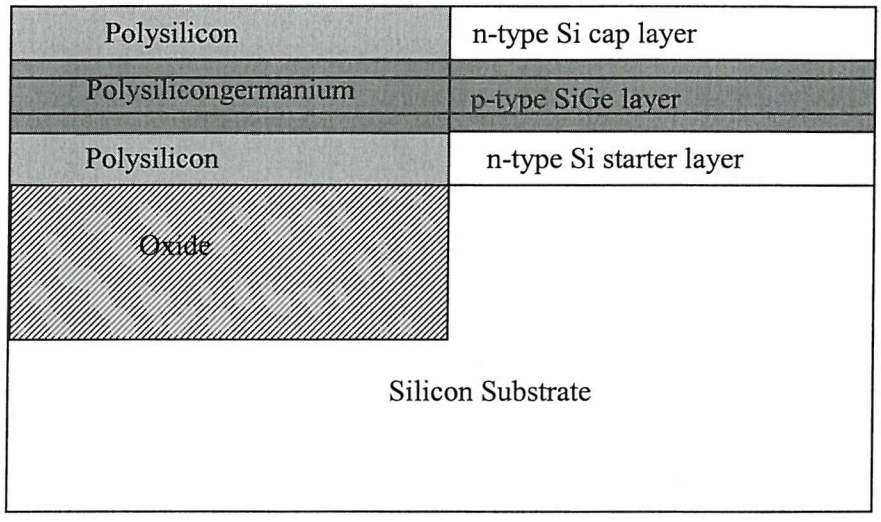

Figure 3.1: A schematic of the structure of the growth layers.

Secondary ion mass spectroscopy (SIMS) was used to detect the boron and germanium profiles using a 3keV oxygen beam and a 14.5keV caesium beam with a high mass resolution to detect the phosphorus profile. The SIMS analysis was done by Dr. Chris Mulcahy at Cascade Scientific ltd. The dopant concentrations and layer thicknesses were extracted from the SIMS profiles by a method illustrated in figure 3.2. The Si starter layer (collector) thickness t_C was defined to be from the point at which the phosphorus profile starts to rise above its background level to the start of

the rising edge of the germanium profile. The Si starter layer (collector) doping concentration N_C was defined as the average concentration across the layer. The germanium percentage concentration was calculated by dividing the the peak germanium concentration N_{Ge} by the total concentration of atoms in a silicon lattice $5\times10^{22}cm^{-3}$ and mutiplying by 100% as shown in equation 3.1. The Si_{1-x} Ge_x layer thickness t_{SiGe} was defined as the region for which the germanium composition is ≥0.2% Ge, which is equivalent to a germanium concentration of $1\times10^{20}cm^{-3}$. The undoped Si_{1-x} Ge_x spacer layer beween the Si starter layer and the p-type Si_{1-x} Ge_x layer (collector-base spacer layer $t_{C/B}$) was defined as the region where the germanium composition is ≥0.2% Ge and the boron p-type doping concentration is less than the phosphorus n-type doping concentration in the Si starter layer. The undoped Si_{1-x} Ge_x spacer layer beween the p-type Si_{1-x} Ge_x layer and the n-type Si cap layer (emitter-base spacer $t_{E/B}$) was defined as the region where the germanium composition is ≥0.2% Ge and the boron doping concentration is less than the phosphorus doping concentration in the Si cap layer. The boron doped Si_{1-x} Ge_x layer (base layer t_B) was defined as the region where the boron doping is above the phosphorus doping concentrations in the Si starter and cap layers. The boron doping concentration in the Si_{1-x} Ge_x layer (N_B) was defined as the peak boron concentration in the layer. The Si cap layer (emitter) thickness (t_E) was defined as the region from the growth surface to the falling edge of the germanium profile. The doping concentration in the Si cap layer (emmitter) (N_E) was taken as the peak phosphorus concentration in the layer.

$$\text{Ge content (\%)} = \frac{N_{GE}}{5\times10^{22}}\times100\% \qquad (3.1)$$

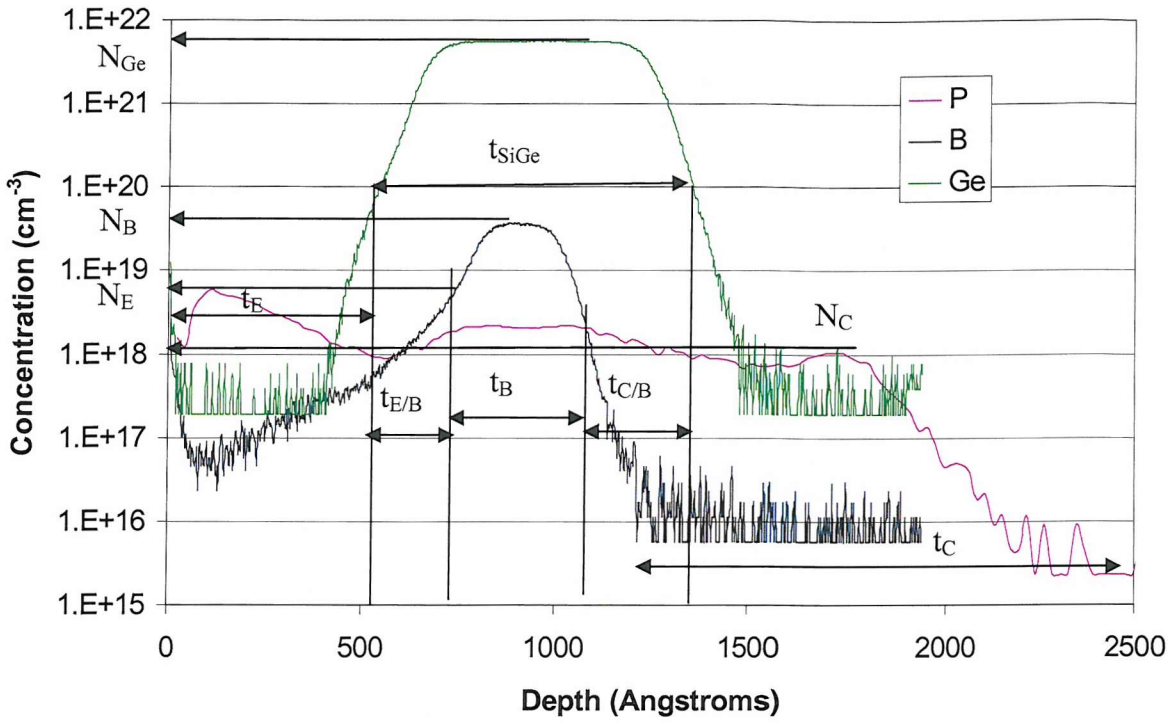

Figure 3.2: Extraction of layers thicknesses and doping concentrations from the SIMS profiles.

Transmission electron microscopy analysis was performed by Dr. Yun Wang at Surrey University, to verify the layer thicknesses and crystalline quality. The layer thicknesses and compositions were also analysed by ultra violet to visible, UV-VIS (wavelengths: 200 to 1000 nm) spectroellipsometry (SE) by Dr. Octavian Buiu at the University of Liverpool. Experimental data was obtained at an angle of incidence of 75° using a M2000U J. A. Woollam instrument [1]. The WVASE32™ software package was used for modelling. The fitting of the experimental results and the model were used simultaneously to determine the compositions and thicknesses of the layers. Spectroellipsometry is a well-established non-destructive technique for characterising semiconductor materials including $Si_{1-x}Ge_x$ and $Si_{1-x-y}Ge_xC_y$ layers [2-4].

Ellipsometry is a non-destructive analysis technique used to characterise materials during which elliptically polarised electromagnetic waves are directed on to the materials being characterised and the reflected waves are then detected. It is based on the fact that both the phase and amplitude of the incident electromagnetic wave change upon reflection from the materials surface. This change in phase and amplitude depends on many things including the properties of the material and its thickness. The difference in the change in phase that occurs upon reflection termed "delta Δ" (as shown in equation 3.2) and the angle whose tangent is the ratio of the magnitudes of the total reflection coefficients termed "Psi Ψ" (as shown in equation 3.3) are measured and used along with an assumed model of the material structure to calculate the material properties including layer thicknesses [5].

$$\Delta = \delta_1 - \delta_2 \tag{3.2}$$

Where δ_1 is the phase difference between the parallel component and the perpindicular component of the incident wave and δ_2 is the phase difference between the parallel component and the perpindicular component of the reflected wave.

$$\tan\psi = \frac{|R^p|}{|R^s|} \tag{3.3}$$

Where R^p is the ratio of the amplitudes of the parallel components of the reflected wave to the incident wave and R^s is the ratio of the amplitudes of the perpendicular components of the reflected wave to the incident wave..

Growth Number	n-type Si starter layer			Undoped Si_{1-x} Ge_x spacer layer			p-type Si_{1-x} Ge_x layer			Undoped Si_{1-x} Ge_x spacer layer			n-type Si cap layer		
	Temp (°C)	Gas flow (sccm)	Time	Temp (°C)	Gas flow (sccm)	Time	Base Temp (°C)	Gas flow (sccm)	Time	Temp °C	Gas flow (sccm)	Time	Temp °C	Gas flow (sccm)	Time
2Si910	800	H_2 120 SiH_4 40 L PH_3 100	1min 3s	700	H_2 120 SiH_4 40 $GeH_4$15	20s	700	SiH_4 40 $GeH_4$15 $B_2H_6$30	14s	700	H_2 120 SiH_4 40 GeH_4 15	4s	700	H_2 120 SiH_4 40 H PH_3 1	2mins 5s
2Si912	800 700	H_2 120 SiH_4 40 L PH_3 100	10s 2mins 5s	700	H_2 120 SiH_4 40 $GeH_4$15	21s	700	SiH_4 40 $GeH_4$15 $B_2H_6$30	14s	700	H_2 120 SiH_4 40 GeH_4 15	10s	700	H_2 120 SiH_4 40 H PH_3 0.5	2mins 5s
2Si913	800 700	H_2 120 SiH_4 40 L PH_3 100 L PH_3 10	15s 4mins 17s	700	H_2 120 SiH_4 40 $GeH_4$13	13s	700	H_2 120 SiH_4 40 $GeH_4$13 $B_2H_6$30	14s	700	H_2 120 SiH_4 40 GeH_4 13	12s	700	H_2 120 SiH_4 40 H PH_3 0.5	2mins 5s
2Si914	800	H_2 120 SiH_4 40 L PH_3 100	2mins 16s	700	H_2 120 SiH_4 40 $GeH_4$13	13s	700	H_2 120 SiH_4 40 $B_2H_6$30	13s	700	H_2 120 SiH_4 40 GeH_4 13	10s	700	H_2 120 SiH_4 40 H PH_3 0.5	2mins 5s
2Si918	800 700	H_2 120 SiH_4 40 L PH_3 100 L PH_3 4.7	30s 6mins 26s H	700	H_2 120 SiH_4 40 $GeH_4$13	7s	700	H_2 120 SiH_4 40 $GeH_4$13 $B_2H_6$30	13s	700	H_2 120 SiH_4 40 GeH_4 13	10s H	700	H_2 120 SiH_4 40 H PH_3 0.5	2mins 5s

Table 3.1: A summary of the growth details of all growth runs done.

3.3 Results and Discussion

Figure 3.3 shows the boron and germanium SIMS profiles of two boron doped Si_{1-x} Ge_x layers grown at 700°C. The germanium profiles have sharp edges and flat peaks, with a peak concentration of 12%, indicating uniform germanium concentrations throughout the base layers and good control of the Si_{1-x} Ge_x growth. The boron profile in figure 3.3 (a) has a sharp starting edge and a tailing edge through the emitter (see growth number 2Si914 in table 3.1 for details). This tailing edge is a problem as it prevents good control of the base thickness and would cause tunnelling leakage in a Si_{1-x} Ge_x heterojunction bipolar transistor. Removing this boron tailing edge was investigated by interrupting the growth, after the undoped Si_{1-x} Ge_x spacer (emitter-base spacer) layer growth but before the Si cap (emitter) layer growth, and passing 350sccm hydrogen through the chamber for 5 minutes to remove the boron dopant gas (diborane B_2H_6) from the chamber (see growth number 2Si918 in table 3.1 for details). Figure 3.3 (b) shows the boron and germanium SIMS profiles for these growth conditions and it can be seen that the boron tailing edge has been totally eliminated. This interruption eliminated the boron tailing edge and thus resulted in a reduction in the boron doped base width by a factor of 2 from 44nm (a) to 22nm (b). The germanium profile width, at a germanium concentration of 2%, was also reduced from 64nm (a) to 31nm (b), this was due to a reduction of the total Si_{1-x} Ge_x layer growth time from 36s to 30s. The achieved Si_{1-x} Ge_x heterojunction bipolar transistor base profile (figure 3.3 (b)) is suitable for high frequency performance devices with a cut off frequency f_T of the order of 100GHz as can be seen from the work of Kasper et al [6] who showed that the cut off frequency f_T of Si_{1-x} Ge_x heterojunction bipolar transistors increased from 20GHz to 100GHz mainly as a result of reducing the Si_{1-x} Ge_x base thickness from 65nm to 25nm.

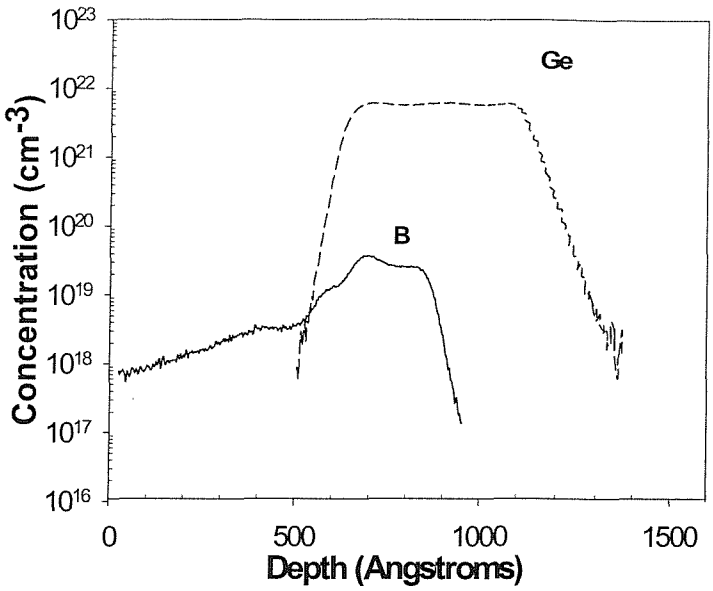

(a)

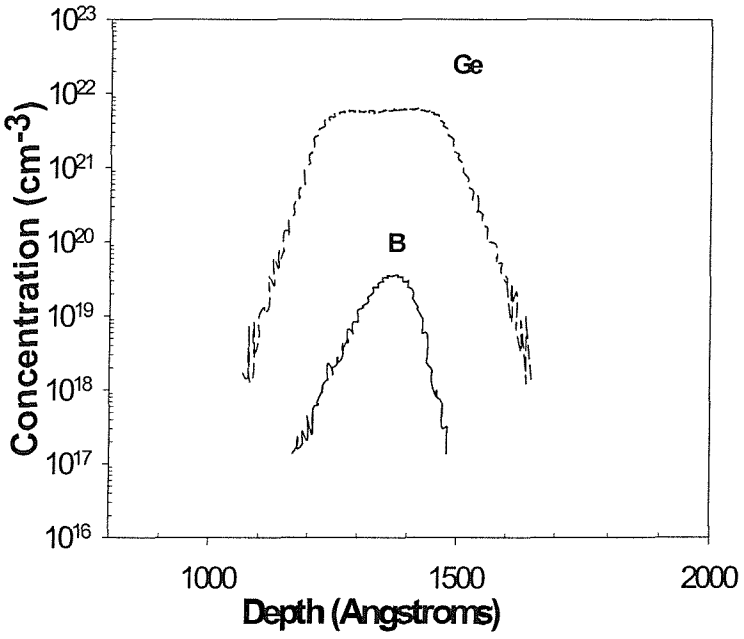

(b)

Figure 3.3: The Boron (B solid) and germanium (Ge dashed) SIMS profiles of two $Si_{1-x}Ge_x$ HBT growth layers; showing (a), with no growth interruption after the base growth: wide Ge and B profiles with a B tailing edge into the emitter, and (b) with a growth interruption after the base growth: narrow Ge and B profiles with no B tailing edge into the emitter.

Figure 3.4 shows an arrhenius plot of the variation of the silicon collector n-type dopant (phosphorus) concentration with growth temperature. The solid triangles data points are from this work (growth number 2Si910 at 800°C and 2Si912 at 700°C see table 3.1), the solid squares are from the work of Bonar on the same growth system [7] and the open circles are from the work of Agnello et al. [8] on atmospheric pressure chemical vapour growth. As seen in figure 3.4, the data from this work, Bonar's work [7] and Agnello et al.'s work [8] all show an increase in phosphorus concentration with a decrease in growth temperature with a decrease in slope for higher growth temperatures seen in Agnello et al.'s data [8]. The differences in phosphorus concentrations and slopes for the three different data sets is due to variation in growth pressure and gas flows, which affect the dopant incorporation. The growth in this work was done at a growth pressure of (0.5 Torr) 67Pa and a phosphine gas flow of 100sccm of a 0.01% phosphine gas. Bonar's [7] growth was done at (1 Torr) 133Pa with a 5sccm phosphine gas flow of a 25 volumes per million phosphine gas. Agnello et al.'s [8] growth was done at atmospheric pressure 100KPa with a 4 parts per million phosphine gas source. The data from this work shows that the phosphorus concentration increases by a factor of 20 from $5x10^{16}cm^{-3}$ to $1x10^{18}cm^{-3}$ with a 100°C decrease in growth temperature from 800°C to 700°C respectively. This corresponds to a decrease in silicon growth rate from 113 nm/min to 47 nm/min, respectively. The silicon growth rates were calculated by dividing the Si starter (collector) layer thickness obtained from measurements on the SIMS profiles (see experimental procedure figure 3.2) by the layer's growth time (see table 3.1). This could be explained by the theory of Reif et al. [9] who showed that at lower growth rates an equilibrium is established between the solid and the gas phases of the dopant,

hence increasing the dopant incorporation and that this equilibrium is not achieved at higher growth rates, hence less dopant incorporation occurs.

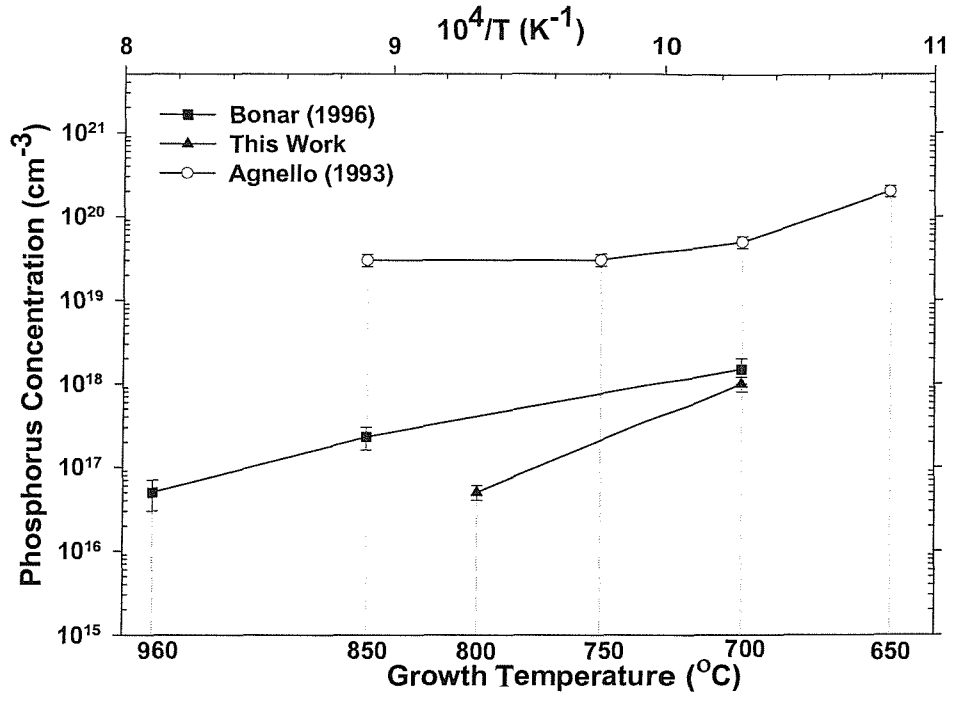

Figure 3.4: Variation of the n-type dopant (phosphorus) concentration in Si with growth temperature, solid triangles (this work growth number 2Si910 at 800°C and 2Si912 at 700°C see table 3.1), solid squares (Bonar [7]), open circles (Agnello et al. [8]) all showing an increase in dopant incorporation with a decrease in growth temperature.

Varying the phosphine gas flow at a growth temperature of 700°C from 100sccm (2Si912) to 10sccm (2Si913) and to 4.7sccm (2Si918) (see table 3.1 for growth details), we obtain a linear variation of phosphorus concentration with phosphine gas flow as shown in figure 3.5. A phosphorus concentration of $1x10^{17}cm^{-3}$ is obtained by reducing the phosphine flow to 4.7sccm. This collector doping concentration is the typically used for high frequency performance devices [10].

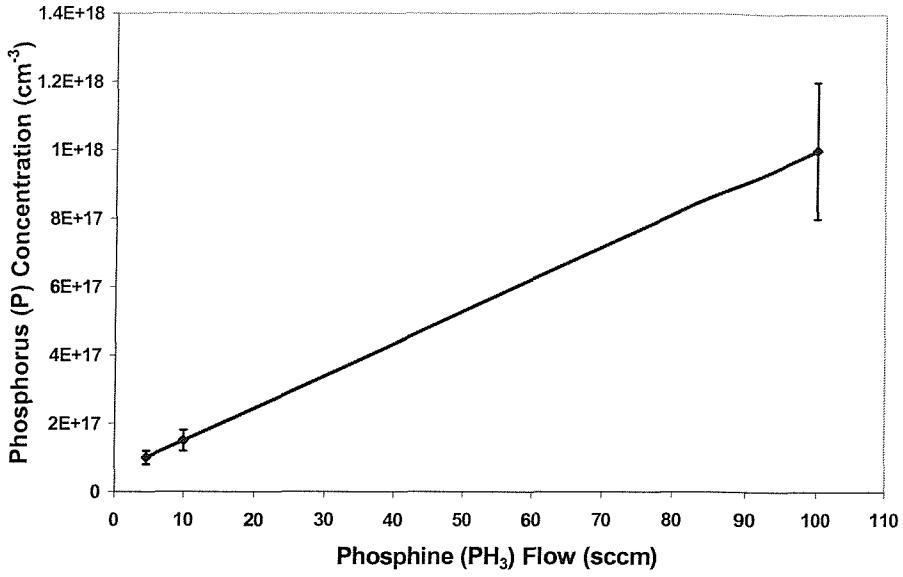

Figure 3.5: Variation of the n-type dopant (phosphorus) concentration in Si with phosphine gas flow, layers grown at 700°C (with phosphine flows of 100sccm, 10sccm and 4.7 sccm for growth numbers 2Si912, 2Si913 and 2Si918 respectively see table 3.1 for details).

Figure 3.6 shows the boron, germanium and phosphorus SIMS pofiles of the optimised $Si_{1-x}Ge_x$ heterojunction bipolar transistor layers grown at 700°C (growth 2Si918 see table 3.1 for details). The germanium profile is flat and uniform with a peak concentration of 12% Ge. The boron profile is narrow and situated within the germanium profile (as seen previously in figure 3.3 (b)). The phosphorus profile in the Si starter (collector) layer is uniform at a concentration of $1\times10^{17}cm^{-3}$ as shown earlier in figure 3.5. The phosphorus profile in the Si cap (emitter) is not uniform, this is due to the very short growth time of this layer. We also notice a small phosphorus peak within the $Si_{1-x}Ge_x$ layer. This is due to an auto doping effect from phosphorus remaining on the wafer surface after the growth of the Si starter (collector) layer. However it is well below the boron concentration and hence does not create any

problem for a $Si_{1-x}Ge_x$ heterojunction bipolar transistor. Overall the profiles show good dual control of n-type and p-type dopants with a resulting structure which is suiatble for $Si_{1-x}Ge_x$ heterojunction bipolar transistors.

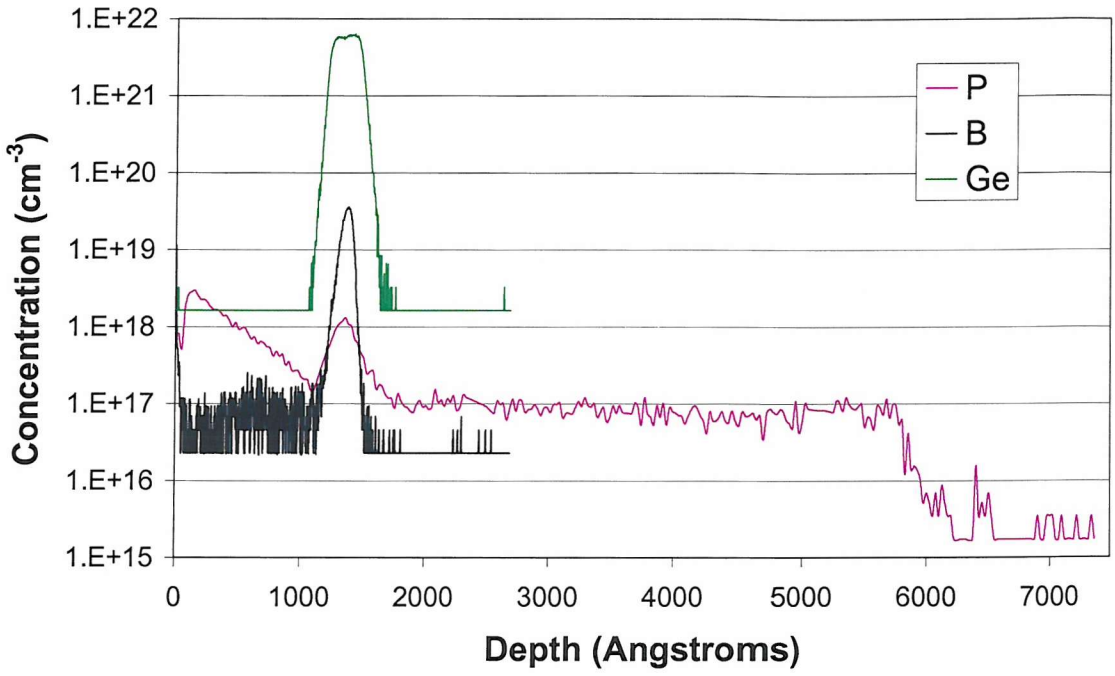

Figure 3.6: Geramanium, boron and phosphorus SIMS profiles of $Si_{1-x}Ge_x$ heterojunction bipolar transistor layers grown by non-selective epitaxy at 700°C in one step (growth number 2Si918 see table 3.1 for details).

Figure 3.7 shows a cross-sectional transmission electron microscopy micrograph of the optmised $Si_{1-x}Ge_x$ heterojunction bipolar transistor layers grown by non-selective epitaxy at 700°C in one step (growth number 2Si918 see table 3.1 for details). The dark uneven layer above the Si substrate is the growth interface, which consists of contaminants on the wafer surface, probabaly oxygen and carbon. The silicon layer above the growth interface is the Si starter (collector) layer. Hence, the growth interface is buried deep in the collector layer far away from the transistor's

base depletion region, where it could cause leakage. The darker layer above the Si starter (collector) layer is the strained Si_{1-x} Ge_x (base) layer. The top silicon cap layer is the emitter layer. All the device layers are smooth, planar, uniform and free of defects, indicating good growth control and good epitaxial quality.

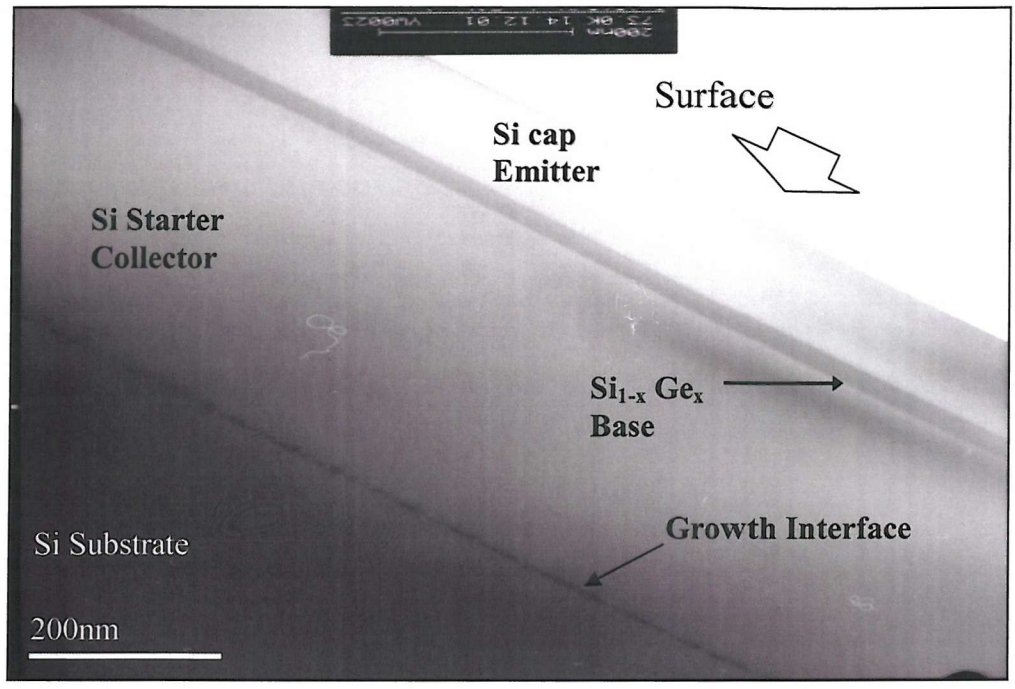

Figure 3.7: A cross-sectional transmission electron microscopy micrograph of Si_{1-x} Ge_x heterojunction bipolar transistor layers grown by non-selective epitaxy at 700°C in one step (growth number 2Si918 see table 3.1 for details).

Spectroellipsometry experimental and simulation fitted results are presented in figure 3.8. Psi Ψ and Delta Δ determine the differential changes in amplitude and phase, respectively, experienced upon reflection by the component vibrations of the electric vector parallel and perpendicular to the plan of incidence. The figure shows an excellent agreement between the experimental measurements (dotted lines) and the simulation fitted (solid lines) results. This indicates accuracy of the extracted layer compositions and thicknesses to be discussed later on (see table 3.2).

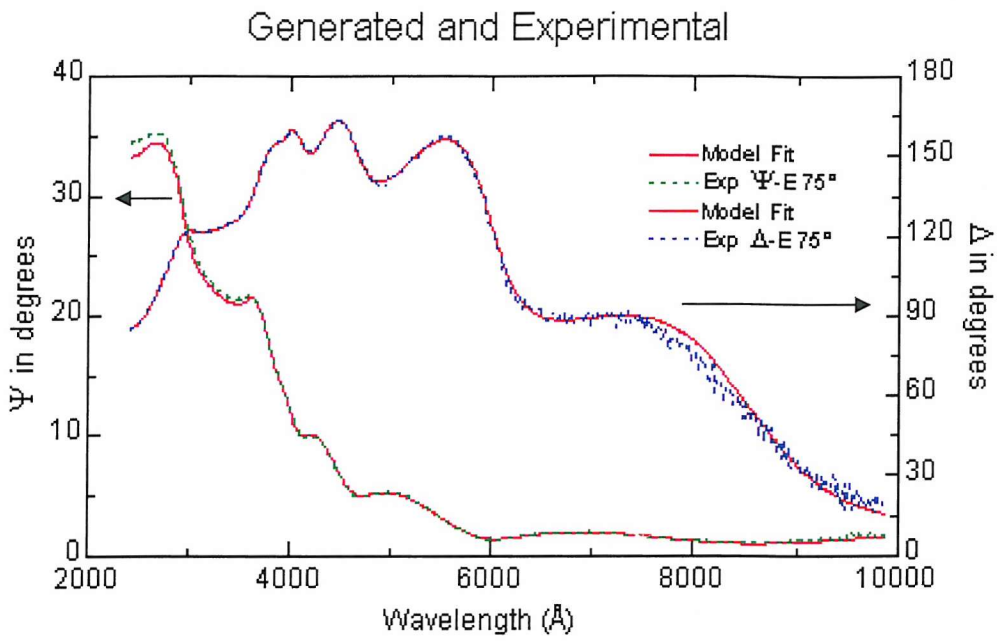

Figure 3.8: Spectroellipsometry experimental data (dotted lines), together with simulated data (solid lines) for Si_{1-x} Ge_x HBT layers grown at 700°C.

Table 3.2 shows the $Si_{1-x}Ge_x$ heterojunction bipolar transistor layer thicknesses of the sample shown in figure 3.7 (growth number 2Si918 see table 3.1 for details). The layer thicknesses were obtained from measurements on the SIMS profiles (see figure 3.6), and on the cross-sectional transmission electron microscopy (XTEM) micrograph of the layers (see figure 3.7) and spectroellipsometry analysis of the layers. The silicon starter (collector) layer thickness obtained from SIMS is 470nm, which agrees closely with the value obtained from XTEM, 480nm. The Si_{1-x} Ge_x (base) layer thickness obtained from SIMS is 31nm at a germanium concentration of 2%, which agrees closely with the thickness obtained from XTEM of 32nm. The Si_{1-x} Ge_x (base) layer thickness obtained from spectroellipsometry of 27nm for a Si_{1-x} Ge_x alloy of 5.4% Ge agrees with the thickness obtained from SIMS (26nm) at a germanium concentration of 5.4%. The silicon cap (emitter) layer thickness obtained from SIMS is slightly thinner than the value obtained from XTEM and

spectroellipsometry. Overall a good agreement is obtained for the different analysis methods used.

Layer	SIMS (nm)	XTEM (nm)	Elipsometry (nm)
Si starter layer	470±1	480±1	
SiGe layer (2% Ge)	31±1	32±1	
SiGe layer (5.4% Ge)	26±1		27±1
Si cap layer	111±1	140±1	130±1

Table 3.2: Comparative results obtained through three different techniques; SIMS, XTEM and Spectroellipsometry, for the thicknesses of the $Si_{1-x}Ge_x$ heterojunction bipolar transistor layers grown at 700°C (growth number 2Si918 see table 3.1 for details).

3.4 Conclusions

A $Si_{1-x}Ge_x$ heterojunction bipolar transistor layers growth process at 700°C has been developed controlling both n and p-type dopants in a single growth step. Control of the Si starter (collector) layer doping concentration was achieved by altering the growth temperature and the phosphine gas flow. The boron tailing edge into the Si cap (emitter) was removed by interrupting the growth with a 350sccm hydrogen flow for 5 minutes after the $Si_{1-x}Ge_x$ (base) layer growth but prior to the Si cap (emitter) layer growth. A $Si_{1-x}Ge_x$ HBT structure with a $Si_{1-x}Ge_x$ layer width of 31nm and a boron profile width of 22nm was obtained. The layer thicknesses were compared using three different analytical techniques; SIMS, TEM and spectroellipsometry and reasonable agreement was obtained.

References

1. J. A. Woollam, B. Johs, C. M. Herzinger, J. Hilfiker, R. Synowicki and C. L. Bungay; Critical Reviews of Optical Science and Technology, vol. CR72, p. 3, (1999).
2. R. T. Carline, C. Pickering, D. J. Robbins, W. Y. Leong, A. D. Pitt, and A. G. Cullis, "Spectroscopic ellipsometry of $Si_{1-x}Ge_x$ epilayers of arbitrary composition $0 \leq x \geq 0.255$"; Applied Physics Letters, vol. 64 (9), pp. 1114-1116, (1994).
3. C. Pickering and R. T. Carline, "Dielectric function spectra of strained and relaxed $Si_{1-x}Ge_x$ alloys (x = 0-0.25)"; Journal of Applied Physics, vol. 75 (9), pp. 4642-4647, (1994).
4. S. Zollner, J. Hildreth, R. Liu, P. Zaumseil, M. Weidner and B. Tillack, "Optical constants and ellipsometric thickness determination of strained $Si_{1-x}Ge_x$: C layers on Si (100) and related heterostructures"; Journal of Applied Physics, vol. 88 (7), pp. 4102-4108, (2000).
5. H. G. Tompkins, "A User's guide to Ellipsometry"; Academic Press Inc, United States of America, (1993).
6. E. Kasper, H. Kibbel, H. -J. Herzog and A. Gruhle, "Growth of 100GHz SiGe-heterobipolar transistor (HBT) structures"; Japanese Applied Physics Part 1 Regular Paper Short Note Review Paper, vol. 33 (4B), pp. 2415-2418, (1994).
7. J. M. Bonar, "Process development and characterization of silicon and silicon-germanium growth in a novel single-wafer LPCVD system"; Ph. D. thesis, Microelectronics Research Group, School of Electronics and Computer science, University of Southampton, United Kingdom, January (1996).

8. P. D. Agnello, T. O. Sedgwick and J. Cotte, "Growth rate enhancement of heavy n- and p-type doped silicon deposited by atmospheric pressure chemical vapour deposition at low temperatures"; Journal of the Electrochemical Society, vol. 140 (9), pp. 2703-2709, (1993).
9. R. Reif, T. I. Kamins and K. C. Saraswat, "A model for dopant incorporation into growing silicon epitaxial films: I. Theory"; Journal of the Electrochemical Society, vol. 126 (4), pp. 644-652, (1979).
10. A. J. Joseph, J. D. Cressler, D. M. Richey and G. Niu, "Optimisation of SiGe HBT's for operation at high current densities"; IEEE Transactions on Electron Devices, vol. 46 (7), pp. 1347-1354, (1999).

Chapter 4

The Effect of Fluorine Implantation Energy on Boron Diffusion in $Si_{1-x}Ge_x$

4.1 Introduction

The minimisation of boron diffusion is vitally important in all types of Si and $Si_{1-x}Ge_x$ devices. For example, in $Si_{1-x}Ge_x$ heterojunction bipolar transistors (HBTs) diffusion of boron from the $Si_{1-x}Ge_x$ base creates parasitic energy barriers that degrade the current gain and limit the value of cut-off frequency that can be achieved [1]. Recently, fluorine implantation has been investigated as an alternative method of suppressing boron diffusion in silicon and shown to be extremely effective [2-6]. However to the authors' knowledge, there have been no reports of the effects of fluorine on boron diffusion in $Si_{1-x}Ge_x$.

This chapter investigates the effect of varying F^+ implantation energy on boron thermal diffusion and boron transient enhanced diffusion (TED) in metastable $Si_{0.86}Ge_{0.14}$ by characterising the diffusion of a boron marker layer in samples with and without P^+ and F^+ implants. The effect of two F^+ implantation energies (185keV and 42keV) was studied at two anneal temperatures 950°C and 1025°C. In samples implanted with P^+ & 185keV F^+, the fluorine suppresses boron transient enhanced diffusion completely at 950°C and suppresses thermal diffusion by 44% at 1025°C. In samples implanted with P^+ & 42keV F^+, the fluorine does not reduce boron transient

enhanced diffusion at 950°C. This result is explained by the location of the boron marker layer in the vacancy-rich region of the fluorine damage profile for the 185keV implant, which could result in an under-saturation of interstitials and hence suppress boron diffusion. Whilst for the 42keV implant the boron marker layer is in the interstitial-rich region of the implant which could result in the enhanced diffusion observed. Isolated dislocation loops are seen in the $Si_{0.86}Ge_{0.14}$ layer of the 185keV implanted sample after anneal. We postulate that these loops are due to the partial relaxation of the metastable $Si_{0.86}Ge_{0.14}$ layer. A band of dislocation loops is seen in the $Si_{0.86}Ge_{0.14}$ layer of the 42keV implanted sample after anneal. This is attributed to implantation damage.

4.2 Experimental Procedure

Low pressure chemical vapour deposition (LPCVD) at 700°C was used to grow a 400nm Si starter layer, a 55nm $Si_{0.86}Ge_{0.14}$ layer and a 63 nm Si cap layer on a (100) silicon wafer. A boron doped marker layer was incorporated within the $Si_{0.86}Ge_{0.14}$ layer with a peak concentration of $4.1\times10^{19}cm^{-3}$. The wafer was cleaved into 1cm×1cm samples. Three types of samples were then produced from the same wafer; the first had no implants (unimplanted), the second a phosphorus and a low energy fluorine implant (P^+ & low F^+) and the third a phosphorus and a high energy fluorine implant (P^+ & high F^+). A 288keV, $6\times10^{13}cm^{-2}$ P^+ implant was chosen to be similar to those used for a selective implanted collector in a bipolar process, which causes boron transient enhanced diffusion [7]. The low energy F^+ was implanted at 42KeV, $9x10^{14}cm^{-2}$, with the energy chosen to give a fluorine peak (at 0.09μm) which is approximately coinciding with the as grown boron peak (at 0.1μm). The high

energy F^+ was implanted at 185KeV, $2.3x10^{15}cm^{-2}$, with the energy chosen to give a fluorine peak coinciding with the implanted phosphorus peak (at 0.41μm). The phosphorus and fluorine implantations were done at the EPSRC Ion Implantation Centre at Surrey University. After ion implantation the samples were cleaned by a 10 minutes dip in fuming nitric acid followed by rinsing with DI water and blow drying using a nitrogen gun. The samples were then arranged side by side on the platen of an AG rapid thermal annealing RTA system using dummy bits in order to complete a 4 inch wafer area, such that there were no free edges in order to reduce heat loss, and annealed in nitrogen at either 950°C or 1025°C for 30s. Boron (B11), fluorine (F19) and germanium (Ge 74) concentration depth profiles were obtained on all samples by Secondary Ion Mass Spectroscopy (SIMS) at Loughborough Surface Analysis Ltd. SIMS was performed using O_2^+ primary ion bombardment and positive secondary ion detection to optimise boron detection. Similar detection levels of fluorine (F19) were obtained using O_2^+ primary ion bombardment as were obtained by using Cs^+ primary ion bombardment. Hence, the use of O_2^+ primary ion bombardment was preferentially used to allow the relative positions of boron and fluorine to be monitored by profiling them simultaneously. The O_2^+ beam at 10keV with 0.8μA current was rastered over a 250μm square. The data was quantified using ion implanted reference materials of boron and fluorine in silicon and the depth scales were determined by measuring the sputtered crater depths by interference microscopy, which is accurate to ±10nm. The samples were also analysed by Transmission Electron Microscopy (TEM) by Dr. Yun Wang at Surrey University.

4.3 Results

Figure 4.1(a) shows boron SIMS profiles in unimplanted samples and samples implanted with P^+ and 42keV F^+ (P^+ & low F^+) and with P^+ and 185keV F^+ (P^+ & high F^+) and annealed for 30s at 950°C in nitrogen. Boron and germanium profiles after growth are also shown for reference. The annealed boron profile of the P^+ & high F^+ implanted sample almost coincides with that of the unimplanted sample with slightly less diffusion. However, the annealed boron profile of the P^+ & low F^+ implanted sample is much broader, showing greater diffusion than the unimplanted and the P^+ & high F^+ implanted samples. Comparing the distance diffused by the boron into the silicon starter layer at a concentration of $1\times10^{17}cm^{-3}$, the least diffusion is seen for the P^+ & high F^+ implanted sample (14nm) followed by the unimplanted sample (18nm) and the largest diffusion is seen for the P^+ & low F^+ implanted sample (41nm). This indicates that a high energy fluorine implant has suppressed boron transient enhanced diffusion and slightly reduced boron thermal diffusion (by 4nm) at 950°C, whereas a low energy fluorine implant has not suppressed boron transient enhanced diffusion caused by the phosphorus implant (see figures 5.1 and 6.1 in chapters 5 and 6 respectively). Figure 4.1(b) shows boron SIMS profiles for a P^+ & high F^+ implanted sample and an unimplanted sample after an anneal of 30s at 1025°C. The annealed boron profile of the P^+ & high F^+ implanted sample is much narrower than that of the unimplanted sample indicating that the fluorine implant has significantly reduced boron thermal diffusion. Comparing the distance diffused by the boron in to the silicon starter layer at a concentration of $1\times10^{17}cm^{-3}$, we find that the distance diffused by boron in the P^+ & high F^+ implanted sample (23nm) is 18nm less than that for the unimplanted sample (41nm). This indicates that the P^+ & high F^+ implant has

suppressed boron transient enhanced diffusion and reduced boron thermal diffusion by 44% at 1025°C.

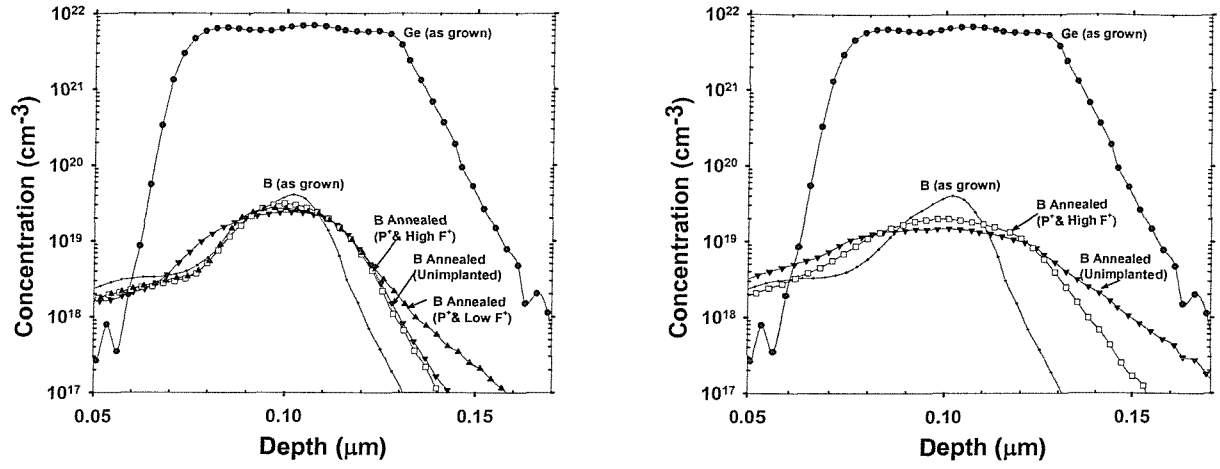

(a) (b)

Figure 4.1: Boron SIMS profiles in $Si_{0.86}Ge_{0.14}$ after growth and after anneal for an unimplanted sample and samples implanted with P^+ & low F^+ and with P^+ & high F^+; (a) 950°C anneal (b) 1025°C anneal.

Figure 4.2 compares the as implanted and annealed (at 950°C for 30s) fluorine profiles for the samples implanted with P^+ & low F^+ (a) and with P^+ & high F^+ (b). The annealed fluorine profile of the P^+ & low F^+ implanted sample shown in figure 4.2(a) shows two peaks at depths of 0.05μm and 0.1μm. The shallowest F^+ peak at a depth of 0.05μm is located in the silicon cap layer and the peak at 0.1μm is located completely within the $Si_{0.86}Ge_{0.14}$ layer and coincides with the boron profile. This peak is slightly deeper than the implant range (0.09μm) with a concentration of $3\times10^{20}cm^{-3}$, which is ≈ 4× higher than the as implanted peak concentration of

$8\times10^{19}cm^{-3}$. The annealed fluorine profile of the P^+ & high F^+ implanted sample shown in figure 4. 2(b) shows five peaks at depths of 0.02μm, 0.1μm, 0.14μm, 0.5μm, 0.6μm, a broad peak at 0.4μm and a shoulder between 0.16μm and 0.26μm. The shallowest F^+ peak at a depth of 0.02μm is located in the silicon cap layer. The 0.1μm and 0.14μm peaks are located completely within the $Si_{0.86}Ge_{0.14}$ layer, and the 0.1μm peak has a peak concentration of $4.7\times10^{19}cm^{-3}$, which is ≈ 11× higher than the corresponding concentration after implant of $4.2\times10^{18}cm^{-3}$. The broad peak at 0.4μm coincides with the implant range 0.41μm and has a peak concentration of $1\times10^{20}cm^{-3}$, slightly higher than the as implanted peak concentration of $8.6\times10^{19}cm^{-3}$. The peak at depth of 0.5μm coincides with the growth interface. The integrated doses of the fluorine SIMS profiles after anneal are $8.2\times10^{14}cm^{-2}$ and $2.2\times10^{15}cm^{-2}$ for the P^+ & low F^+ and P^+ & high F^+ implanted samples respectively. This indicates that very little (8.9% for the P^+ & low F^+ and 4.3% for the P^+ & high F^+ implanted samples respectively) fluorine has been lost during anneal in both samples.

Figure 4.3 compares the as implanted and annealed (at 1025°C for 30s) fluorine profiles for the samples implanted with P^+ & low F^+ (a) and with P^+ & high F^+ (b). The profiles are qualitatively similar to those shown in figure 4.2, except there are no surface fluorine peaks compared to those seen before in figure 4.2. For the P^+ & low F^+ (figure 4.3 (a)) profile shows two peaks at depths of 0.077μm and 0.09μm. The shallowest F^+ peak at a depth of 0.077μm is located at the Si-$Si_{0.86}Ge_{0.14}$ interface and the peak at 0.09μm is located completely within the $Si_{0.86}Ge_{0.14}$ layer and coincides with the implant range (0.09μm) with a concentration of $2.2\times10^{20}cm^{-3}$, which is ≈ 2.8× higher than the as implanted peak concentration of $8\times10^{19}cm^{-3}$. Notice that this peak in the $Si_{0.86}Ge_{0.14}$ layer has shifted closer to the surface compared to that

in figure 4.2(a). For the P^+ & high F^+ (figure 4.3 (b)) profile the peak concentrations in the $Si_{0.86}Ge_{0.14}$ layer ($2.1\times10^{19}cm^{-3}$ at 0.1μm and $4.4\times10^{18}cm^{-3}$ at 0.14μm) have decreased compared to those in figure 4.2(b) ($4.7\times10^{19}cm^{-3}$ at 0.1μm and $3.3\times10^{19}cm^{-3}$ at 0.14μm). Also a visible peak extending from 0.16μm to 0.26μm is visible in figure 4.3 (b), whereas a shoulder was seen in figure 4.2(b). The integrated doses of the fluorine SIMS profiles after anneal are $5.1\times10^{14}cm^{-2}$ and $1.8\times10^{15}cm^{-2}$ for the P^+ & low F^+ and the P^+ & high F^+ implanted samples respectively. This corresponds to dose losses of 43% for the P^+ & low F^+ and 22% for the P^+ & high F^+ implanted samples respectively.

Figure 4.4 shows light field cross-sectional TEM micrographs of a sample implanted with P^+ & low F^+ and annealed at 1025°C. No defects are seen in the silicon starter and cap layers in figure 4.4 (a). However, defects can be seen in the $Si_{0.86}Ge_{0.14}$ layer. These are observed more closely in the high magnification micrograph of figure 4.4 (b) and consist of a band of dislocation loops, with various lengths (56nm to 100nm) extending along the top interface of the silicon germanium layer.

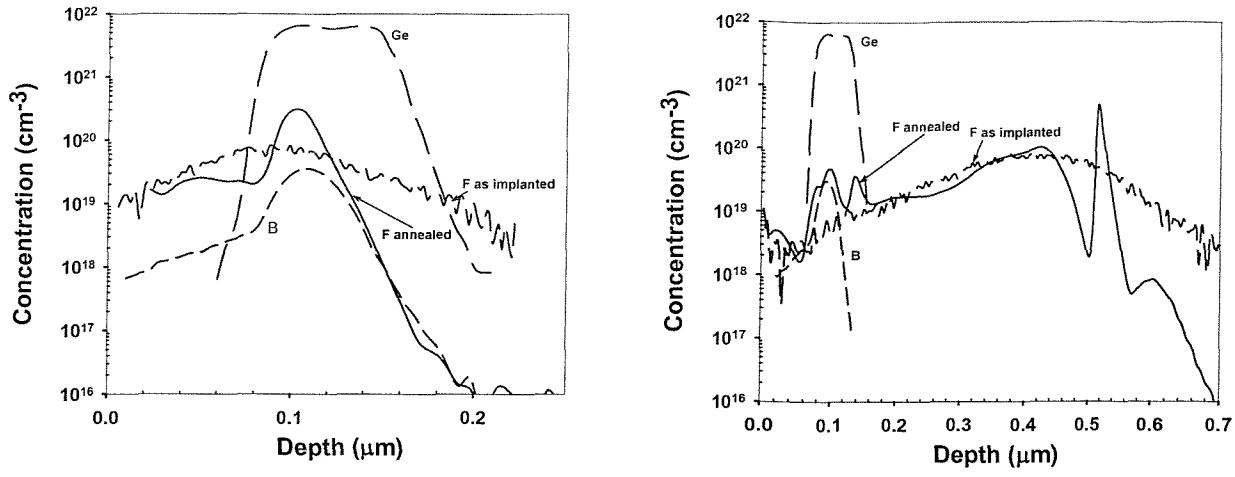

Figure 4.2: Fluorine SIMS profiles in samples implanted with (a) P^+ & low F^+ and (b) P^+ & high F^+ after implant and after anneal for 30s at 950°C in nitrogen.

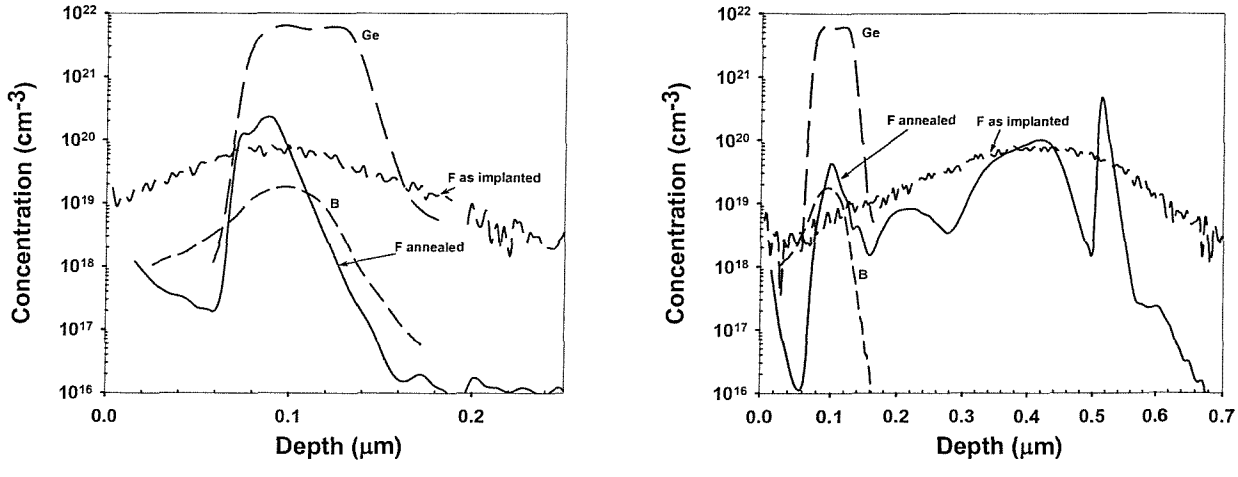

Figure 4.3: Fluorine SIMS profiles in samples implanted with (a) P^+ and low F^+ and (b) P^+ and high F^+ after implant and after anneal for 30s at 1025°C in nitrogen. The corresponding boron and germanium profiles are also shown for reference in both figures 4.2 and 4.3.

Figure 4.5 shows light field cross-sectional TEM micrographs of a sample implanted with P^+ & high F^+ and annealed at 1025°C. A band of dislocation loops extending from a depth of 0.31μm to a depth of 0.63μm from the surface centred around the P^+ & high F^+ implants range of 0.41μm can be seen in figure 4.5 (a). Defects can also be seen in the $Si_{0.86}Ge_{0.14}$ layer (see figure 4.5 (b) for a high magnification view of these defects) consisting of isolated adjacent dislocation loops, each loop having a width of ≈ 46nm and a length of ≈ 108nm and extending across the $Si_{0.86}Ge_{0.14}$ layer from the bottom to the top surface.

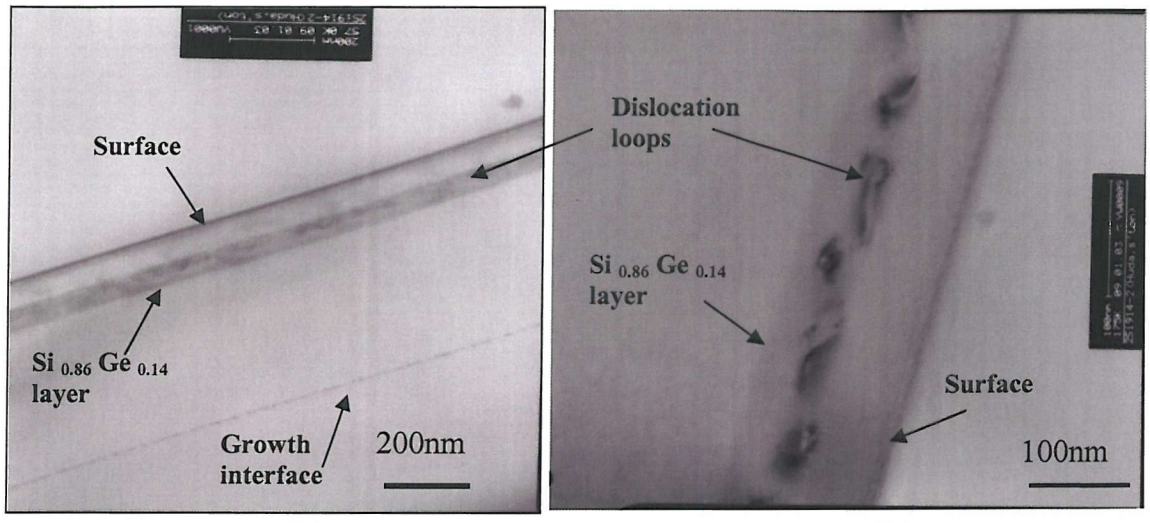

(a) (b)

Figure 4.4: Cross-sectional transmission electron microscopy micrographs of samples implanted with P^+ & low F^+ and annealed for 30s at 1025°C in nitrogen; (a) low magnification, (b) high magnification.

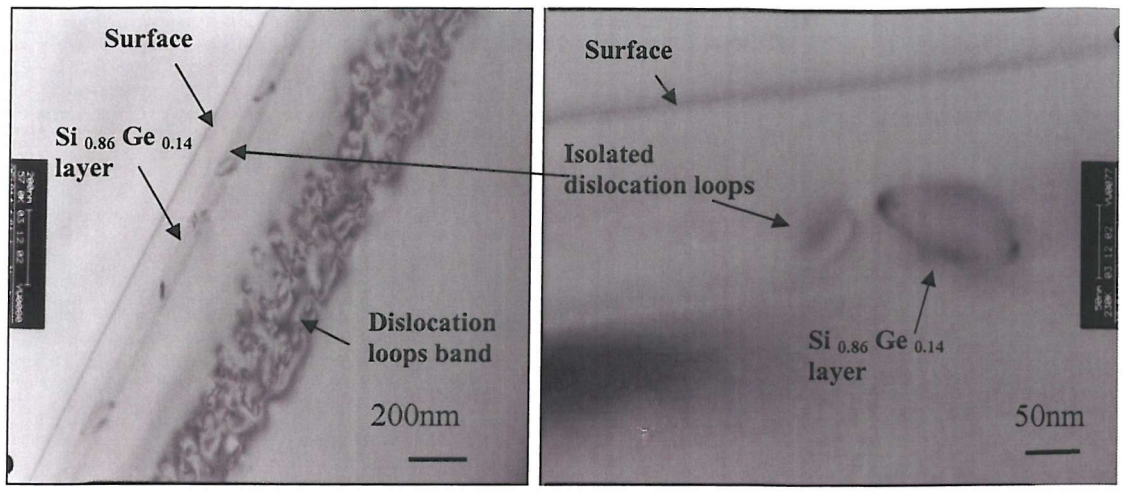

(a) (b)

Figure 4.5: Cross-sectional transmission electron micrographs of samples implanted with P^+ & high F^+ and annealed for 30s at 1025°C in nitrogen; (a) low magnification, (b) high magnification.

4.4 Discussion

The results in figure 4.1 show that a high energy fluorine implant completely suppresses boron transient enhanced diffusion at 950°C, whereas a low energy fluorine implant gives no suppression of boron transient enhanced diffusion caused by the phosphorus implant (seen in figures 5.1 and 6.1 in chapters 5 and 6 respectively). Furthermore, a high energy fluorine implant also suppresses boron thermal diffusion by 44% at 1025°C. The suppression of boron transient enhanced diffusion for the high energy fluorine implant agrees with the results of Liu et al [3] who showed that increasing the fluorine implantation energy from 2keV to 12keV ($2\times10^{15}cm^{-2}$), resulted in increased suppression of boron transient enhanced diffusion in silicon of an implanted boron profile (1.12keV $1\times10^{15}cm^{-2}$, B^+) caused by a preamorphising silicon implant (70keV $1\times10^{15}cm^{-2}$, Si^+).

The suppression of boron thermal diffusion in silicon or silicon germanium by a high energy F^+ implant has not been reported before in the literature and can be explained by the location of the boron marker layer in the vacancy rich region of the high energy F^+ implant damage profile, which extends from the surface to a depth approaching the implantation range R_p [8], perhaps leading to an under saturation in the interstitials concentration. This mechanism is discussed fully in chapters 5 and 6. The lack of boron diffusion suppression in the P^+ & low F^+ implanted samples can then be explained by the location of the boron marker layer in the interstitial rich region of the low energy F^+ implant damage profile, which extends from a depth slightly shallower than the implantation range R_p and peaks at the implantation range R_p [8].

The fluorine profiles after anneal shown in figures 4.2 and 4.3 have interesting shapes giving insight into fluorine diffusion in silicon and silicon germanium. We notice that more fluorine has been lost during the higher temperature (1025°C) anneal in both samples compared to the lower temperature (950°C) anneal which would be expected. Also at both anneal temperatures the % loss in fluorine dose during anneal is greater for the lower energy implant than the higher energy implant. This suggests that the surface may be having an influence on the fluorine diffusion and hence affecting the shape of the annealed fluorine profiles. The influence of the surface can be seen in the presence of the surface peak (at 0.02μm and 0.05μm) after a 950°C anneal (figure 4.2), but its absence after a 1025°C anneal (figure 4.3). The origin of these surface fluorine peaks will be explained later in chapter 6. The influence of the surface can also be seen in the movement of the peak in the $Si_{0.86}Ge_{0.14}$ layer in the P^+ & low F^+ implanted sample closer towards the surface after a 1025°C anneal (figure 4.3 (a)) than after a 950°C anneal (figure 4.2 (a)). This indicates that fluorine when

annealed diffuses outwards to the surface from which it is lost resulting in the dose loss seen. The high energy fluorine implant range (0.41μm) is ≈ 4.6× deeper than that of the low energy fluorine implant (0.09μm), which is closer to the surface and hence fluorine diffuses out from the surface more easily in the low energy fluorine implanted sample resulting in the larger % dose loss seen. This agrees with reports in the literature which indicate that fluorine diffuses to the surface from which it is lost [9].

Correlating the annealed fluorine SIMS profiles in figure 4.3 with the TEM micrographs shown in figures 4.4 and 4.5, we notice that the fluorine peaks seen in the silicon germanium layers in figure 4.3 (a) and (b) coincide with the dislocation loops seen in figure 4.4 (b) and figure 4.5 (b) respectively. We also notice that the broad fluorine peak at 0.4μm and the peaks at 0.5 and 0.6μm in figure 4.3 (b) coincide with the band of dislocation loops in the silicon starter layer extending from a depth of 0.31μm to a depth of 0.63μm from the surface seen in figure 4.5(a). Hence, the fluorine peaks observed in figure 4.3 (a) and (b) result from fluorine gettering to the dislocation loops observed in figures 4.4 and 4.5 respectively. Similar dislocation loops were reported due to a 500keV $5x10^{15}cm^{-2}$ F^+ implant where SIMS showed fluorine gettering to the dislocation loops [10].

The dislocation loops seen in figure 4.4 (b) in the $Si_{0.86}Ge_{0.14}$ layer, which extends from a depth of 0.064μm to 0.118μm corresponding to 0.7 R_p to 1.3 R_p (where R_p is the implantation range of the low energy F^+ implant 0.09μm), are in the interstitial-rich region of the low energy fluorine implant damage profile, which extends from a depth slightly shallower than the implantation range R_p and peaks at the implantation range R_p [8]. The band of dislocation loops in the silicon starter layer seen in figure 4.5(a) extend from a depth of 0.31μm to a depth of 0.63μm from the

surface corresponding to 0.7 R_p to 1.5 R_p (where R_p is the implantation range of the high energy F^+ implant 0.41μm) and hence are also in the interstitial-rich region of the high energy fluorine implant damage profile [9]. SUSPRE [11] simulations show that the P^+ & low F^+ implant was below the amorphisation threshold. TEM micrographs of as-implanted samples (see figure 6.14 in chapter 6) show that the silicon and silicon germanium layers have not been amorphised by the P^+ & high F^+ implants. Hence, these dislocation loops in both the P^+ & low F^+ and P^+ & high F^+ implanted samples are both most probably due to sub amorphising implantation damage [12].

The dislocation loops seen in the $Si_{0.86}Ge_{0.14}$ layer in figure 4.5, which extends from a depth of 0.064μm to 0.118μm corresponding to 0.16 R_p to 0.29 R_p (where R_p is the implantation range of the high energy F^+ implant 0.41μm), are in the vacancy-rich region of the high energy fluorine implant, which extends from the surface to a depth approaching the implantation range R_p [8] and hence are unlikely to be due to sub amorphising implantation damage. We speculate that these dislocation loops are due to partial relaxation of the strain in the $Si_{0.86}Ge_{0.14}$ layer. The 55nm thick $Si_{0.86}Ge_{0.14}$ layer is metastable (the critical thickness at 14% Ge is ≈ 40nm) (see figure 2.2) [13], hence, relaxation is possible after a high temperature anneal. This point is backed by results shown later in chapter 6, where a cross-sectional TEM micrograph of a stable 30nm thick $Si_{0.89}Ge_{0.11}$ layer (the critical thickness at 11% Ge is ≈ 60nm) (see figure 2.2) [13], which has been given the same P^+ and F^+ implants as the P^+ & high F^+ implanted sample and annealed at 1000°C for 30s in nitrogen is presented in figure 6.15 showing no dislocation loops in the $Si_{0.89}Ge_{0.11}$ layer.

4.5 Conclusions

In conclusion a study of the effect of varying F^+ implantation energy on boron thermal diffusion and boron transient enhanced diffusion (TED) in $Si_{0.86}Ge_{0.14}$ has been shown. It has been shown that a high energy fluorine implant completely suppresses boron transient enhanced at 950°C, whereas a low energy fluorine implant gives no suppression of boron TED. Furthermore, a high energy fluorine implant also suppresses boron thermal diffusion by 44% at 1025°C. The suppression of boron transient enhanced diffusion and thermal diffusion by a high energy F^+ implant is explained by the location of the boron marker layer in the vacancy-rich region of the fluorine implant damage profile and the lack of any TED suppression for the low energy fluorine implant is explained by the location of the boron marker layer in the interstitial-rich region of the fluorine implant damage profile. Isolated dislocation loops are seen in the $Si_{0.86}Ge_{0.14}$ layer of the sample given a high energy F^+ implant. These loops are in the vacancy-rich region of the fluorine implant damage profile and we postulate that they are due to partial relaxation of the metastable $Si_{0.86}Ge_{0.14}$ layer.

References

1. Md. R. Hashim, R. F. Lever and P. Ashburn, "2D simulation of transient enhanced boron out-diffusion from the base of a SiGe HBT due to an extrinsic base implant"; Solid State Electronics, vol. 43, pp. 131-140, (1999).
2. K. Ohyu, T. Itoga and N. Natsuaki, "Advantages of fluorine introduction in boron implanted shallow p+/n junction formation"; Japanese Journal of Applied Physics, vol. 29, pp. 457-462, (1990).
3. L. S. Robertson, P. N. Warnes, K. S. Jones, S. K. Earles, M. E. Law, D. F. Downey, S. Falk and J. Liu. "Junction depth reduction of ion implanted boron in silicon through fluorine ion implantation"; Materials Research Society Symposium Proceedings, vol. 610, pp. B4.2.1-B4.2.6, (2000).
4. T. S. Shano, R. Kim, T. Hirose, Y. Furuta, H. Tsuji, M. Furuhashi and K. Taniguchi, "Realization of ultra –shallow junction: suppressed boron diffusion and activation by optimized fluorine co-implantation"; Technical Digest of the International Electron Device Meeting IEDM, pp. 37.4.1-37.4.4, (2001).
5. M. Diebel, S. Chakravarthi, C. F. Machala, S. Ekbote, A. Jain and S. T. Dunham, "Investigation and modelling of fluorine co-implantation effects on dopant redistribution"; Materials Research Society Symposium Proceedings; vol. 765, pp. D6.15.1-D6.15.6, (2003).
6. K. Liu, J. Wu, J. Chen, A. Jain, "Fluorine assisted super-halo for sub-50nm transistors"; IEEE Electron Device Letters; vol. 24, pp. 180-182, (2003).
7. B. Martinet, H. Baudry, O. Kermarree, Y. Campidelli, M. Laurens, M. Marty, T. Schwartzmann, A. Monroy, D. Bensahel and A. Chantre, "100GHz SiGe:C HBTs using non selective base epitaxy"; Proceedings of the European Solid State Device Research Conference ESSDERC, pp. 97-100, (2001).

8. M. D. Giles, "Transient phosphorus diffusion below the amorphization threshold"; Journal of the Electrochemical Society, vol. 138, pp. 1160-1165, (1991).

9. S.-P. Jeng, T.-P. Ma, R. Canteri, M. Anderle and G. W. Rubloff, "Anomalous diffusion of fluorine in silicon"; Applied Physics Letters, vol. 61 (11), pp. 1310-1312, (1992).

10. X. D. Pi, C. B. Burrows and P. G. Coleman, "Fluorine in Silicon: Diffusion, Trapping and Precipitation", Physical Review Letters, vol. 90 (15), pp.155901-1-115901-4, (2003).

11. SUSPRE, University of Surrey, United Kingdom.

12. K. S. Jones, S. Prussin and E. R. Weber, "A systematic Analysis of defects in ion implanted silicon"; Applied Physics A Solids and Surfaces, vol. 45, pp. 1-34, (1988).

13. E. Kasper and H. -J. Herzog, "Elastic strain and misfit dislocation density in $Si_{0.92}Ge_{0.08}$ films on silicon substrates"; Thin Solid Films, vol. 44, pp. 357-370, (1977).

Chapter 5

Reduction of Boron Thermal Diffusion in Silicon by High Energy Fluorine Implantation

5.1 Introduction

While there has been considerable research on the effect of fluorine on boron transient enhanced diffusion in silicon [1-19], little has been published on the effects of fluorine on the thermal diffusion of boron in silicon. In this chapter, a study is made of the effect of fluorine on the diffusion of boron in buried marker layers in silicon. In the first section of this chapter samples with and without a P^+ implant are studied so that the effect of fluorine on both boron transient enhanced diffusion and thermal diffusion can be separately characterised. It is shown that fluorine not only eliminates boron transient enhanced diffusion, but also dramatically reduces boron thermal diffusion. The effect of the fluorine implantation dose on boron thermal diffusion in silicon is also studied in the second section of this chapter. It is shown that a critical fluorine dose exists, above which the fluorine suppresses boron thermal diffusion and below which it has no effect on the boron thermal diffusion.

5.2 Experimental Procedure

Silicon layers with and without a buried boron-doped marker layer were grown on (100) silicon wafers using molecular beam epitaxy (MBE) at 520°C and low pressure chemical vapour deposition (LPCVD) at 800°C respectively. The molecular beam epitaxy samples were grown by Dr. Rob Price at Imperial College, London. Each wafer was then cleaved into 1cm×1cm square pieces, which were then separated into four different groups, the first having no implants (unimplanted), the second having a phosphorus implant only (P^+ implanted), the third a phosphorus and a fluorine implant (P^+ & F^+ implanted) and the fourth a fluorine implant only (F^+ implanted). A 288keV, $6\times10^{13}cm^{-2}$ P^+ implant was used and was chosen to be similar to those used for a selective implanted collector in a bipolar process [20]. A 185KeV F^+ implant was used and the energy was selected such that the fluorine range was the same as that of the phosphorus implant. The fluorine implantation dose was varied from $5\times10^{14}cm^{-2}$ to $2.3\times10^{15}cm^{-2}$ in the fluorine only implanted samples. The phosphorus and fluorine implantations were carried out at the EPSRC Ion Implantation Centre at Surrey University. After ion implantation the samples were cleaned by a 10 minute dip in fuming nitric acid followed by rinsing with DI water and blow drying using a nitrogen gun. The samples were then arranged side by side on the platen of an AG rapid thermal annealing RTA system using dummy bits in order to complete a 4 inch wafer area, such that there were no free edges in order to reduce heat loss, and annealed in nitrogen at 1000°C for 30s. Boron (B11) and fluorine (F19) concentration depth profiles were obtained on all samples by Secondary Ion Mass Spectroscopy (SIMS) at Loughborough Surface Analysis Ltd. SIMS was performed using O_2^+ primary ion bombardment and positive secondary ion detection to optimise boron detection. Similar detection levels of fluorine (F19) were

obtained using O_2^+ primary ion bombardment as were obtained by using Cs^+ primary ion bombardment. Hence, the use of O_2^+ primary ion bombardment was preferentially used to allow the relative positions of boron and fluorine to be monitored by profiling them simultaneously. The O_2^+ beam at 10keV with 0.8μA current was rastered over a 250μm square. The data was quantified using ion implanted reference materials of boron and fluorine in silicon and the depth scales were determined by measuring the sputtered crater depths by interference microscopy, which is accurate to ±10nm. The layers were also analysed by Transmission Electron Microscopy (TEM) (done at ST, Catania, Italy). The annealed boron SIMS profiles peaks were aligned to the as-grown boron SIMS profile peak and the boron doses in all profiles were normalised to the as-grown boron profile dose. This reduces errors in dose and depth scaling arising from SIMS analysis. The annealed boron profiles were then fitted using the Silvaco, Athena Optimizer. This was done by importing the as-grown and annealed boron SIMS profiles into a silicon layer defined in the ATHENA input file (as shown in Appendix A). The intrinsic boron diffusion coefficient (Dix.0 Athena parameter) was then optimised with all other factors turned off (as shown in Appendix B), using the fully coupled diffusion model, until a good fit was obtained between the fitted and measured SIMS boron profiles.

5.3 Results

5.3.1 The Effect of a High Energy Fluorine Implant on Boron Diffusion in Silicon

Figure 5.1 shows the effect of a P^+ implant on the boron diffusion in the absence of a F^+ implant. It can be seen that the P^+ implant causes significant extra

diffusion of the boron marker layer compared with the unimplanted control sample. Comparing the boron profiles at a concentration of $1x10^{17}cm^{-3}$, we find that the width of the P^+ implanted boron profile is 138nm, compared with 108nm for the unimplanted boron profile and 48nm for the as-grown boron profile. The boron diffusion into the substrate of the P^+ implanted sample (56nm) is 25nm more than that of the unimplanted sample (31nm). This translates to an enhancement factor of 81% in boron diffusion due to the phosphorus implant. This result indicates that the phosphorus implant is giving rise to transient enhanced diffusion of boron. We also notice that the boron profile in the P^+ implanted sample is asymmetrical, with more diffusion into the substrate (56nm) than in to the silicon cap (33nm). This is due to the backflow of excess interstitials from beyond the as implanted phosphorus peak; similar asymmetries have been reported previously for boron transient enhanced diffusion caused by a silicon implant [21]. Similar boron transient enhanced diffusion caused by a similar $6\times10^{13}cm^{-2}$ P^+ implant was reported [20]. Similar enhanced boron diffusion caused by a P^+ implant was observed by Lee *et al.* [22] and characterised as transient enhanced diffusion. This was verified by a study of the boron enhanced diffusion by a P^+ implant for three anneal temperatures 750°C, 800°C and 950°C and it was shown that the enhanced boron diffusion was reduced as the anneal temperature was increased. This is characteristic of transient enhanced diffusion as for higher anneal temperatures the interstitials recombination rate is higher resulting in less boron transient enhanced diffusion [22].

Figure 5.2 shows the effect of a 185keV, $2.3\times10^{15}cm^{-2}$ F^+ implant on boron transient enhanced diffusion in samples implanted with P^+. It is clear that there is dramatically less boron diffusion in the sample implanted with both P^+ & F^+. Comparing the boron profiles at a concentration of $1\times10^{17}cm^{-3}$, we observe that the

diffusion of boron into the substrate in the P^+ & F^+ implanted sample (14nm) is 42nm less than that in the P^+ implanted sample (56nm), which indicates that the F^+ implant has reduced the boron diffusion by 75%. We also observe that the diffusion of boron into the substrate in the P^+ & F^+ implanted sample (14nm) is 17nm less than that in the unimplanted sample (31nm). This indicates that the F^+ implant has not only totally suppressed the boron transient enhanced diffusion caused by the P^+ implant but has also greatly reduced the thermal diffusion by 55%.

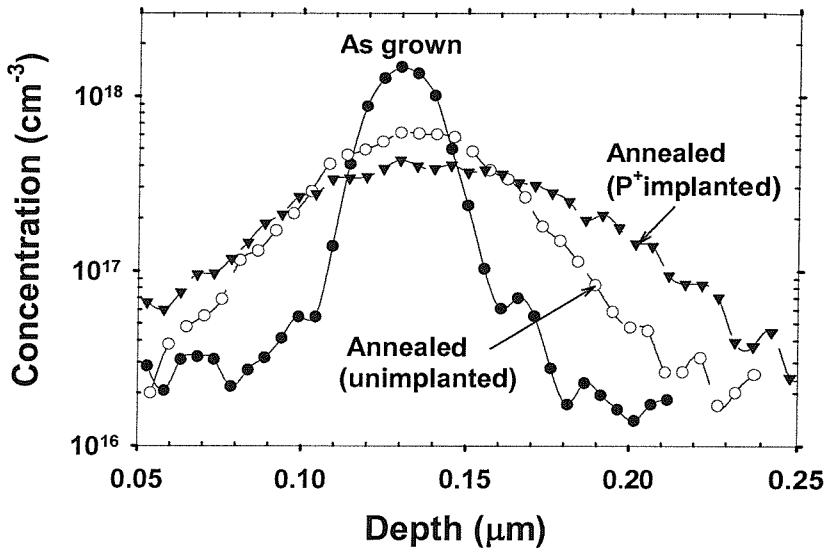

Figure 5.1: Boron SIMS profiles of unimplanted and P^+ implanted samples after a 30s anneal at 1000°C in nitrogen. The as-grown boron profile is added for reference.

Figure 5.3 shows the effect of a 185keV, $2.3\times10^{15}cm^{-2}$ F^+ implant on boron thermal diffusion in samples not given a P^+ implant. It can be seen that there is considerably less diffusion in the sample implanted with F^+ than in the unimplanted sample. Comparing the boron profiles at a concentration of $1x10^{17}cm^{-3}$ we find that the diffusion of boron into the substrate for the F^+ implanted sample (11nm) is 20nm less than that in the unimplanted sample (31nm), which indicates that the F^+ implant has reduced the thermal boron diffusion by 65%.

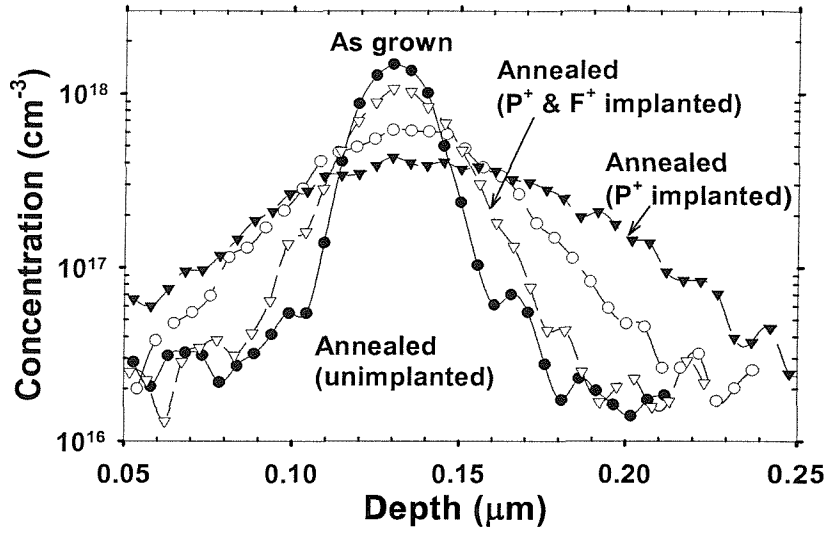

Figure 5.2: Boron SIMS profiles of unimplanted, P^+ implanted and P^+ & $2.3\times10^{15}cm^{-2}$ F^+ implanted samples after a 30s anneal at 1000°C in nitrogen. The as-grown boron profile is added for reference.

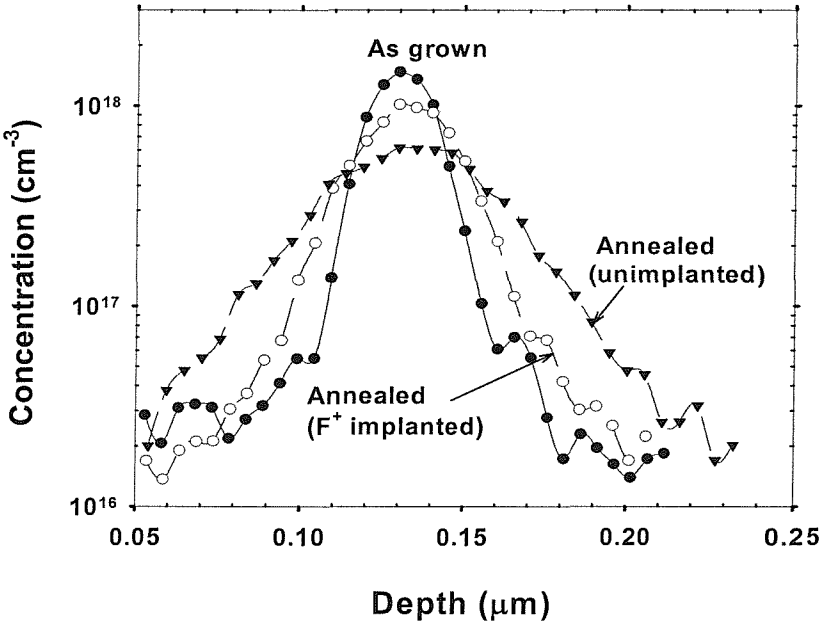

Figure 5.3: Boron SIMS profiles of unimplanted and $2.3\times10^{15}cm^{-2}$ F^+ implanted samples after a 30s anneal at 1000°C in nitrogen. The as-grown boron profile is added for reference.

Figure 5.4 compares the fluorine profiles of the P^+ & F^+ implanted sample discussed in figure 5.2, before and after anneal at 1000°C for 30s in nitrogen. The corresponding boron profile is shown for reference. The annealed fluorine profile is considerably different than the as-implanted profile and shows two broad peaks. The deeper broad peak lies within a depth range of 0.29μm to 0.73μm with a peak concentration of $8.31x10^{19}cm^{-3}$ at a depth of 0.41μm. This peak concentration almost coincides with the as-implanted peak concentration of $8.32x10^{19}cm^{-3}$ at a depth of 0.41μm. The shallower peak lies between 0.055μm and 0.23μm, coinciding with the boron profile, and shows four small peaks at depths of 0.11μm, 0.12μm, 0.15μm and 0.17μm. A slight shoulder can also be seen, extending from about 0.22 to 0.28μm. The integrated dose of the as-implanted fluorine SIMS profile is $2.3\times10^{15}cm^{-2}$ and the integrated fluorine dose after anneal is $1.5\times10^{15}cm^{-2}$, indicating that 35% of the implanted fluorine has been lost during annealing. The majority of the fluorine lost comes from the shallow fluorine peak and shoulder regions, i.e. from the surface to a depth of 0.28μm, but there is also some loss of fluorine from the deep peak region (0.29μm to 0.8μm).

Figure 5.5 compares the fluorine profiles of the F^+ implanted sample discussed in figure 5.3, before and after anneal at 1000°C for 30s in nitrogen. The corresponding boron profile is shown for reference. The annealed fluorine profile is broadly similar to that in figure 5.4. The deeper peak lies between 0.28 μm to 0.57μm from the surface. The fluorine concentration rises higher than the as implanted concentration within a depth range of 0.4μm to 0.46μm, with a peak concentration of $9.11x10^{19}cm^{-3}$ at a depth of 0.43μm. This peak concentration is slightly higher and deeper than the as-implanted peak concentration of $8.32\times10^{19}cm^{-3}$, at a depth of 0.41μm.

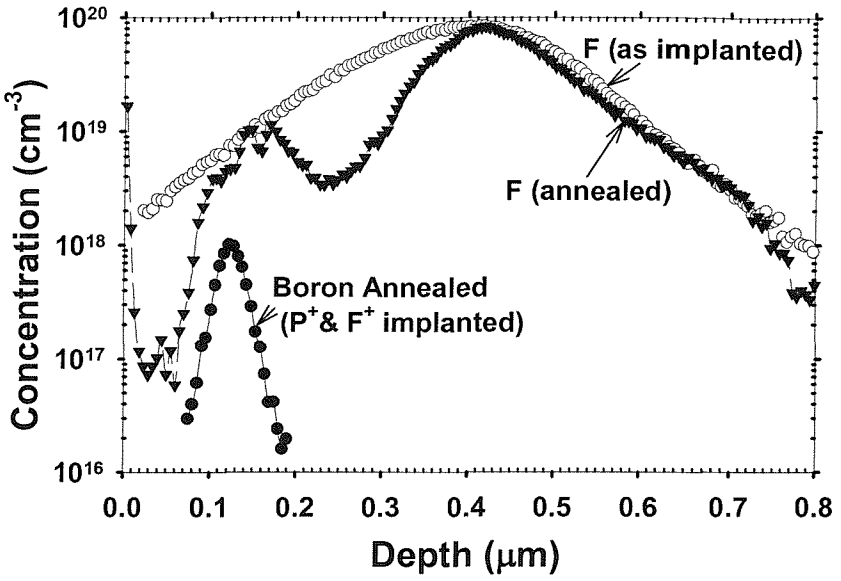

Figure 5.4: Comparison of fluorine profiles before and after anneal for 30s at 1000°C in nitrogen for the P^+ & $2.3\times10^{15}cm^{-2}$ F^+ implanted sample. The corresponding annealed boron profile is added for reference.

The shallower peak lies between 0.05μm and 0.22μm and shows three small peaks at depths of 0.13μm, 0.17μm and 0.2μm. A substantial shoulder can also be seen, extending from about 0.22 to 0.28μm. The integrated fluorine dose after anneal is $1.6\times10^{15}cm^{-2}$, indicating that 30% of the implanted fluorine has been lost during annealing. The majority of the fluorine lost comes from the shallow fluorine peak and shoulder regions, i.e. from the surface to a depth of 0.28μm, but there is also some loss of fluorine from the deep peak region (0.29μm to 0.8μm). Notice that the fluorine lost from the substrate beyond a depth of 0.57μm is $6.7\times10^{13}cm^{-2}$, which is 7.3 times more than that lost in figure 5.4, $0.9\times10^{13}cm^{-2}$.

Figure 5.6 shows a comparison of the fitted and measured SIMS boron profiles of the samples discussed earlier in figures 5.1, 5.2 and 5.3. In all the figures the fitted profile agrees with the SIMS profile indicating a reasonable fit. Figure 5.6 (a) shows the fitted boron profile of the annealed unimplanted sample. The diffusion coefficient extracted is $8.1x10^{-14}cm^2/s$, which is the inert boron diffusion coefficient at 1000°C for this material. Figure 5.6 (b) shows the fitted boron profile of the annealed P^+ implanted sample. The diffusion coefficient extracted for the P^+ implanted sample is $2.3x10^{-13}cm^2/s$, which is 2.8 times greater than that of the unimplanted sample. This indicates that the phosphorus implant has enhanced the boron diffusion coefficient by a factor of $\approx$3. Figure 5.6 (c) shows the fitted boron profile of the annealed P^+ & F^+ implanted sample. The diffusion coefficient extracted for the P^+ & F^+ implanted sample is $2.1x10^{-14}cm^2/s$, which is 11 times less than that of the P^+ implanted sample and 3.9 times less than that of the unimplanted sample. The diffusion coefficient extracted for the F^+ implanted sample is $2.2x10^{-14}cm^2/s$, which is very similar to that of the P^+ & F^+ implanted sample ($2.1x10^{-14}cm^2/s$) and is 3.7 times less than that of the unimplanted sample. This shows that the fluorine implant has eliminated the transient enhanced diffusion caused by the phosphorus implant and also reduced the thermal diffusion by a factor of 3.9.

Figure 5.7 shows cross-sectional transmission electron microscopy micrographs of the P^+ &F^+ implanted sample (a) and the F^+ implanted sample (b) after an anneal at 1000°C for 30s in nitrogen, discussed in figures 5.4 and 5.5 respectively. In both figures 5.7 (a) and (b) the region from the surface to a depth of 0.29μm is smooth with no visible defects and a band of dislocation loops is seen from a depth of 0.29μm to a depth of 0.73μm, centred around the implantation range of 0.41μm.

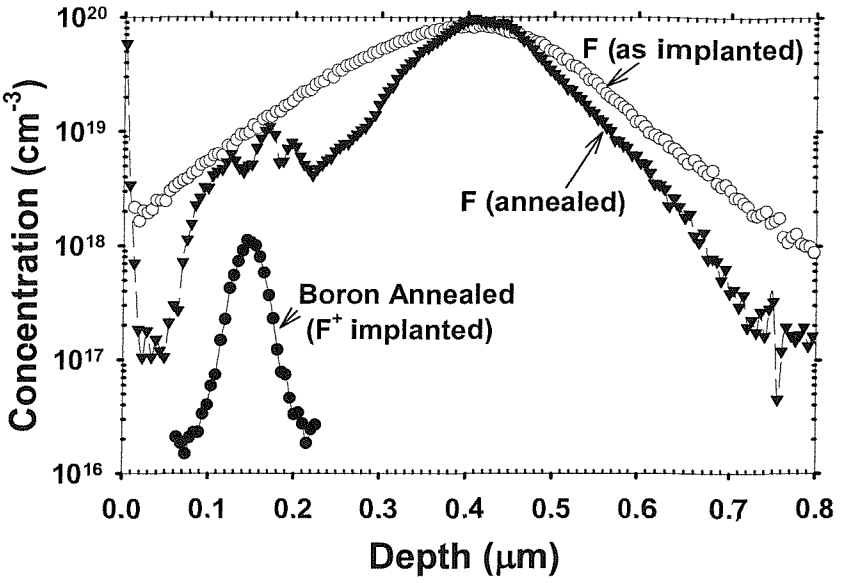

Figure 5.5: Comparison of fluorine profiles before and after anneal for 30s at 1000°C in nitrogen for the $2.3\times10^{15}cm^{-2}$ F^+ implanted sample. The corresponding annealed boron profile is shown for reference.

Figure 5.8 shows high magnification cross-sectional transmission electron microscopy micrographs of the defects regions of the P^+ &F^+ implanted sample (a) and the F^+ implanted sample (b) discussed in figure 5.7. The defects seen in both figures 5.8 (a) and (b) are very similar and consist mainly of dislocation loops with diameters varying from 11nm to 96nm.

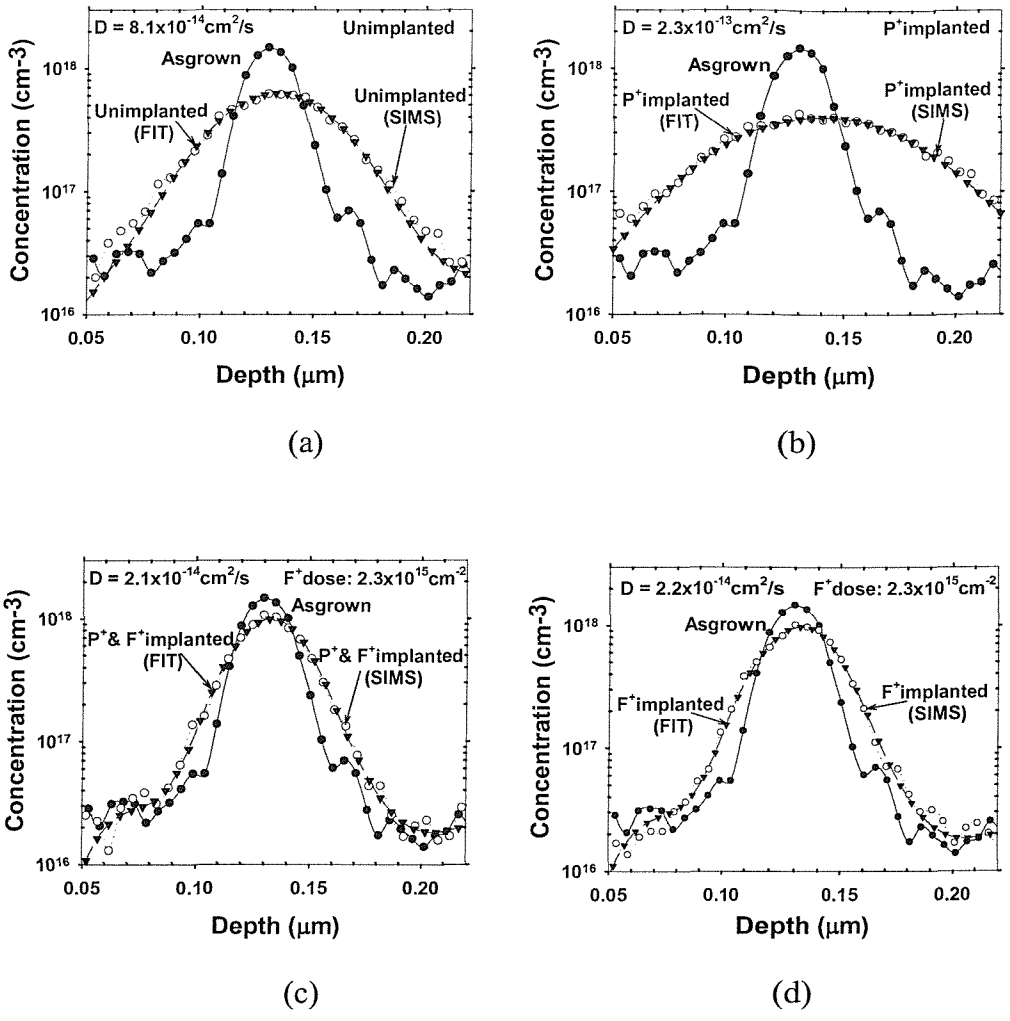

Figure 5.6: Simulated and measured boron profiles after an anneal of 30s at 1000°C in nitrogen for: unimplanted (a), P^+ implanted (b), P^+ & F^+ implanted (c) and F^+ implanted (d) samples. The as-grown boron profile is added for reference.

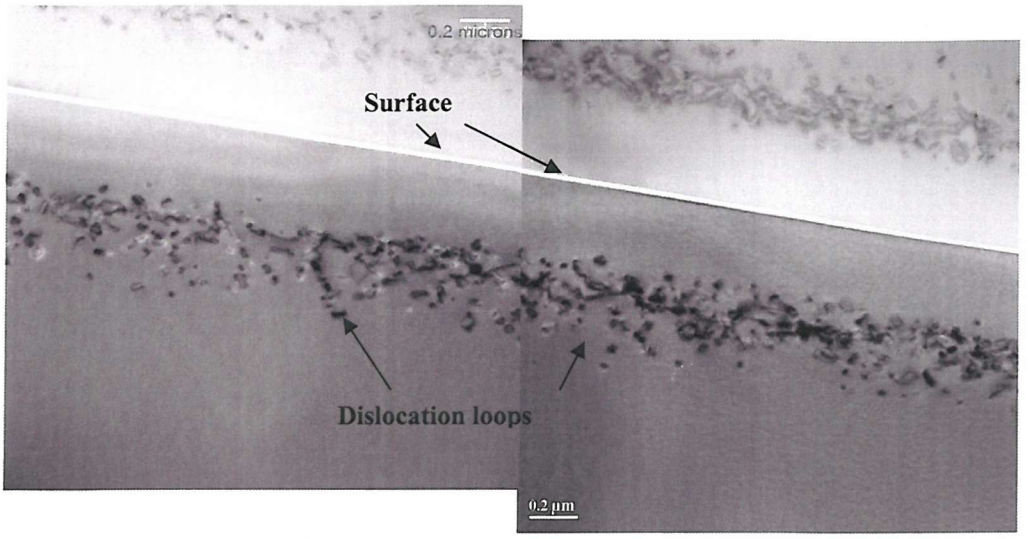

(a) (b)

Figure 5.7: Cross-sectional transmission electron microscopy micrographs of $2.3\times10^{15}cm^{-2}$ F^+ implanted and annealed Si MBE layers (a) P^+ & F^+ implanted sample and (b) F^+ implanted sample.

(a) (b)

Figure 5.8: High magnification cross-sectional transmission electron microscopy micrographs of $2.3\times10^{15}cm^{-2}$ F^+ implanted and annealed Si MBE layers (a) P^+ & F^+ implanted sample and (b) F^+ implanted sample.

5.3.2 The Effect of Fluorine Implantation Dose on Boron Thermal Diffusion in Silicon

Figure 5.9 shows a comparison of boron SIMS profiles in F^+ implanted and unimplanted samples after an anneal at 1000°C for 30s in nitrogen. The as-grown boron profile is also included for reference. Results are shown for fluorine implantation doses of $5\times10^{14}cm^{-2}$ (figure 5.9 (a)), $9\times10^{14}cm^{-2}$ (figure 5.9 (b)) and $1.4\times10^{15}cm^{-2}$ (figure 5.9 (c)). For the lowest fluorine dose of $5\times10^{14}cm^{-2}$ the fluorine implanted boron profile width (100nm) at a concentration of $1x10^{17}cm^{-3}$ is 8nm wider than that of the unimplanted profile (92nm),perhaps indicating a slight enhancement in boron diffusion. The width of the boron profile of the $9\times10^{14}cm^{-2}$ fluorine implanted sample (92nm) is exactly the same as that of the unimplanted sample, indicating that the fluorine implant had no effect on the boron thermal diffusion. The width of the boron profile of the $1.4\times10^{15}cm^{-2}$ fluorine implanted sample (78nm) is 14nm less than that of the unimplanted sample (92nm) indicating that the fluorine has suppressed the boron thermal diffusion. The boron diffusion length into the substrate at a concentration of $1x10^{17}cm^{-3}$ of the $1.4\times10^{15}cm^{-2}$ fluorine implanted sample (10nm) is 9nm less than that of the unimplanted sample (19nm) indicating a 47% reduction in thermal diffusion. The reduction in thermal diffusion in the $2.3\times10^{15}cm^{-2}$ fluorine implanted sample is 65% as shown earlier in figure 5.3. These results show that a critical fluorine dose between $9\times10^{14}cm^{-2}$ and $1.4\times10^{15}cm^{-2}$ is needed before fluorine shows a reduction effect on the thermal diffusion of boron in silicon at 1000°C and that the reduction in thermal diffusion increases as the fluorine dose increases.

Figure 5.10 shows a comparison of simulated and measured boron profiles of F^+ implanted and unimplanted samples after an anneal at 1000°C for 30s in nitrogen. The as-grown boron profile is also included for reference. Results are shown for the unimplanted sample (figure 5.10 (a)) and for fluorine implantation doses of $5\times10^{14}cm^{-2}$ (figure 5.10 (b)), $9\times10^{14}cm^{-2}$ (figure 5.10 (c)), and $1.4\times10^{15}cm^{-2}$ (figure 5.10 (d)). In all figures the fitted profiles coincide very well with the measured profiles, indicating a good fit.

The extracted values of diffusion coefficient for the unimplanted and F^+ implanted samples with F^+ doses of $5\times10^{14}cm^{-2}$ to $2.3\times10^{15}cm^{-2}$ are summarised in table 5.1. The value for the $2.3\times10^{15}cm^{-2}$ F^+ implanted sample is that shown earlier in figure 5.6 (d) and is normalised to the unimplanted diffusion coefficient shown in figure 5.6 (a). The extracted diffusion coefficient for the lowest F^+ implantation dose of $5\times10^{14}cm^{-2}$ ($7.6\times10^{-14}cm^2/s$) is slightly higher than that of the unimplanted sample ($5.9\times10^{-14}cm^2/s$) as expected from figure 5.9 (a). However, the difference is small and is discounted by results in chapter 6, which show that for the same fluorine dose of $5\times10^{14}cm^{-2}$ the extracted boron diffusion coefficient is very similar to that of the unimplanted sample (see table 6.4). The extracted diffusion coefficient for a F^+ implantation dose of $9\times10^{14}cm^{-2}$ ($5.3\times10^{-14}cm^2/s$) is almost equal to that of the unimplanted sample ($5.9\times10^{-14}cm^2/s$) as expected from figure 5.9 (b). For the two highest F^+ implantation doses of $1.4\times10^{15}cm^{-2}$ and $2.3\times10^{15}cm^{-2}$ the extracted diffusion coefficients are factors of 1.9 and 3.7 × lower than the diffusion coefficients of the corresponding unimplanted samples respectively.

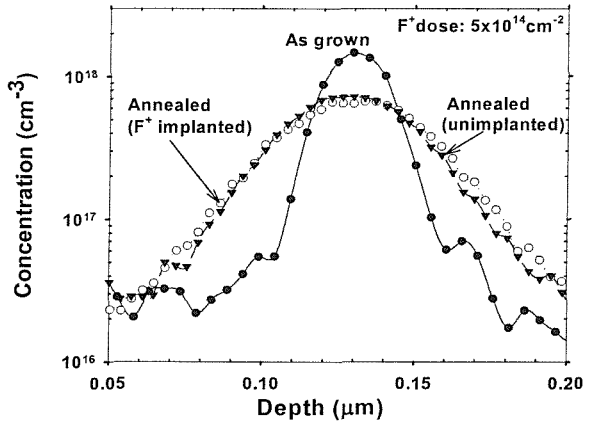

(a)

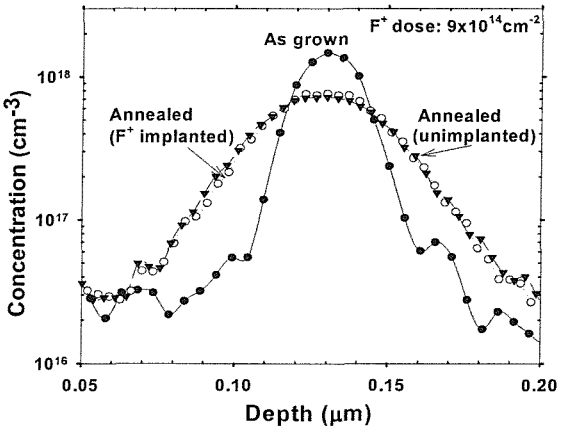

(b)

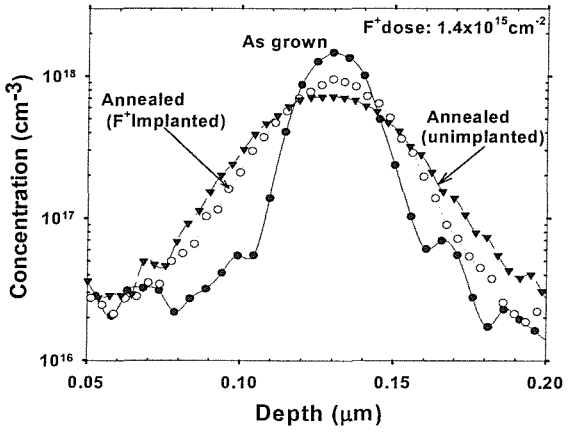

(c)

Figure 5.9: Boron SIMS profiles in F^+ implanted and unimplanted samples after a 30s anneal at 1000°C in nitrogen. The as-grown boron profile is also included for reference. Results are shown for fluorine implantation doses of (a) $5\times10^{14}cm^{-2}$, (b) $9\times10^{14}cm^{-2}$ and (c) $1.4\times10^{15}cm^{-2}$.

F^+ Implant Dose (cm^{-2})	Boron Diffusion Coefficient (cm^2/s)	Normalised Boron Diffusion Coefficient	Reduction Factor
Unimplanted	5.9×10^{-14}	1	
5×10^{14}	7.6×10^{-14}	1.3	-
9×10^{14}	5.3×10^{-14}	0.9	-
1.4×10^{15}	3.1×10^{-14}	0.52	1.9
2.3×10^{15}	2.2×10^{-14}	0.27	3.7

Table 5.1: A summary of the extracted boron diffusion coefficients for unimplanted samples and samples implanted with F^+ doses of $5\times10^{14}cm^{-2}$ to $2.3\times10^{15}cm^{-2}$.

Figure 5.11 compares the fluorine SIMS profiles before and after an anneal at 1000°C for fluorine implantation doses of $5\times10^{14}cm^{-2}$ (figure 5.11 (a)), $9\times10^{14}cm^{-2}$ (figure 5.11 (b)), $1.4\times10^{15}cm^{-2}$ (figure 5.11 (c)) and $2.3\times10^{15}cm^{-2}$ (figure 5.11 (d)). The corresponding boron profiles are added for reference. For all the implanted doses the as-implanted fluorine profile is approximately gaussian with an implantation range of 0.41μm. For the lowest fluorine implantation dose of $5\times10^{14}cm^{-2}$, negligible fluorine is present (SIMS background level) in the vicinity of the boron profile after anneal. The majority of the fluorine is located in a broad double peak at a depth corresponding approximately with the range of the fluorine implant (0.41μm). This deep fluorine peak extends from a depth of about 0.3μm to 0.64μm. For a fluorine implantation dose of $9\times10^{14}cm^{-2}$, negligible fluorine is again visible in the vicinity of the boron profile, but a small shoulder can be seen on the surface side of the deep fluorine peak between about 0.22 and 0.28μm. This shoulder was not present for the lower fluorine dose of $5\times10^{14}cm^{-2}$ in figure 5.11 (a). For the highest fluorine dose of $1.4\times10^{15}cm^{-2}$, an additional shallow, fluorine peak can be clearly seen in the vicinity of the boron marker layer, extending from about 0.07μm to 0.22μm. The shape of this

shallow fluorine peak is complex and comprises two small ripples at depths of 0.16 and 0.18μm. A substantial shoulder can also be seen at a similar depth as the shoulder seen in figure 5.11 (b) (≈ 0.22-0.28μm).

Figure 5.12 shows fluorine SIMS profiles in samples with and without a boron marker layer after a fluorine implant of $5\times10^{14}cm^{-2}$ (figure 5.12 (a)), $9\times10^{14}cm^{-2}$ (figure 5.12 (b)), $1.4\times10^{15}cm^{-2}$ (figure 5.12 (c)) or $2.3\times10^{15}cm^{-2}$ (figure 5.12 (d)) and an anneal at 1000°C. The fluorine profiles in the samples without the boron marker layer show the same overall trends as those with the boron marker layer. For all fluorine doses, a broad fluorine peak is seen at a depth corresponding approximately with the range of the fluorine implant. For the lowest F^+ dose of $5\times10^{14}cm^{-2}$, there is negligible fluorine in the vicinity of the boron profile. For a fluorine dose of $9\times10^{14}cm^{-2}$, there is again negligible fluorine in the vicinity of the boron profile, but a shoulder can be seen between about 0.22 and 0.28μm. For the highest doses of $1.4\times10^{15}cm^{-2}$ and $2.3\times10^{15}cm^{-2}$, an additional shallow fluorine peak can be seen in the vicinity of the boron profile, extending from approximately 0.07 to 0.22μm. A substantial shoulder can also be seen, extending from about 0.22 to 0.28μm. The shape of the additional shallow fluorine peak in the samples without a boron marker layer is different than in those with the boron marker layer. In the former samples a single broad peak is present at a depth of 0.16μm, whereas in the latter samples small ripples can be seen. It should be noted that the samples with the boron marker layer were grown using molecular beam epitaxy, whereas the samples without the boron marker layer were grown using low pressure chemical vapour deposition. However, the difference in the as-grown point defect concentration in the layers grown by the two different methods will not directly affect the fluorine profile. This is because the point defects created by the fluorine implantation damage is by far greater than the

intrinsic as-grown point defect concentration and thus these ion implantation generated point defects which are the same regardless of the epitaxy method are responsible for the fluorine diffusion profile after anneal. The small ripples seen on the samples with the boron marker layer may therefore be an artefact of the growth method, due to the trapping of fluorine at interfaces created by short growth interrupts during the boron doped layer growth by molecular beam epitaxy.

Table 5.2 summarises the integrated fluorine doses in different regions of the profiles before and after anneal. The fluorine doses after implant obtained by integrating the SIMS profiles are in reasonable agreement with the implanted dose, indicating that the SIMS profiles are reasonably accurate. The total fluorine doses after anneal indicate that considerable fluorine is lost during anneal, varying from 30% for the highest F^+ implant dose of $2.3\times10^{15}cm^{-2}$ to 56% for the lowest implant dose of $5\times10^{14}cm^{-2}$. For all implant doses the majority of the fluorine after anneal is located in the deep fluorine peak, which is defined as extending from 0.28μm to 0.70μm. For example, for the highest F^+ implant dose of $2.3\times10^{15}cm^{-2}$, 94% of the fluorine resides in the deep fluorine peak after anneal. This percentage is even higher for the other fluorine doses. For F^+ doses of 1.4 and $2.3\times10^{15}cm^{-2}$, where suppression of boron thermal diffusion is seen, approximately 2.5% and 5.2% respectively of the fluorine resides in the shallow fluorine peak and 1.8% and 2.9% respectively resides in the shoulder.

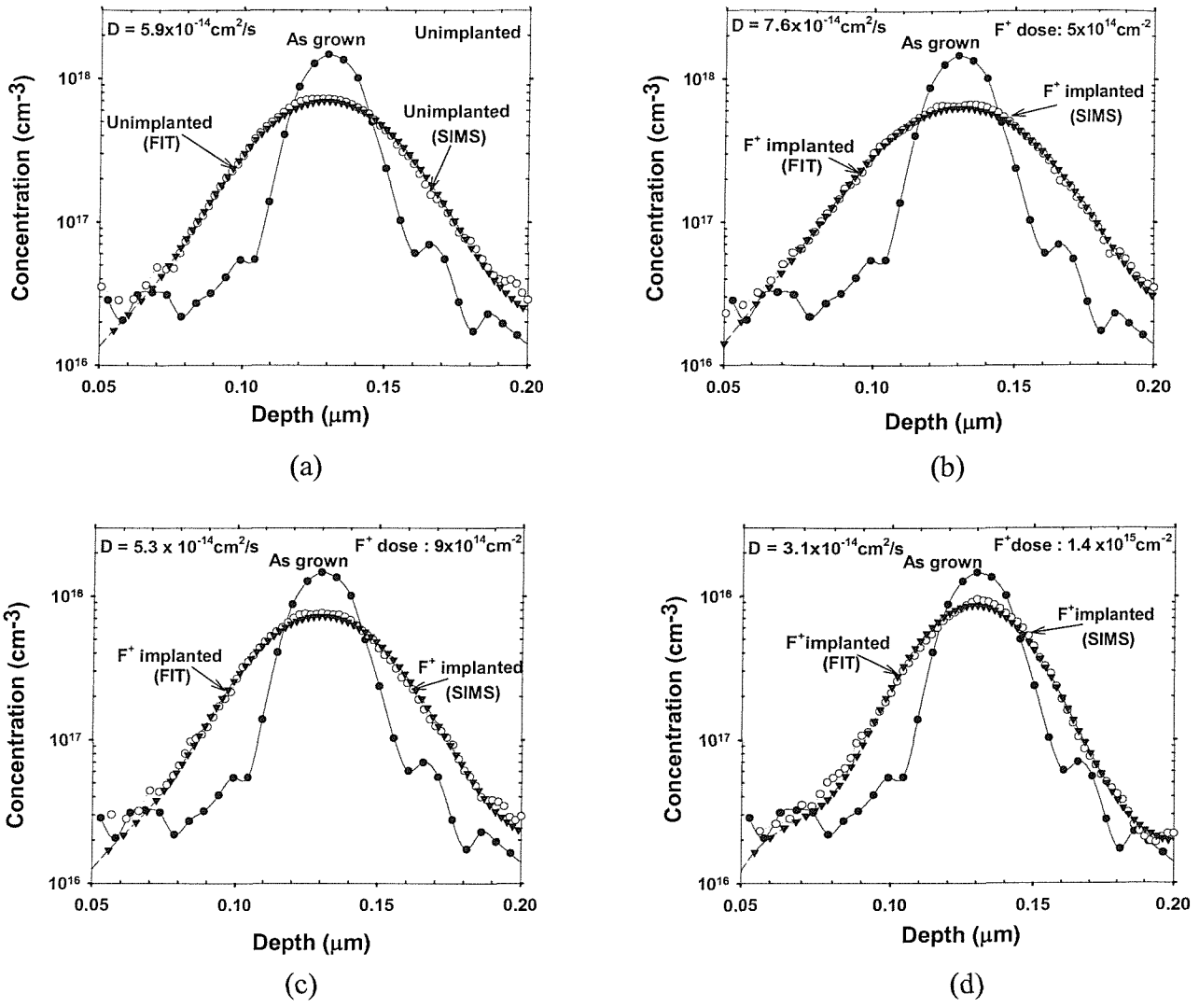

Figure 5.10: Simulated and measured boron profiles after an anneal of 30s at 1000°C in nitrogen for an unimplanted sample (a) and samples implanted with F^+ doses of : $5\times10^{14}cm^{-2}$(b), $9\times10^{14}cm^{-2}$ (c) and $1.4\times10^{15}cm^{-2}$ (d). The as-grown boron profile is added for reference.

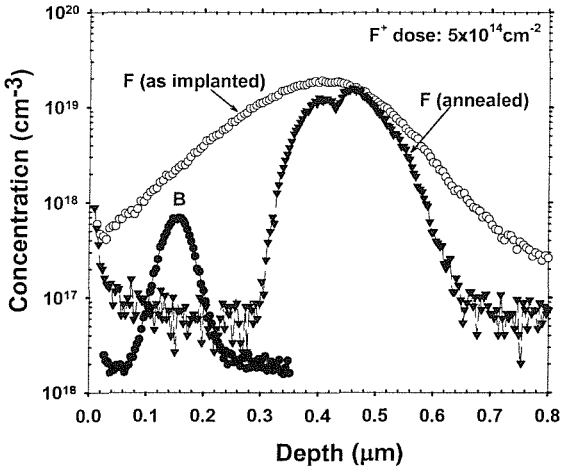

(a)

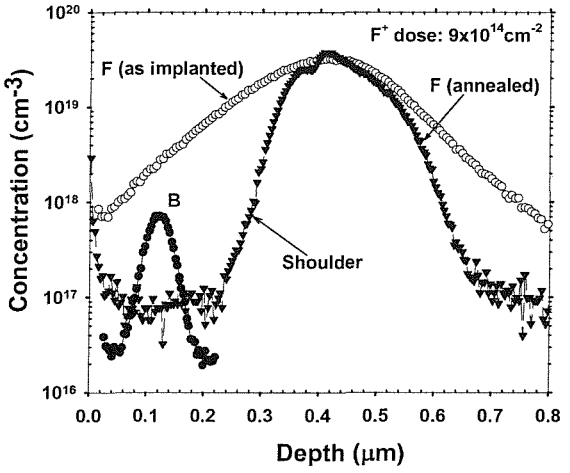

(b)

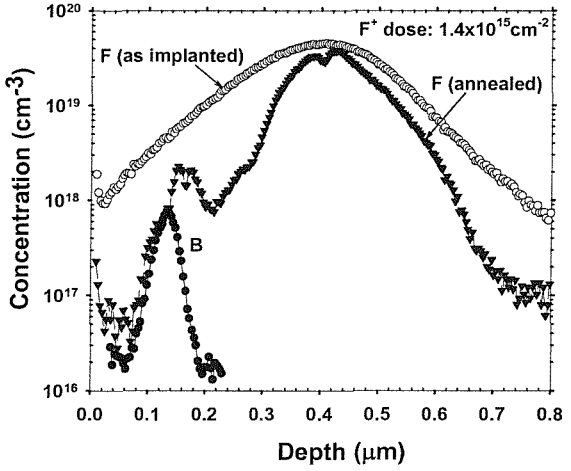

(c)

Figure 5.11: Fluorine SIMS profiles before and after a 30s anneal at 1000°C. Boron profiles after anneal are also included for reference. Results are shown for fluorine implantation doses of (a) $5\times10^{14}cm^{-2}$, (b) $9\times10^{14}cm^{-2}$ and (c) $1.4\times10^{15}cm^{-2}$.

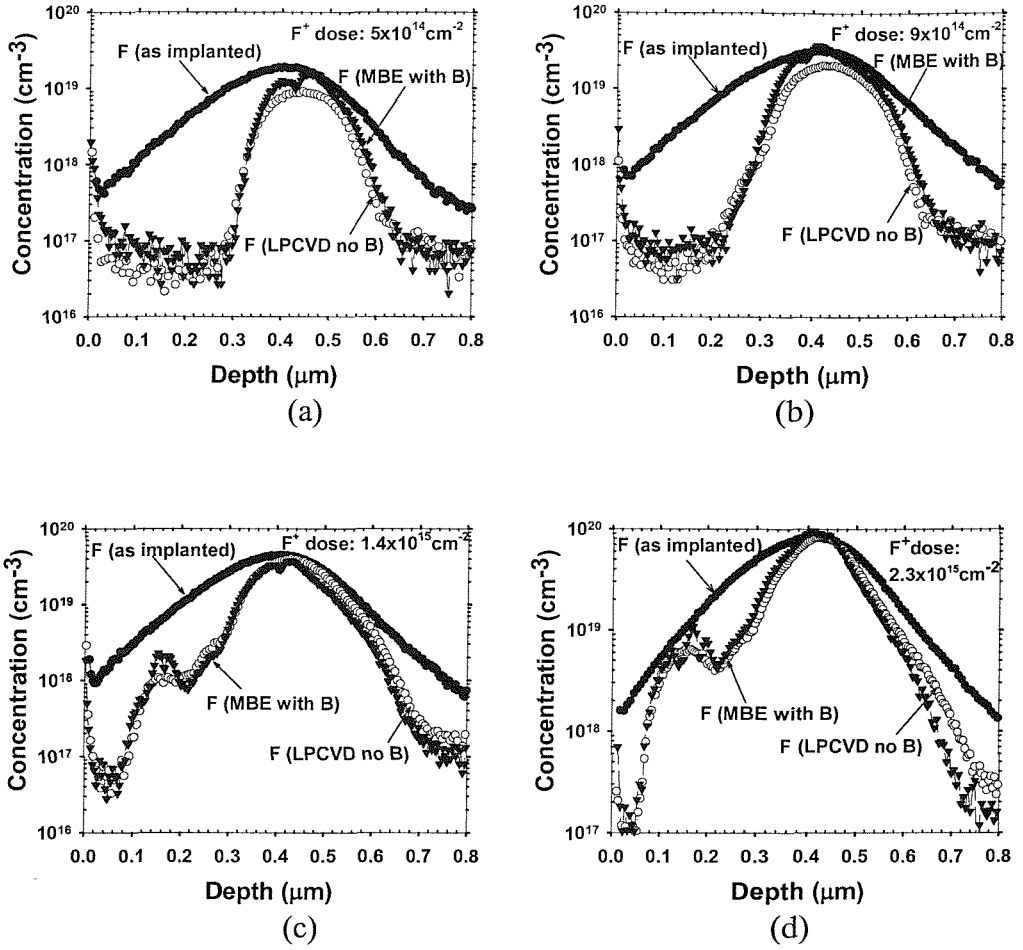

Figure 5.12: Fluorine SIMS profiles before and after an anneal of 30s at 1000°C in nitrogen for samples with and without a boron marker layer. The samples with the boron marker layer were grown using MBE whereas the samples without the boron marker layer were grown using LPCVD. Results are shown for fluorine implantation doses of (a) $5\times10^{14}cm^{-2}$, (b) $9\times10^{14}cm^{-2}$, (c) $1.4\times10^{15}cm^{-2}$ and (d) $2.3\times10^{15}cm^{-2}$.

F implant dose (cm^{-2})		Fluorine remaining after anneal							
Implant	SIMS	Total		Shallow peak (0.07-0.22μm)		Shoulder (0.22-0.28μm)		Deep peak (0.28-0.70μm)	
		(cm^{-2})	%	(cm^{-2})	%	(cm^{-2})	%	(cm^{-2})	%
5×10^{14}	5×10^{14}	2.2×10^{14}	44	1.1×10^{12}	0.5	3.5×10^{11}	0.2	2.1×10^{14}	95
9×10^{14}	8.8×10^{14}	5.6×10^{14}	63	1.3×10^{12}	0.2	2.0×10^{12}	0.4	5.5×10^{14}	98
1.4×10^{15}	1.2×10^{15}	6.1×10^{14}	51	1.5×10^{13}	2.5	1.1×10^{13}	1.8	5.8×10^{14}	95
2.3×10^{15}	2.3×10^{15}	1.6×10^{15}	70	8.3×10^{13}	5.2	4.6×10^{13}	2.9	1.5×10^{15}	94

Table 5.2: A summary of integrated fluorine doses in different regions of the profiles before and after an anneal of 30s at 1000°C in nitrogen for fluorine implantation doses of $5\times10^{14}cm^{-2}$ to $2.3\times10^{15}cm^{-2}$.

Figure 5.13 shows a graph of the peak fluorine concentration in the fluorine peaks and shoulders as a function of F^+ implantation dose. Results are shown for samples with and without the boron marker layer. For the shallow fluorine peak in the samples without the boron marker layer, the peak fluorine concentration rises from the SIMS background level to a value of around $1\times10^{18}cm^{-3}$ at a F^+ implantation dose of $1.4\times10^{15}cm^{-2}$ and then rises further as the F^+ dose is increased to $2.3\times10^{15}cm^{-2}$. A similar trend is seen in the samples with the boron marker layer, though the values of peak fluorine concentration are higher after the rise from the SIMS background level. Consideration of the SIMS profiles in figures 5.12(c) and (d) shows that these higher fluorine concentrations are due to the presence of the ripples on the shallow fluorine peak. For the fluorine shoulder in the samples with and without the boron marker layer, the peak fluorine concentration rises from the SIMS background level to a value of around $1\times10^{18}cm^{-3}$ at a F^+ dose of $9\times10^{14}cm^{-2}$, and then increases further as the F^+ dose is increased to $2.3\times10^{15}cm^{-2}$. Thus, the trend for the fluorine shoulder is similar to that for the shallow fluorine peak, with the difference that the rise in peak fluorine

concentration from the SIMS background level occurs at a lower fluorine dose. For the deep fluorine peak, a high concentration of fluorine is present for all F^+ doses and this value rises with increasing F^+ dose. A similar trend is seen in samples with and without the boron marker layer, though the values of fluorine concentration are slightly higher in the former samples, particularly at the two lowest F^+ doses.

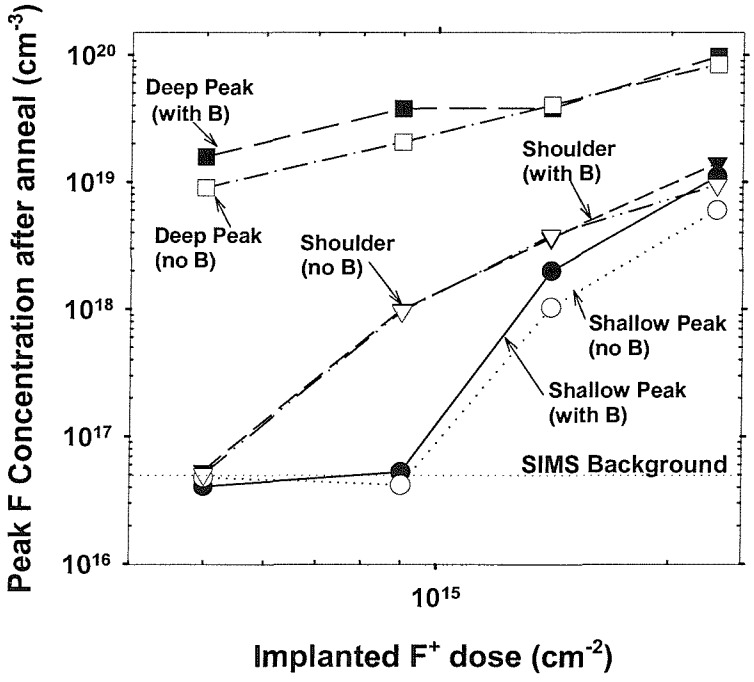

Figure 5.13: Fluorine concentrations at depths corresponding to the positions of the shallow fluorine peak, the fluorine shoulder and the deep fluorine peak as a function of F^+ implantation dose. Results are shown for samples with and without the boron marker layer.

5.4 Discussion

The results in figures 5.2 and 5.3 show that the high energy F^+ implant has not only completely eliminated boron transient enhanced diffusion, but has also given a substantial reduction in the thermal diffusion of boron. This corresponds to a reduction factor of 3.9 in boron thermal diffusion coefficient in silicon. Reductions in

the transient enhanced diffusion of boron in silicon by fluorine have been reported previously in the literature [1-19], however our results show complete suppression of transient enhanced diffusion and reduction in thermal diffusion, which have not been reported before in the literature.

The results in figure 5.9 clearly show that no reduction of boron thermal diffusion is seen at F^+ doses of 5×10^{14} and $9\times10^{14}cm^{-2}$, whereas significant reduction is seen at a F^+ dose of $1.4\times10^{15}cm^{-2}$. Furthermore, the results in figure 5.11 show that a shallow fluorine peak is present in the vicinity of the boron marker layer for a F^+ dose of $1.4\times10^{15}cm^{-2}$, but is not present for lower doses. Thus there is a correlation between the appearance of the shallow fluorine peak in the vicinity of the boron marker layer and the reduction of boron thermal diffusion. This reduction of boron thermal diffusion occurs above a critical F^+ dose between 9×10^{14} and $1.4\times10^{15}cm^{-2}$.

The shallow fluorine peak in figure 5.11(c) lies at a depth of about 0.07-0.22μm, which corresponds to 0.17-0.53R_p, where R_p is the range of the fluorine implant. Simulations of vacancy and interstitial profiles after implantation [23, 24] have predicted a vacancy-rich region extending from the surface to a depth approaching the implantation range, R_p, and a deeper interstitial-rich region peaking at a depth just beyond R_p. This indicates that the shallow fluorine peak lies in the vacancy-rich region of the damage profile. Work on the diffusion of fluorine in silicon [25] has shown that fluorine diffuses extremely rapidly in silicon, with significant diffusion occurring at temperatures as low as 550°C [25]. Thus we would not expect to see much fluorine remaining after the 30s anneal at 1000°C used in our work. The presence of large fluorine peaks in figure 5.11 after anneal therefore suggests that fluorine has been trapped at defects created by the fluorine implant. The TEM micrograph in figure 5.7 shows no evidence of extended defects down to a depth of

0.29μm, and hence the trapping of fluorine at the shallow fluorine peak must be due to defects that are too small to resolve by TEM.

There is considerable evidence in the literature for the formation of vacancy-fluorine clusters [13, 17, 26-28] that are too small to resolve by TEM. For example, Shano *et al.* [13] proposed the presence of $F\text{-}V_6$ clusters on the basis of ab-initio calculations and Diebel *et al.* [17, 28] proposed the presence of $F\text{-}V_3$ clusters. Positron annihilation spectroscopy has also been used to directly show the presence of fluorine vacancy complexes close to the surface [26]. Our results are consistent with this work, and hence we propose that the shallow fluorine peak is due to the trapping of fluorine at vacancy-fluorine clusters. The results in figure 5.13 show that a fluorine concentration after anneal of $\approx 1\times10^{18}cm^{-3}$ is needed for the fluorine vacancy clusters to form and for boron thermal diffusion to be reduced. This value is in agreement with the results of Shano *et al.* [13], who showed that a minimum fluorine concentration of $1\times10^{18}cm^{-3}$ was required after anneal to suppress boron transient enhanced diffusion.

A comparison of the SIMS profiles in figures 5.4 and 5.5 with the TEM micrographs in figure 5.7 (a) and (b) respectively, shows that the deep fluorine peak correlates with the band of dislocation loops. The deep fluorine peak extends from about 0.28μm to 0.70μm, which compares with the band of defects in figure 5.7 extending from about 0.29μm to 0.73μm. As the fluorine implant did not amorphise the layer (see figure 6.14 in chapter 6), these are typical dislocation loops resulting from a sub amorphising implant [29]. Similar dislocation loops have been reported by Wu *et al.* [30] for a 49keV, $2\times10^{15}cm^{-2}$ BF_2^+ implant after anneal at 900°C for 30 minutes. The loops were reported to be perfect and faulted partial interstitial loops, with sizes ranging from ≈ 20-80nm [30]. Given the similarity between these reported loops and those in figure 5.7, and the location of the deep fluorine peak in the

interstitial-rich region of the fluorine damage profile, we suggest that the deep fluorine peak is due to fluorine trapping at interstitial type dislocation loops.

Several alternative mechanisms have been proposed to explain the effect of fluorine in suppressing the transient enhanced diffusion of boron in silicon, including a chemical interaction between boron and fluorine [4, 9, 11, 14, 16], the presence of vacancy-fluorine clusters [13, 17, 28] and the interaction of fluorine with interstitials [12,4-10)].

The possibility of a chemical interaction between boron and fluorine can be discounted, since the shallow fluorine peak is seen whether or not a boron marker layer is present, as shown in figure 5.12 (c) and (d), indicating that the shallow fluorine peak is not caused by the presence of the boron marker layer. Figure 5.12 also shows that the deep fluorine peak is present at all F^+ doses, while figures 5.9 and 5.3 show that suppression of boron thermal diffusion is only seen for the two highest F^+ doses of $1.4\times10^{15}cm^{-2}$ and $2.3\times10^{15}cm^{-2}$ respectively. Trapping of interstitials at dislocation loops in the deep fluorine peak can therefore also be discounted as an explanation for the effect of fluorine on boron thermal diffusion. The strong correlation between the suppression of boron thermal diffusion and the appearance of the shallow fluorine peak in the vicinity of the boron marker layer at a fluorine implantation dose of $1.4\times10^{15}cm^{-2}$ provides clear evidence that this peak is responsible for the suppression of boron thermal diffusion. The presence of vacancy-fluorine clusters in the vicinity of the boron marker layer would be expected to give an under-saturation of the local interstitial concentration, since any interstitials in the vicinity would be able to recombine and annihilate with vacancies at or near the vacancy-fluorine clusters. Since boron diffusion in silicon is mediated by interstitials,

an under-saturation of the interstitial concentration would give rise to a suppression of the boron thermal diffusion.

A comparison of the shapes of the shallow fluorine peaks in figures 5.12 (c) and (d) shows not only an increase in peak fluorine concentration with F^+ implantation dose, but also a broadening of the peak. Taking a fluorine concentration after anneal of $1\times10^{18}cm^{-3}$ as a reference (the concentration required for the shallow peak formation), the shallow fluorine peak extends to within 0.15μm of the surface for a F^+ dose of $1.4\times10^{15}cm^{-2}$ and within 0.07μm for a dose of $2.3\times10^{15}cm^{-2}$, as shown in table 5.4. Thus the shallow fluorine peak extends closer to the surface at the higher F^+ dose. This behaviour can be understood if critical fluorine and vacancy concentrations after implant are required for the vacancy-fluorine clusters to form. The as-implanted fluorine profiles in figures 5.12 (c) and (d) show a rising fluorine concentration with increasing depth in the vicinity of the shallow fluorine peak. In contrast, simulations of vacancy profiles after implant [23] indicate that the vacancy concentration decreases with increasing depth, which is the opposite trend to the fluorine concentration. In the surface region where the shallow fluorine peak is located, the fluorine concentration is low but the vacancy concentration is high, so the fluorine concentration would be expected to limit the vacancy-fluorine cluster formation. This can explain why the shallow fluorine peak extends towards the surface with increasing F^+ dose, since the depth at which the fluorine concentration after implant reaches the critical value required for cluster formation (value estimated below) lies closer to the surface at higher fluorine doses.

The critical fluorine concentration after implant required for vacancy-fluorine cluster formation can be estimated either from the point on the shallow fluorine peak at which the fluorine concentration drops below $1\times10^{18}cm^{-3}$ or from the as-implanted

fluorine concentration in the vicinity of the shallow fluorine peak at the critical F^+ implant dose. Values of critical fluorine concentration after implant are summarised in table 5.4 for the first method and in table 5.3 for the second method. Table 5.3 shows a critical fluorine concentration after implant of $5.6\times10^{18}cm^{-3}$ for a F^+ dose of $1.4\times10^{15}cm^{-2}$, and of $3.6\times10^{18}cm^{-3}$ for a F^+ dose of $2.3\times10^{15}cm^{-2}$. For comparison, table 5.4 shows that the shallow fluorine peak appears at a critical F^+ implant dose between 9×10^{14} and $1.4\times10^{15}cm^{-2}$, which gives a critical fluorine concentration after implant between 4.0 and $6.6\times10^{18}cm^{-3}$. These values in table 5.4 are of the same order as those in table 5.3, which gives some confidence in their validity. From this data it can therefore be concluded that the critical fluorine concentration after implant for the formation of the vacancy-fluorine clusters in the shallow fluorine peak is in the range $3.6\text{-}6.6\times10^{18}cm^{-3}$.

Finally, it is interesting to speculate on the origin of the fluorine shoulder, which is present at a depth of 0.22-0.28μm. This is equivalent to a depth of $0.52\text{-}0.67R_p$, which indicates that the shoulder is in the vacancy-rich region of the damage profile. The TEM results in figure 5.7 show that there are no dislocation loops at this depth, and hence the shoulder is not due to trapping of fluorine at dislocation loops. Furthermore, the results in figure 5.13 show that the variation of peak fluorine concentration in the shoulder with implanted fluorine dose follows a similar trend to that seen in the shallow fluorine peak, though with the critical fluorine dose shifted to a lower value. These considerations point to the conclusion that the shoulder is due to some kind of vacancy-fluorine cluster. Following the two approaches described above for estimating the critical F^+ dose after implant, table 5.4 gives a value of $1.5\times10^{19}cm^{-3}$ at a F^+ dose of $9\times10^{14}cm^{-2}$ and $1.5\times10^{19}cm^{-3}$ at a F^+ dose of $1.4\times10^{15}cm^{-2}$, while table 5.3 gives a value in the range $1.0\text{-}1.7\times10^{19}cm^{-3}$. These two approaches are again

giving values of the same order, and all fall within a range of 1.0-1.7×$10^{19}$$cm^{-3}$. This range is different than that obtained for the shallow fluorine peak (3.6-6.6×$10^{18}$$cm^{-3}$), which suggests that the fluorine shoulder may be due to a different type of vacancy-fluorine cluster than the shallow fluorine peak. Since the shoulder is in a region where the fluorine concentration is high and the vacancy concentration is low [23] after implant, we speculate that the clusters in this region may be fluorine-rich. Similarly, since the shallow fluorine peak is in a region where the fluorine concentration is low and the vacancy concentration high [23] after implant, we speculate that the clusters in this region may be vacancy-rich. Support for this hypothesis comes from reports in the literature which showed that for a 0.5MeV, 5×$10^{15}$$cm^{-2}$ F^+ implant, V-dominated V-F complexes were formed closer to the surface and, F-dominated V-F complexes were formed deeper closer to the implantation range [26]. Further work is needed to confirm this hypothesis.

F implant dose (cm^{-2})	**Shallow F peak**		**F shoulder**	
	F conc^n after implant at depth of 0.16um (cm^{-3})	**Shallow peak present?**	**F conc^n after implant at depth of 0.29um** (cm^{-3})	**Shoulder present?**
5×10^{14}	2.5×10^{18}	✗	1.0×10^{19}	✗
9×10^{14}	4.0×10^{18}	✗	1.7×10^{19}	✔
1.4×10^{15}	6.6×10^{18}	✔	2.5×10^{19}	✔
2.3×10^{15}	11×10^{18}	✔	4.6×10^{19}	✔

Table 5.3: Estimation of the fluorine concentration after implant required for the formation of the shallow fluorine peak and the fluorine shoulder obtained from analysis of the peak fluorine concentrations in the shallow fluorine peak and fluorine shoulder at different F^+ implant doses.

F implant dose (cm^{-2})	Shallow F peak		F shoulder	
	Depth at which F concentration after anneal is 1×10^{18} cm^{-3} (μm)	F concentration after implant (cm^{-3})	Depth at which F concentration after anneal is 1×10^{18} cm^{-3} μm	F concentration after implant (cm^{-3})
9×10^{14}	-	-	0.28	1.5×10^{19}
1.4×10^{15}	0.15	5.6×10^{18}	0.23	1.5×10^{19}
2.3×10^{15}	0.07	3.6×10^{18}	-	-

Table 5.4: Estimation of the fluorine concentration after implant required for the formation of the shallow fluorine peak and the fluorine shoulder obtained from an analysis of the depths at which the fluorine concentration after anneal drops below the critical value of $1\times10^{18}cm^{-3}$

5.5 Conclusions

In conclusion, a study has been made of the effect of a high energy F^+ implant with doses in the range of $5\times10^{14}cm^{-2}$ to $2.3\times10^{15}cm^{-2}$ on the diffusion of boron from a shallow marker layer grown by molecular beam epitaxy and annealed for 30s at 1000°C in nitrogen. In samples implanted with P^+ and F^+, the fluorine ($2.3\times10^{15}cm^{-2}$) completely suppresses boron transient enhanced diffusion. For F^+ doses of $5\times10^{14}cm^{-2}$ and $9\times10^{14}cm^{-2}$ the fluorine implant does not reduce the boron thermal diffusion, whereas for F^+ doses of $1.4\times10^{15}cm^{-2}$ and $2.3\times10^{15}cm^{-2}$ the fluorine reduces the boron thermal diffusion coefficient by factors of 1.9 and 3.7 respectively. This reduction of boron thermal diffusion correlates with the appearance of a shallow fluorine peak (depth = 0.07-0.22μm) in the SIMS profile at the same F^+ dose of $1.4\times10^{15}cm^{-2}$. This peak is present in samples with and without the boron marker layer and hence is not due to a chemical interaction between the fluorine and boron. Cross-sectional TEM

micrographs show that there are no extended defects at the depth of the shallow fluorine peak, which indicates that it is due to trapping of fluorine at defects too small to resolve by TEM. The shallow fluorine peak is located in the vacancy-rich region of the damage profile, which suggests that it is due to vacancy-fluorine clusters. Analysis of the SIMS profiles suggests that a fluorine concentration after implant in the range $3.6\text{-}6.6\times10^{18}cm^{-3}$ is needed for the vacancy-fluorine clusters to form. The reduction in boron diffusion resulting from a F^+ implant is explained by the presence of the vacancy-fluorine clusters, which suppress the excess interstitial concentration in the vicinity of the boron marker layer and hence reduce boron thermal diffusion.

References

1. R. G. Wilson, "Boron, fluorine and carrier profiles for B and BF_2 implants into crystalline and amorphous Si"; Journal of Applied Physics, vol. 54 (12), pp. 6879-6889, (1983).
2. K. Ohyu, T. Itoga and N. Natsuaki, "Advantages of fluorine introduction in boron implanted shallow p+/n junction formation"; Japanese Journal of Applied Physics, vol. 29, pp. 457-462, (1990).
3. D. Fan, J. M. Parks and R. J. Jaccodine; "Effect of fluorine on the diffusion of through-oxide implanted boron in silicon"; Applied Physics Letters, vol. 59 (10), pp. 1212-1214, (1991).
4. L. Y. Krasnobaev, N. M. Omelyanovskaya, V. V. Makarov, "The effect of fluorine on the redistribution of boron in ion implanted silicon"; Journal of Applied Physics, vol. 74 (10), pp. 6020-6022, (1993).
5. T. H. Huang, H. Kinoshita, D. L. Kwong, "Influence of fluorine preamorphization on the diffusion and activation of low energy implanted boron during rapid thermal annealing"; Applied Physics Letters, vol. 65(14), pp. 1829-1831, (1994).
6. H. -H. Vuong, H. -J. Gossmann, C. S. Rafferty, H. S. Luftman, F. C. Unterwald, D. C. Jacobson, R. E. Ahrens, T. Boone, P. M. Zeitzoff, "Influence of fluorine implant on boron diffusion: determination of process modelling parameters"; Journal of Applied Physics; vol. 77 (7), pp. 3056-3060, (1995).

7. D. F. Downey, J. W. Chow, E. Ishida, K. S. Jones, "Effect of fluorine on the diffusion of boron in ion implanted silicon"; Applied Physics Letters, vol. 73 (9), pp. 1263-1265, (1998).
8. Y-J. Park and J–J. Kim, "Fluorine implantation effect on boron diffusion in Si"; Journal of Applied Physics; vol. 85 (2), pp. 803-806, (1999).
9. J. Liu, D. F. Downey, K. S. Jones and E. Ishida, "Fluorine effect on boron diffusion: chemical or damage?"; Proceedings International Conference Ion Implantation Technology, pp. 951-954, (1999).
10. E. Ishida, D. F. Downey, K. S. Jones and J. Liu, "The chemical effect of fluorine on boron transient enhanced diffusion"; Proceedings International Conference Ion Implantation Technology, vol. 2, pp. 909-912, (1999).
11. L. S. Robertson, P. N. Warnes, K. S. Jones, S. K. Earles, M. E. Law, D. F. Downey, S. Falk and J. Liu. "Junction depth reduction of ion implanted boron in silicon through fluorine ion implantation"; Materials Research Society Symposium Proceedings, vol. 610, pp. B4.2.1-B4.2.6, (2000).
12. N. Ohno, T. Hara, Y. Matsunaga, M. I. Current, M. Inoue, "Diffusion of ion implanted boron impurities into pre-amorphised silicon"; Materials Science in Semiconductor Processing; vol. 3, pp. 221-225, (2000).
13. T. S. Shano, R. Kim, T. Hirose, Y. Furuta, H. Tsuji, M. Furuhashi and K. Taniguchi, "Realization of ultra-shallow junction: suppressed boron diffusion and activation by optimised fluorine co-implantation"; Technical Digest of the International Electron Devices Meeting IEDM, pp. 37.4.1-37.4.4, (2001).

14. A. Mokhberi, R. Kasnavi, P. B. Griffin, J. D. Plummer, "Fluorine interaction with point defects, boron and arsenic in ion implanted Si"; Applied Physics Letters, vol. 80 (19), pp. 3530-3532, (2002).

15. J. M. Jacques, L. S. Robertson, K. S. Jones, J. Bennett and M. Rendon, "Effect of fluorine on the diffusion of boron in amorphous silicon"; Materials Research Society Symposium Proceedings, vol. 717, pp. C4.6.1-C4.6.6, (2002).

16. A. Dusch, J. Marcon, K. Masmoudi, K. Ketata, F. Olivie, M. Benzohra and M. Ketata, "Influence of fluorine on the simulation of the transient enhanced diffusion of 15keV BF_2^+ ion implantation into silicon"; Nuclear Instruments and Methods in Physics Research B, vol. 186, pp. 360-365, (2002).

17. M. Diebel, S. Chakravarthi, C. F. Machala, S. Ekbote, A. Jain and S. T. Dunham, "Investigation and modelling of fluorine co-implantation effects on dopant redistribution"; Materials Research Society Symposium Proceedings, vol. 765, pp. D6.15.1-D6.15.6, (2003).

18. K. Liu, J. Wu, J. Chen, A. Jain, "Fluorine assisted super-halo for sub-50nm transistors"; IEEE Electron Device Letters, vol. 24, pp. 180-182, (2003).

19. H. Fukutome, Y. Momiyama, H. Nakao, T. Aoyama, H. Arimoto, "Fluorine implantation impact in extension region on the electrical performance of sub-50nm PMOSFETS"; Technical Digest of the International Electron Devices Meeting, pp. 20.2.1-20.2.4, (2003).

20. B. Martinet, H. Baudry, O. Kermarree, Y. Campidelli, M. Laurens, M. Marty, T. Schwartzmann, A. Monroy, D. Bensahel and A. Chantre, "100GHz SiGe:C HBTs using non selective base epitaxy"; Proceedings of the European Solid State Device Research Conference ESSDERC, pp. 97-100, (2001).

21. D. J. Eaglesham, P. A. Stolk, H. -J. Gossmann and J. M. Poate, "Implantation and transient B diffusion in Si: the source of the interstitials", Applied Physics Letters, vol. 65 (18), pp. 2305-2307, (1994).

22. J. Lee, S. Yoon, Y. Kim, T. Won, J. Kim and D. Lee, "Three-dimensional modelling of the TED due to implantation damage"; Simulation of Semiconductor Processes and Devices SISPAD'97, pp. 301-303, (1997).

23. M. D. Giles, "Transient phosphorus diffusion below the amorphization threshold"; Journal of the Electrochemical Society, vol. 138, pp.1160-1165, (1991).

24. A. Sultan, S. Banerjee, S. List, V. McNeil, "An approach using a subamorphizing threshold dose silicon implant of optimal energy to achieve shallower junctions"; Journal of Applied Physics, vol. 83 (12), pp. 8046-8050, (1998).

25. S.-P. Jeng, T. -P. Ma, R. Canteri, M. Anderle and G. W. Rubloff, "Anomalous diffusion of fluorine in silicon"; Applied Physics Letters, vol. 61 (11), pp. 1310-1312, (1992).

26. X. D. Pi, C. P. Burrows and P. G. Coleman, "Fluorine in silicon: diffusion, trapping and precipitation"; Physical Review Letters, vol. 90 (15), pp.155901-1-155901-4, (2003).

27. R. R. Robinson, M. E. Law, "Fluorine diffusion: models and experiments"; Technical Digest International Electron Devices Meeting, pp. 883-886, (2002).

28. M. Diebel and S. T. Dunham, "Ab-initio calculations to model anomalous fluorine behaviour"; Materials Research Society Symposium Proceedings, vol. 717, pp. C4.5.1-C4.5.6, (2002).

29. . K. S. Jones, S. Prussin and E. R. Weber, "A systematic Analysis of defects in ion implanted silicon"; Applied Physics A Solids and Surfaces, vol.45, pp. 1-34, (1988).

30. I-W. Wu, R. T. Fulks and J. C. Mikkelsen Jr, "Optimisation of BF_2 implanted and rapidly annealed junctions in silicon"; Journal of Applied Physics, vol. 60 (7), pp. 2422-2438, (1986).

Chapter 6

The Effect of Fluorine Implantation Dose on Boron Transient Enhanced Diffusion and Boron Thermal Diffusion in $Si_{1-x}Ge_x$

6.1 Introduction

While there has been considerable research on the effect of fluorine on boron transient enhanced diffusion in silicon [1-8], to our knowledge there have been no reports on the effects of fluorine on transient enhanced and thermal diffusion of boron in silicon germanium. In this chapter, a study is made of the effect of fluorine implantation dose on boron transient enhanced diffusion and thermal diffusion in silicon germanium. Samples with and without a P^+ implant are studied so that the effect of fluorine on both boron transient enhanced diffusion (TED), caused by the excess interstitials generated by the P^+ implant [9], and thermal diffusion can be separately characterised. It is shown that boron transient enhanced diffusion is suppressed for all fluorine doses studied and that the suppression of boron TED is directly related to a broad deep fluorine peak coinciding with the implant range. It is also shown that a critical fluorine dose exists, above which the fluorine suppresses boron thermal diffusion and below which it has no effect on the boron thermal diffusion. This critical fluorine dose is lower than that seen in silicon (chapter 5) and

correlates with a sharp and high fluorine peak in the silicon germanium layer in comparison with a wider and lower fluorine peak in silicon.

6.2 Experimental Procedure

Boron doped silicon germanium marker layers and a $Si_{1-x}Ge_x$ multi layer were grown by low pressure chemical vapour deposition on (100) silicon wafers. The growth details of each of the three layers used are summarised in table 6.1. Samples of the same epitaxial layer were cleaved into 1cm×1cm square bits and separated into four different groups, the first having no implants (unimplanted), the second having a phosphorus implant only (P^+ implanted), the third a phosphorus and a fluorine implant (P^+ & F^+ implanted) and the fourth a fluorine implant only (F^+ implanted). A 288keV, $6x10^{13}cm^{-2}$ P^+ implant was used and was chosen to be similar to those used for a selective implanted collector in a bipolar process [9]. A 185KeV F^+ implant was used and the energy was selected such that the fluorine range was the same as that of the phosphorus implant. The fluorine implantation dose was varied from $5x10^{14}cm^{-2}$ to $1x10^{16}cm^{-2}$ in the fluorine implanted samples. The phosphorus and fluorine implantations were carried out at the EPSRC Ion Implantation Centre at Surrey University. After ion implantation the samples were cleaned by a 10 minutes dip in fuming nitric acid followed by rinsing with DI water and blow drying using a nitrogen gun. The samples were then arranged side by side on the platen of an AG rapid thermal annealing RTA system using dummy bits in order to complete a 4 inch wafer area, such that there were no free edges in order to reduce heat loss, and annealed in nitrogen at 1000°C for 30s. Boron (B11), germanium (Ge 74) and fluorine (F19) concentration depth profiles were obtained on all samples by Secondary Ion Mass Spectroscopy (SIMS) at Loughborough Surface Analysis Ltd. SIMS was performed

using O_2^+ primary ion bombardment and positive secondary ion detection. The SIMS analysis method is the same as that described in chapter 5. The layers were also analysed by Transmission Electron Microscopy (TEM). The TEM micrographs were taken by Dr. Yun Wang at Surrey University. The annealed boron profiles were aligned to the as-grown boron profile and the boron doses were normalised to the as-grown boron profile dose. This reduces errors in dose and depth scaling arising from SIMS analysis. The annealed boron profiles were then fitted using the Silvaco Athena Optimizer. This was done by importing the as-grown and annealed boron SIMS profiles in the $Si_{1-x}Ge_x$ layer into a silicon layer defined in the ATHENA input file (as shown in Appendix A). The intrinsic boron diffusion coefficient (Dix.0 Athena parameter) was then optimised with all other factors turned off (as shown in Appendix B), using the fully coupled diffusion model, until a good fit was obtained between the fitted and measured SIMS boron profiles.

Sample	**Growth Temperature (°C)**	**Ge content (%)**	**Ge width (nm)**	**B peak concentration (cm^{-3})**
A (2Si962)	800	11	39	$1.2x10^{19}$
B (5-351)	850	6	49	$5.1x10^{18}$
C (5-355)	850	10 6 3	52 44 52	NONE

Table 6.1: A summary of the growth details of the $Si_{1-x}Ge_x$ epitaxial layers used.

6.3 Results

Figure 6.1 shows boron SIMS profiles in samples (from growth B see table 6.1) implanted with fluorine doses of $5\times10^{14}cm^{-2}$ (figure 6.1(a)), $7\times10^{14}cm^{-2}$ (figure 6.1(b)), $9\times10^{14}cm^{-2}$ (figure 6.1(c)), and $1.4\times10^{15}cm^{-2}$ (figure 6.1(d)) and annealed at 1000°C. Profiles are presented for P^+ & F^+ implanted, P^+ implanted, F^+ implanted and unimplanted samples. The as-grown boron and germanium profiles are also included for reference. For the sample implanted with P^+ only, the anneal decreases the peak boron concentration in the $Si_{1-x}Ge_x$ layer significantly from 5.1×10^{18} to $1.5\times10^{18}cm^{-3}$ and gives considerable out-diffusion of the boron profile into the adjacent silicon layers. In contrast for the unimplanted sample, the decrease in peak boron concentration in the $Si_{1-x}Ge_x$ layer is smaller (from 5.1×10^{18} to $2.3\times10^{18}cm^{-3}$) and the boron out-diffusion into the silicon is significantly less. Comparing the widths of the boron profiles at a concentration of $3\times10^{17}cm^{-3}$, we obtain widths of 160nm and 114nm for the P^+ implanted and unimplanted samples respectively. These results indicate that the phosphorus implant is giving rise to considerable transient enhanced diffusion of boron. The SIMS profile in figure 6.1(a) for the P^+ & F^+ implanted sample indicates that the amount of boron diffusion is dramatically less than that in the sample implanted with P^+ only and is comparable with the amount of boron diffusion in the unimplanted sample. Comparing the widths of the boron profiles at a concentration of $3\times10^{17}cm^{-3}$, we obtain values of 160nm, 116nm and 114nm for P^+ implanted, P^+ & F^+ implanted and unimplanted samples respectively. This indicates that the $5\times10^{14}cm^{-2}$ F^+ implant has completely suppressed boron transient enhanced diffusion resulting from the phosphorus implant. Similar results are seen in figure 6.1(b) for a F^+ implant of $7\times10^{14}cm^{-2}$, as can be seen from the values of boron profile

widths in table 6.2. The boron profile of the F^+ implanted sample is almost identical to that of the unimplanted sample in both figures 6.1 (a) and (b) indicating that for the $5\times10^{14}cm^{-2}$ and $7\times10^{14}cm^{-2}$ F^+ doses the fluorine has no effect on the boron thermal diffusion.

Figure 6.1(c) shows boron SIMS profiles for a $9\times10^{14}cm^{-2}$ F^+ implanted sample and very different behaviour is observed. In this case, the amount of boron diffusion in the P^+ & F^+ implanted sample is not only dramatically less than that in the sample implanted with P^+ only, but also significantly less than that in the unimplanted sample. Comparing the boron profile widths at a concentration of $3\times10^{17}cm^{-3}$, we obtain values of 160nm, 87nm and 114nm for P^+ implanted, P^+ & F^+ implanted and unimplanted samples respectively. Furthermore, the amount of boron diffusion in the P^+ & F^+ implanted sample is similar to that in the F^+ implanted sample (boron profile width of 87nm compared with 93nm) (as shown in table 6.2). These results indicate that a $9\times10^{14}cm^{-2}$ F^+ implant not only suppresses boron transient enhanced diffusion but also significantly decreases boron thermal diffusion. Similar behaviour is seen for a F^+ dose of $1.4\times10^{15}cm^{-2}$, as shown in figure 6.1(d). In this case, the widths of the boron profiles are 87nm and 93nm in the P^+ & F^+ implanted and F^+ implanted samples respectively, compared with 160nm and 114nm in the P^+ implanted and unimplanted samples respectively (as shown in table 6.2).

Figure 6.2 shows the effect of a F^+ implant on boron diffusion for higher F^+ implantation doses of $2.3\times10^{15}cm^{-2}$ (figure 6.2(a)) and $1\times10^{16}cm^{-2}$ (figure 6.2(b)). The profiles were measured on samples taken from growth A (see table 6.1) and the as-grown boron and germanium profiles are included for comparison. These samples show a similar trend to that seen in figure 6.1(d), namely these high dose F^+ implants not only suppress boron transient enhanced diffusion resulting from the P^+ implant but

also significantly decrease boron thermal diffusion. Values for the boron profile widths are summarised in table 6.2 for all the samples studied. The table shows an increased reduction in the boron profile widths as the F^+ implanted dose increases.

F^+ implant dose (cm^{-2})	**Width of boron profile for different sample types (nm)**			
	P^+ implanted	**unimplanted**	**P^+ & F^+ implanted**	**F^+ implanted**
5×10^{14}	160	114	116	116
7×10^{14}	160	114	107	114
9×10^{14}	160	114	100	100
1.4×10^{15}	160	114	90	90
2.3×10^{15}	136	127	77	77
1×10^{16}	136	127	81	81

Table 6.2: A summary of boron profile widths for samples implanted with 288keV, $6x10^{13}cm^{-2}$ phosphorus and various doses of fluorine and annealed in nitrogen for 30s at 1000°C.

Figure 6.3 shows a comparison of the fitted (FIT) and measured (SIMS) boron profiles in $Si_{1-x}Ge_x$ (growth B) of unimplanted (a), P^+ implanted (b) and P^+ & F^+ implanted (c-f) samples annealed at 1000°C for 30s in nitrogen. Results are shown for samples implanted with fluorine doses of $5\times10^{14}cm^{-2}$ (figure 6.3(c)), $7\times10^{14}cm^{-2}$ (figure 6.3(d)), $9\times10^{14}cm^{-2}$ (figure 6.3(e)), and $1.4\times10^{15}cm^{-2}$ (figure 6.3(f)). All the fitted profiles are in reasonable agreement with the measured SIMS profiles indicating reasonable fits. The extracted diffusion coefficient for the P^+ implanted sample (1.7×10^{-13} cm^2/s) is 3.2× greater than that of the unimplanted sample (5.2×10^{-14} cm^2/s) indicating transient enhanced diffusion caused by the P^+ implant as seen earlier in figure 6.1. The extracted diffusion coefficients of the P^+ & F^+ implanted samples (c-f)

are all much lower than that of the P^+ implanted sample (b), with reduction factors varying from 4 to 10.6 as shown in table 6.3, indicating suppression of transient enhanced diffusion for all fluorine doses.

Figure 6.4 shows a comparison of the fitted (FIT) and measured (SIMS) boron profiles in $Si_{1-x}Ge_x$ (growth B) of F^+ implanted samples annealed at 1000°C for 30s in nitrogen. Results are shown for samples implanted with fluorine doses of $5\times10^{14}cm^{-2}$ (figure 6.4(a)), $7\times10^{14}cm^{-2}$ (figure 6.4(b)), $9\times10^{14}cm^{-2}$ (figure 6.4(c)), and $1.4\times10^{15}cm^{-2}$ (figure 6.4(d)). All the fitted profiles are in reasonable agreement with the measured SIMS profiles indicating reasonable fits. The extracted diffusion coefficients of the $5\times10^{14}cm^{-2}$ (figure 6.4(a)) and $7\times10^{14}cm^{-2}$ (figure 6.4(b)) F^+ implanted samples (5.1×10^{-14} cm^2/s and 4.8×10^{-14} cm^2/s respectively) are very similar to that of the unimplanted sample (figure 6.3 (a)) (5.2×10^{-14} cm^2/s) as shown in table 6.4. The extracted diffusion coefficients of the $9\times10^{14}cm^{-2}$ (figure 6.4(c)) and $1.4\times10^{15}cm^{-2}$ (figure 6.4(d)) F^+ implanted samples (2.7×10^{-14} cm^2/s and 2.1×10^{-14} cm^2/s respectively) are very much lower than that of the unimplanted sample (figure 6.3 (a)) (5.2×10^{-14} cm^2/s). This indicates suppression of boron thermal diffusion by factors of 1.9 and 2.5 for fluorine doses of $9\times10^{14}cm^{-2}$ and $1.4\times10^{15}cm^{-2}$ respectively (as shown in table 6.4).

The extracted boron diffusion coefficients for the unimplanted samples (5.2×10^{-14} cm^2/s for growth B and 3×10^{-14} cm^2/s for growth A) agree with values in the literature for boron thermal diffusion in 10% Ge Si_{1-x} Ge_x at 1000°C; $2\times10^{-14}cm^2/s$ [10], $2\times10^{-14}cm^2/s$ [11] and $4\text{-}6\times10^{-14}cm^2/s$ [12].

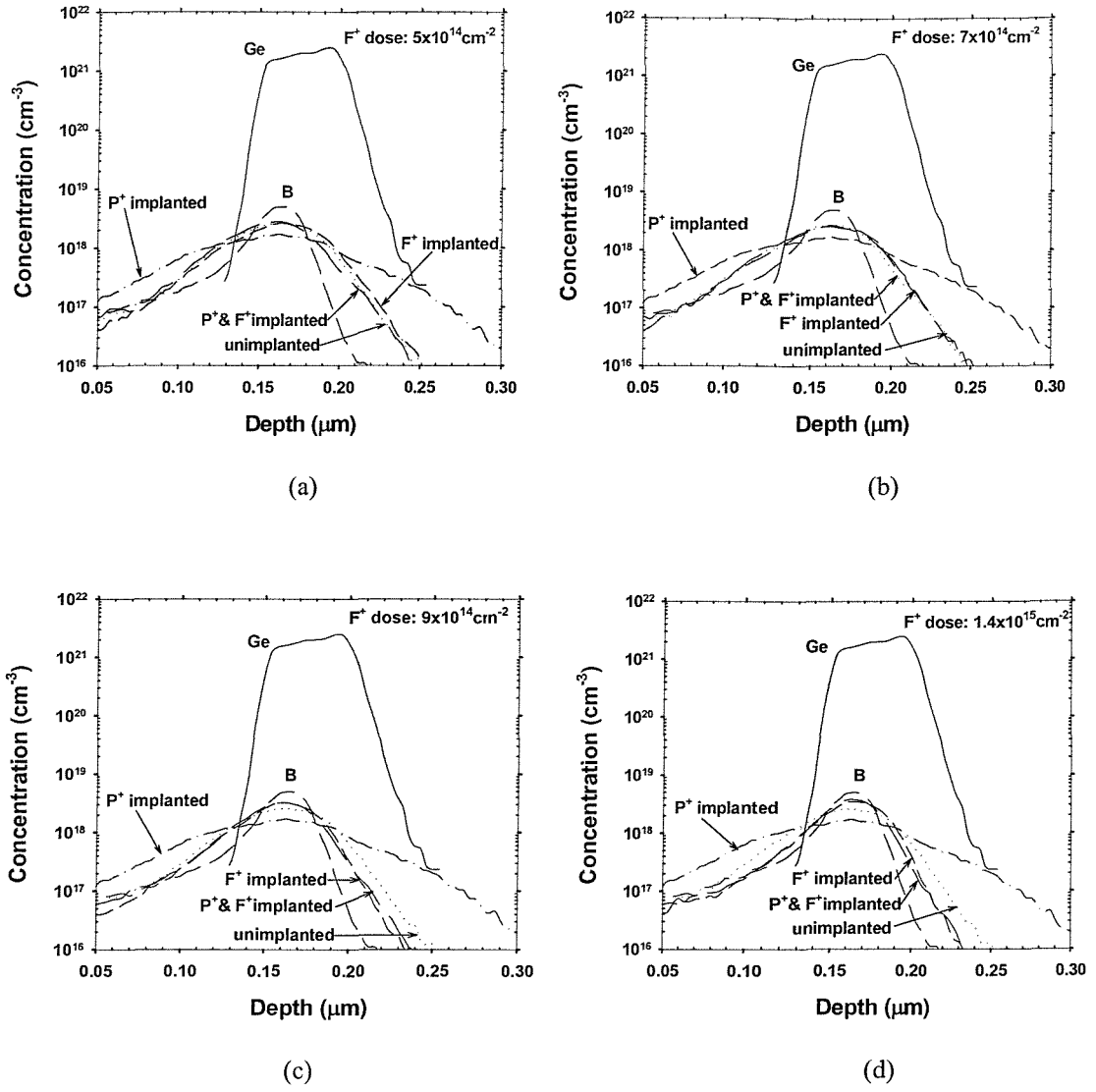

Figure 6.1: Boron SIMS profiles after an anneal at 1000°C for 30s in nitrogen for samples implanted with P^+ and F^+ (P^+ & F^+ implanted), P^+ only (P^+ implanted), F^+ only (F^+ implanted) and for samples with no implants (unimplanted). Results are shown for fluorine implantation doses of (a) $5\times10^{14}cm^{-2}$, (b) $7\times10^{14}cm^{-2}$, (c) $9\times10^{14}cm^{-2}$, and (d) $1.4\times10^{15}cm^{-2}$. As-grown boron and germanium profiles are also shown for reference. These samples are from growth B (see table 6.1).

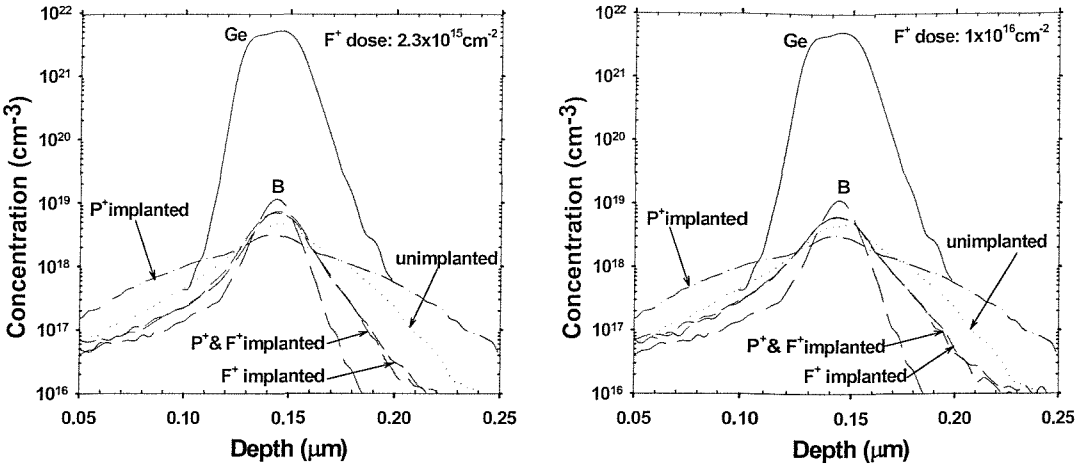

(a) (b)

Figure 6.2: Boron SIMS profiles after an anneal at 1000°C for 30s in nitrogen for samples implanted with P^+ and F^+ (P^+ & F^+ implanted), P^+ only (P^+ implanted), F^+ only (F^+ implanted) and for samples with no implants (unimplanted). Results are shown for fluorine implantation doses of (a) $2.3\times10^{14}cm^{-2}$, and (b) $1\times10^{16}cm^{-2}$. As-grown boron and germanium profiles are also shown for reference. These samples are from growth A (see table 6.1).

Figure 6.5 shows a comparison of the fitted and measured boron profiles in $Si_{1-x}Ge_x$ (growth A). Results are shown for unimplanted (figure 6.5 (a)) and P^+ implanted (figure 6.5 (b)) samples and for P^+ & F^+ implanted samples with fluorine doses of $2.3\times10^{15}cm^{-2}$ (figure 6.5 (c)) and $1\times10^{16}cm^{-2}$ (figure 6.5 (d)). Results are also shown for F^+ implanted samples with fluorine doses of $2.3\times10^{15}cm^{-2}$ (figure 6.5 (e)) and $1\times10^{16}cm^{-2}$ (figure 6.5 (f)). The fitted profiles show reasonable agreement with the measured SIMS profiles. The extracted diffusion coefficient for the P^+ implanted sample ($9.3\times10^{-14}cm^2/s$) is 3.1× greater than that of the unimplanted sample (3.0×10^{-14} cm^2/s) indicating transient enhanced diffusion caused by the P^+ implant as seen earlier in figure 6.2 and in agreement with the 3.2 factor obtained for samples from growth B

(see figure 6.3). The extracted diffusion coefficients for the P^+ & $2.3\times10^{15}cm^{-2}$ F^+ ($7.2\times10^{-15}cm^2/s$) and the P^+ & $1\times10^{16}cm^{-2}$ F^+ ($1.2\times10^{-14}cm^2/s$) implanted samples are 12.9 and 7.8 × less than that of the P^+ implanted sample ($9.3\times10^{-14}cm^2/s$) respectively (as shown in table 6.3), indicating suppression of boron transient enhanced diffusion. The extracted diffusion coefficients for the $2.3\times10^{15}cm^{-2}$ F^+ implanted sample ($8.5\times10^{-15}cm^2/s$) and the 1×10^{16} cm^{-2} F^+ implanted sample ($1.2\times10^{-14}cm^2/s$) are 3.5 and 2.5 × less than that of the unimplanted sample (3×10^{-14} cm^2/s) (as shown in table 6.4) indicating a large reduction of boron thermal diffusion in $Si_{1-x}Ge_x$.

Tables 6.3 and 6.4 show a summary of the extracted and normalised diffusion coefficients of the profiles shown in figures 6.3, 6.4 and 6.5 as well as the calculated reduction factors. Data shown in table 6.3 is for P^+ & F^+ implanted samples (growth A and B) with diffusion coefficients normalised to the diffusion coefficient of the P^+ implanted sample from the same growth. The data shown in table 6.4 is for F^+ implanted samples (growth A and B) with diffusion coefficients normalised to the diffusion coefficient of the unimplanted sample from the same growth. Values are given for a fluorine dose range of $5\times10^{14}cm^{-2}$ to $1\times10^{16}cm^{-2}$.We notice that the suppression of boron transient enhanced diffusion is seen for all doses, whilst the reduction in boron thermal diffusion is only seen at doses of $9\times10^{14}cm^{-2}$ and higher. The reduction in thermal diffusion increases with fluorine dose between doses of $9\times10^{14}cm^{-2}$ and $2.3\times10^{15}cm^{-2}$. This effect is illustrated clearly in figure 6.6, which shows a plot of the normalised diffusion coefficients versus fluorine implanted dose. The diffusion coefficients of the samples implanted with $1\times10^{16}cm^{-2}$ F^+ are slightly higher than those of the $2.3\times10^{15}cm^{-2}$ F^+ implanted samples. This result needs further verification. The diffusion coefficients of the P^+ & F^+ implanted samples are very similar to those of the F^+ implanted samples for all fluorine doses, indicating that both

transient enhanced diffusion suppression and boron thermal diffusion reduction is seen in those samples.

Figure 6.7 shows fluorine SIMS profiles before and after an anneal at 1000°C for samples (from growth B, see figure 6.1) implanted with F^+ only (right column) and with P^+ & F^+ (left column) at F^+ doses of $5\times10^{14}cm^{-2}$ (figures 6.7(a) and (b)), $7\times10^{14}cm^{-2}$ (figures 6.7(c) and (d)), $9\times10^{14}cm^{-2}$ (figures 6.7(e) and (f)) and $1.4\times10^{15}cm^{-2}$ (figures 6.7(g) and (h)). The corresponding annealed germanium and boron profiles are also shown for reference. For all F^+ doses the fluorine profiles of the F^+ implanted samples are almost identical to those of the P^+ & F^+ implanted samples, indicating that the P^+ implant had little effect on the fluorine profiles. For the two lowest fluorine implantation doses of $5\times10^{14}cm^{-2}$ (figures 6.7(a) and (b)) and $7\times10^{14}cm^{-2}$ (figures 6.7(c) and (d)), negligible fluorine is present (at the SIMS background level of $\approx1\times10^{17}cm^{-3}$) in the vicinity of the $Si_{1-x}Ge_x$ layer after anneal. The majority of the fluorine is located in a broad peak; for a F^+ dose of $5\times10^{14}cm^{-2}$, this broad peak is slightly deeper than the range of the fluorine implant, whereas for a F^+ dose of $7\times10^{14}cm^{-2}$, the peak is at a depth corresponding approximately with the range of the fluorine implant (0.41μm). For a fluorine dose of $9\times10^{14}cm^{-2}$ (figures 6.7(e) and (f)) two additional shallow peaks can be seen in the $Si_{1-x}Ge_x$ layer at depths of 0.16 and 0.19μm. These depths correspond with the positions of the top and bottom $Si_{1-x}Ge_x$/Si heterojunction interfaces. A small shoulder on the deep fluorine peak can also be seen between 0.22 and 0.28μm.

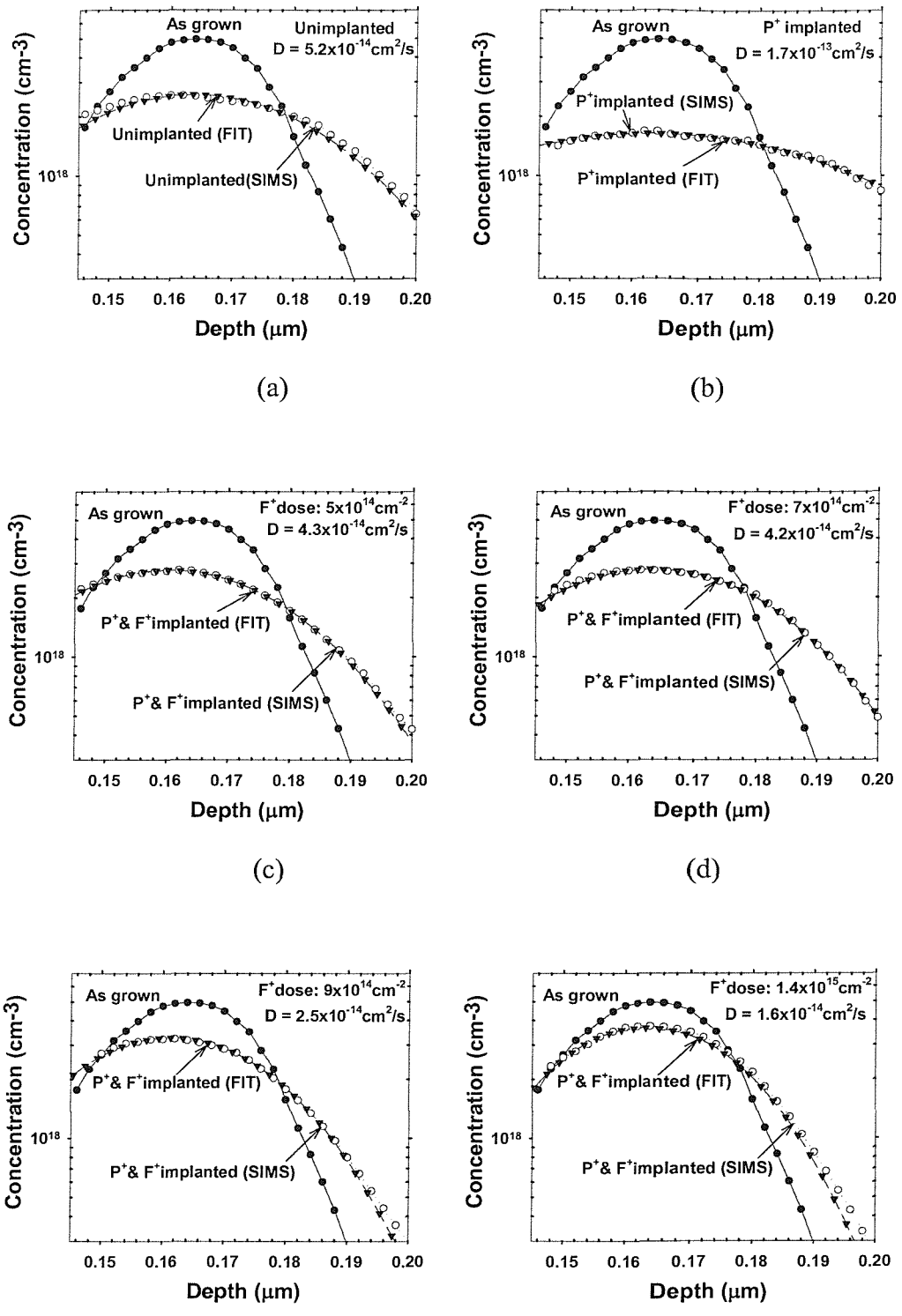

Figure 6.3: A comparison of fitted and measured boron profiles in $Si_{1-x}Ge_x$ (growth B) for unimplanted (a), P^+ implanted (b) and P^+ & F^+ implanted samples with fluorine doses of $5\times10^{14}cm^{-2}$ (c), $7\times10^{14}cm^{-2}$ (d), $9\times10^{14}cm^{-2}$ (e) and $1.4\times10^{15}cm^{-2}$ (f).

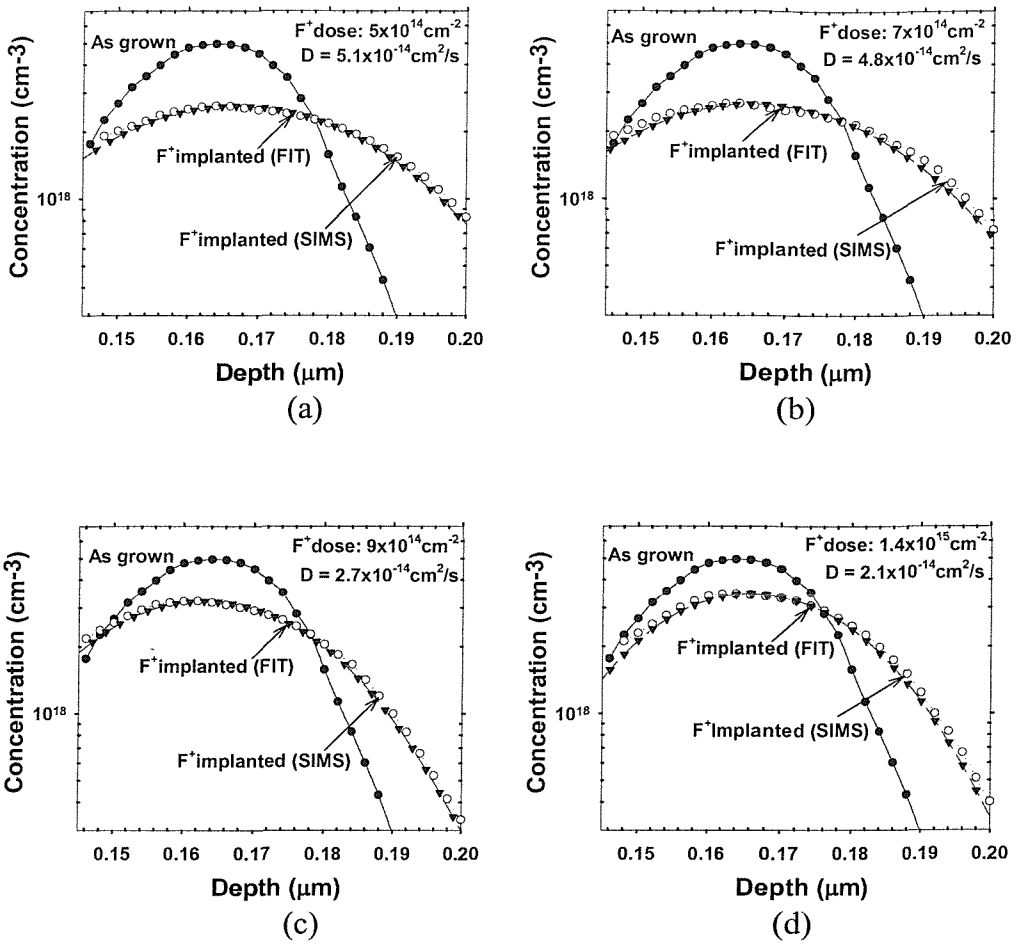

Figure 6.4: A comparison of fitted and measured boron profiles in $Si_{1-x}Ge_x$ (growth B) for F^+ implanted samples with fluorine doses of $5\times10^{14}cm^{-2}$ (a), $7\times10^{14}cm^{-2}$ (b), $9\times10^{14}cm^{-2}$ (c) and $1.4\times10^{15}cm^{-2}$ (d).

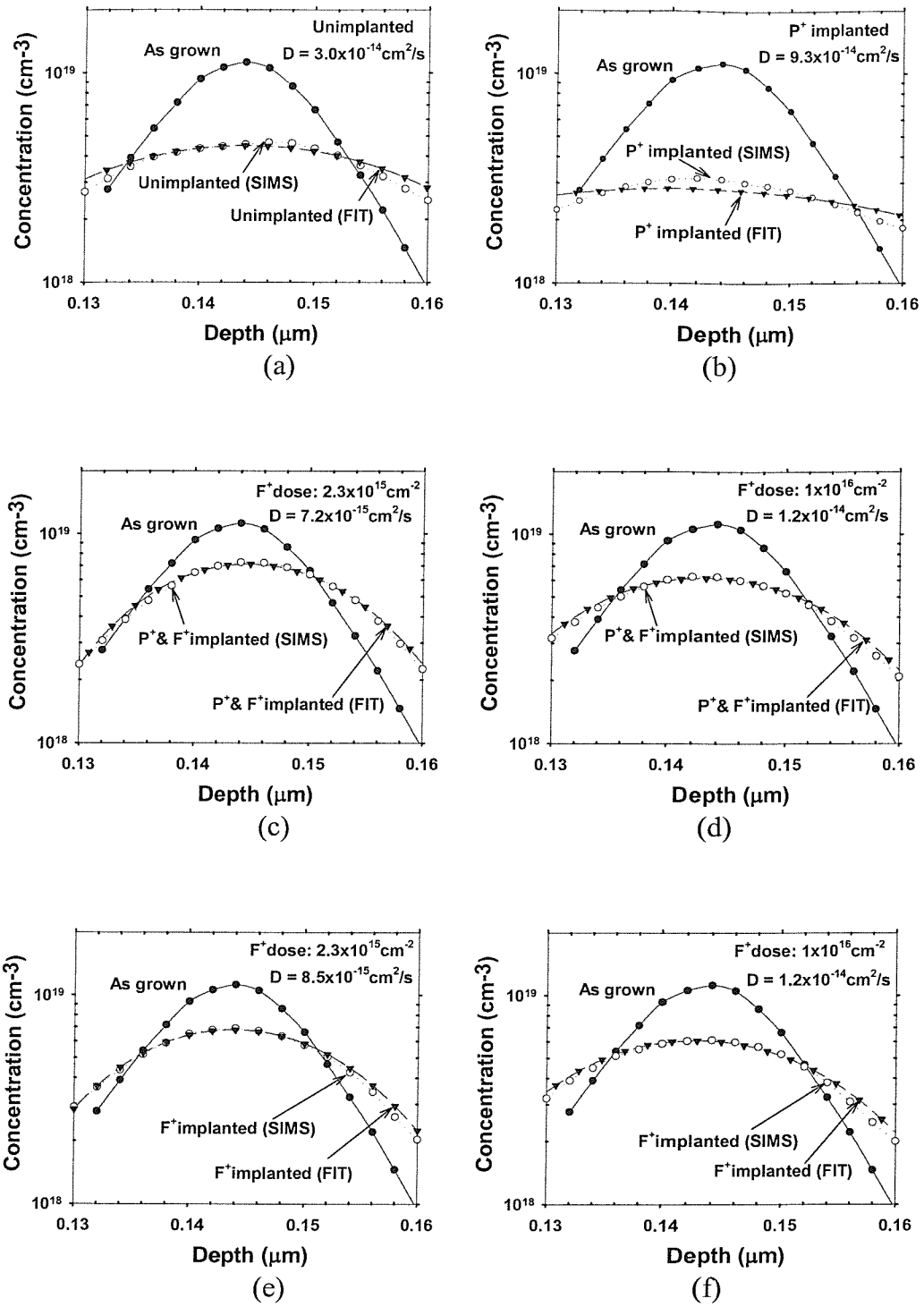

Figure 6.5: A comparison of fitted and measured boron profiles in $Si_{1-x}Ge_x$ (growth A) for unimplanted (a), P^+ implanted (b), P^+ & F^+ implanted samples with fluorine doses of $2.3\times10^{15}cm^{-2}$ (c) and $1\times10^{16}cm^{-2}$ (d) and F^+ implanted samples with fluorine doses of $2.3\times10^{15}cm^{-2}$ (e) and $1\times10^{16}cm^{-2}$ (f).

F^+ Implant Dose (cm^{-2})	Boron Diffusion Coefficient (cm^2/s)	Normalised Boron Diffusion Coefficient	Reduction Factor
NO F^+ implant (B)	1.7×10^{-13}	1	
5×10^{14}	4.3×10^{-14}	0.25	4
7×10^{14}	4.2×10^{-14}	0.25	4
9×10^{14}	2.5×10^{-14}	0.15	6.8
1.4×10^{15}	1.6×10^{-14}	0.09	10.6
NO F^+ implant (A)	9.3×10^{-14}	1	
2.3×10^{15}	7.2×10^{-15}	0.08	12.9
1×10^{16}	1.2×10^{-14}	0.13	7.8

Table 6.3: A summary of the extracted and normalised diffusion coefficients and the calculated reduction in diffusion coefficient factors of P^+ & F^+ implanted samples (growth A and B) with diffusion coefficients normalised to the diffusion coefficient of the P^+ implanted sample from the same growth. Values are given for a fluorine dose range of $5\times10^{14}cm^{-2}$ to $1\times10^{16}cm^{-2}$.

F^+ Implant Dose (cm^{-2})	Boron Diffusion Coefficient (cm^2/s)	Normalised Boron Diffusion Coefficient	Reduction Factor
Unimplanted (B)	5.2×10^{-14}	1	
5×10^{14}	5.1×10^{-14}	0.98	-
7×10^{14}	4.8×10^{-14}	0.92	-
9×10^{14}	2.7×10^{-14}	0.52	1.9
1.4×10^{15}	2.1×10^{-14}	0.4	2.5
Unimplanted (A)	3.0×10^{-14}	1	
2.3×10^{15}	8.5×10^{-15}	0.28	3.5
1×10^{16}	1.2×10^{-14}	0.4	2.5

Table 6.4: A summary of the extracted and normalised diffusion coefficients and the calculated reduction in diffusion coefficient factors of F^+ implanted samples (growth A and B) with diffusion coefficients normalised to the diffusion coefficient of the unimplanted sample from the same growth. Values are given for a fluorine dose range of $5\times10^{14}cm^{-2}$ to $1\times10^{16}cm^{-2}$.

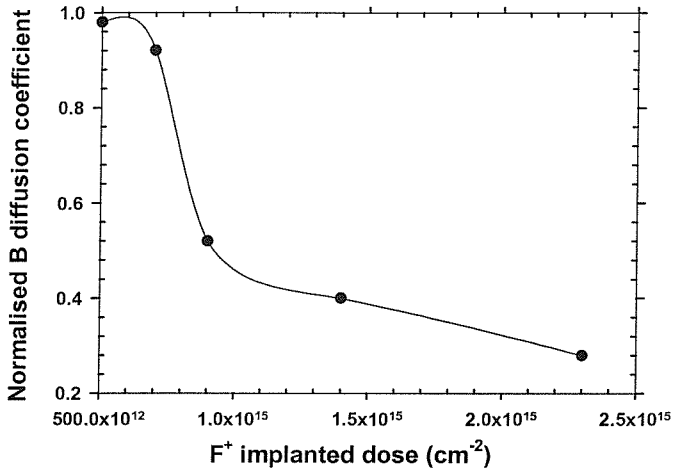

Figure 6.6: A plot of the extracted boron diffusion coefficients of F^+ implanted samples normalised to the diffusion coefficient of the corresponding unimplanted sample (from the same growth) versus F^+ implanted dose for a dose range of $5\times10^{14}cm^{-2}$ to $2.3\times10^{15}cm^{-2}$.

The deep, broad fluorine peak is also present at a depth corresponding with the range of the fluorine implant (0.41μm). For a F^+ dose of $1.4\times10^{15}cm^{-2}$ (figures 6.7(g) and (h)) a shallow double peak is again seen in the $Si_{1-x}Ge_x$ layer, with the two peaks occurring at depths of 0.16 and 0.19μm and corresponding with the positions of the top and bottom $Si_{1-x}Ge_x$/Si heterojunction interfaces. An interesting feature of the peak at the bottom of the heterojunction interface at a depth of 0.19μm is that the fluorine concentration after anneal ($3\times10^{19}cm^{-3}$) is considerably higher than the concentration at the same depth after implant ($1\times10^{19}cm^{-3}$). This indicates that fluorine is being transported into the $Si_{1-x}Ge_x$ layer from the adjacent Si and then accumulates there. The shoulder on the deep fluorine profile is also present between 0.23 and 0.27μm and also the deep fluorine peak at a depth slightly beyond the range

of the fluorine implant (0.41μm) with a peak concentration slightly higher than that after implant.

Figure 6.8 shows fluorine SIMS profiles before and after an anneal at 1000°C for samples (from growth A see figure 6.2) implanted with F^+ only (right column) and with P^+ & F^+ (left column) at high F^+ doses of $2.3\times10^{15}cm^{-2}$ (figures 6.8(a) and (b)) and $1\times10^{16}cm^{-2}$ (figures 6.8(c) and (d)). The corresponding annealed germanium and boron profiles are shown for reference. For both F^+ doses the fluorine profiles of the F^+ implanted samples are almost identical to those of the P^+ & F^+ implanted samples, indicating that the P^+ implant had little effect on the F profiles, which agrees with the profiles in figure 6.7. For a F^+ dose of $2.3\times10^{15}cm^{-2}$ figures 6.8(a) and (b) show that a double fluorine peak is again visible in the $Si_{1-x}Ge_x$ layer, with peaks corresponding with the positions of the top and bottom $Si_{1-x}Ge_x$/Si heterojunction interfaces. The fluorine concentrations at both interfaces after anneal are considerably higher than the equivalent concentrations after implant. This indicates that at F^+ doses of $1.4\times10^{15}cm^{-2}$ and above, fluorine is being transported into the $Si_{1-x}Ge_x$ layer from the adjacent Si layers and is then accumulating in the $Si_{1-x}Ge_x$. A shoulder is again present between 0.22 and 0.28μm, and a deep peak at a depth corresponding with the range of the fluorine implant (0.41μm). A sharp fluorine peak is also present at a depth of 0.57μm, which corresponds with the original growth interface. For a F^+ dose of $1\times10^{16}cm^{-2}$ figures 6.8(c) and (d) show the presence of an additional shallow fluorine peak in the silicon cap layer between 0.03 and 0.08μm. Furthermore, the fluorine shoulder between 0.20 and 0.24μm is more distinct than at lower fluorine doses and the deep fluorine peak is considerably broader.

Table 6.5 summarises the peak fluorine concentrations at the top and bottom $Si_{1-x}Ge_x$/Si heterojunction interfaces before and after implant. The results after anneal

show that once the fluorine peaks in the $Si_{1-x}Ge_x$ layer form at a F^+ implant dose of $9\times10^{14}cm^{-2}$, the concentrations at both interfaces rise strongly with increasing fluorine dose. At high F^+ doses, the fluorine concentrations after anneal become much higher than the equivalent values after implant. It is also interesting to note that for F^+ doses of 9×10^{14} and $1.4\times10^{15}cm^{-2}$, the fluorine concentration after anneal at the bottom interface is significantly higher than at the top interface. The fluorine profiles in figure 6.7 show that this higher fluorine concentration correlates with a higher germanium concentration.

Fluorine implant dose (cm^{-2})	**Peak fluorine concentration in the $Si_{1-x}Ge_x$ layer, (cm^{-3})**			
	After implant		**After anneal**	
	Bottom interface	**Top interface**	**Bottom interface**	**Top interface**
5×10^{14}	3.1×10^{18}	1.9×10^{18}	$<10^{17}$	$<10^{17}$
7×10^{14}	3.7×10^{18}	2.1×10^{18}	$\approx10^{17}$	$\approx10^{17}$
9×10^{14}	6.0×10^{18}	3.9×10^{18}	5×10^{18}	3×10^{17}
1.4×10^{15}	1×10^{19}	7×10^{18}	3×10^{19}	5×10^{18}
2.3×10^{15}	1.3×10^{19}	1×10^{19}	4×10^{19}	6×10^{19}
1×10^{16}	5×10^{19}	-	3×10^{20}	-

Table 6.5: A summary of fluorine concentrations at the top and bottom $Si_{1-x}Ge_x/Si$ heterojunction interfaces after implant and after anneal at 1000°C for fluorine implants at doses in the range of $5\times10^{14}cm^{-2}$ to $1\times10^{16}cm^{-2}$.

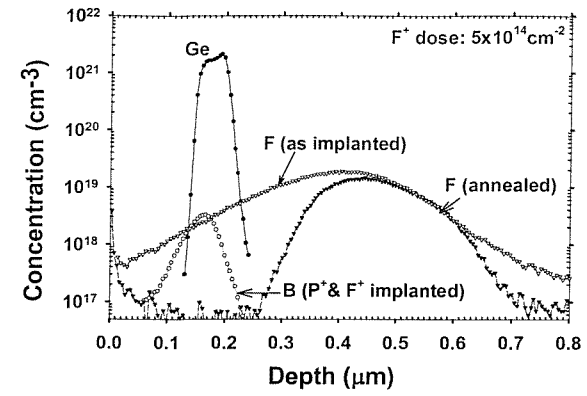

(a)

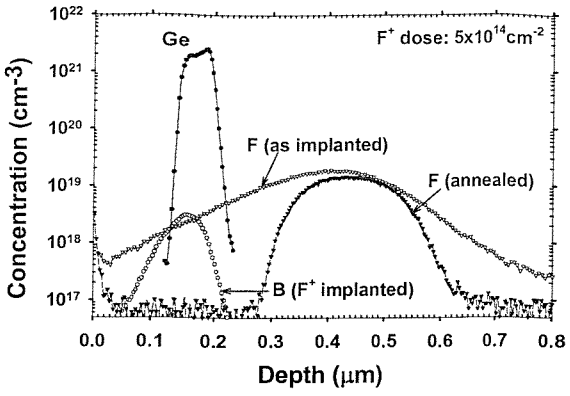

(b)

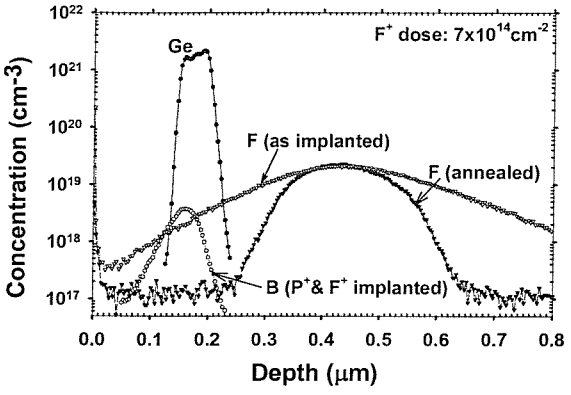

(c)

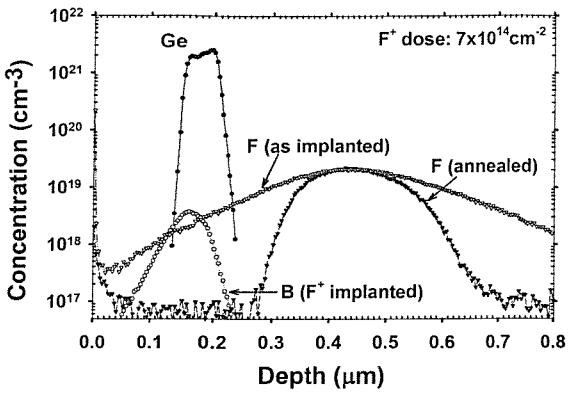

(d)

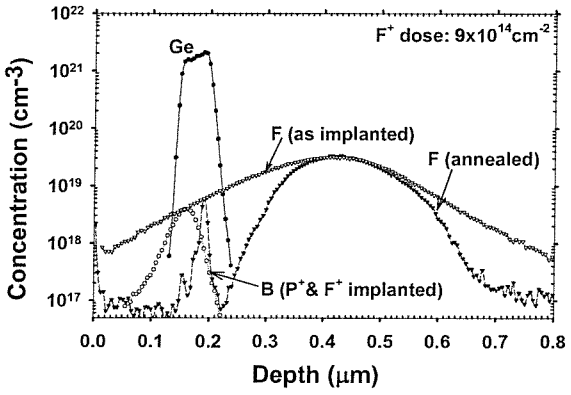

(e)

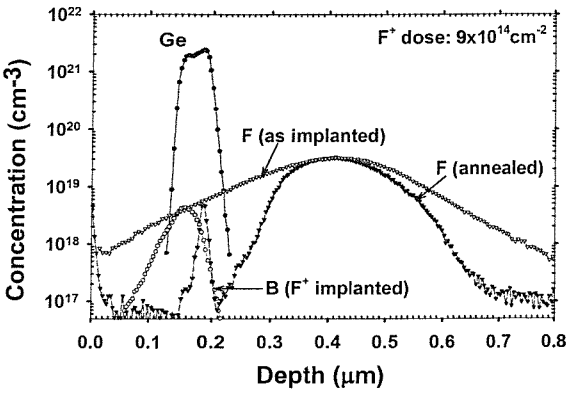

(f)

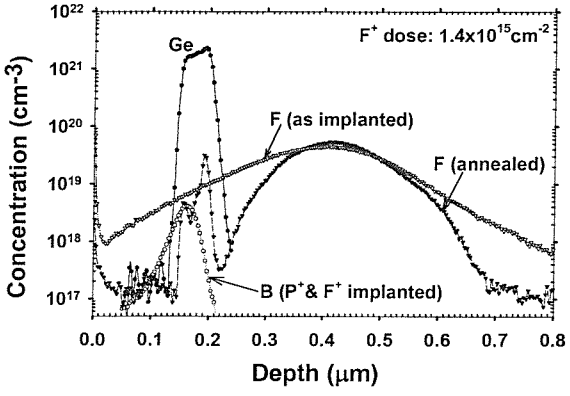

(g)

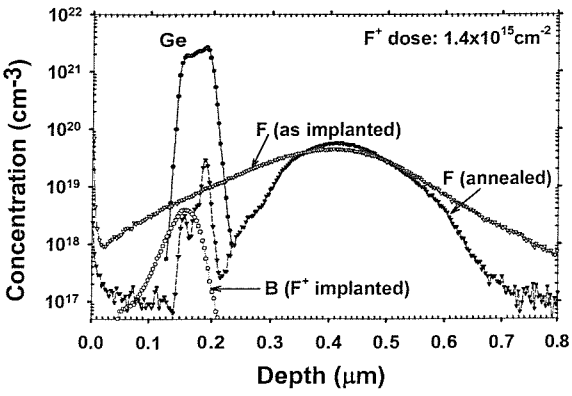

(h)

Figure 6.7: Fluorine SIMS profiles before and after anneal for $Si_{1-x}Ge_x$ samples (growth B) implanted with P^+ & F^+ (left) and F^+ only (right) at F^+ doses of $5\times10^{14}cm^{-2}$(a, b), $7\times10^{14}cm^{-2}$(c, d), $9\times10^{14}cm^{-2}$(e, f), and $1.4\times10^{15}cm^{-2}$(g, h). The corresponding annealed germanium and boron profiles are shown for reference.

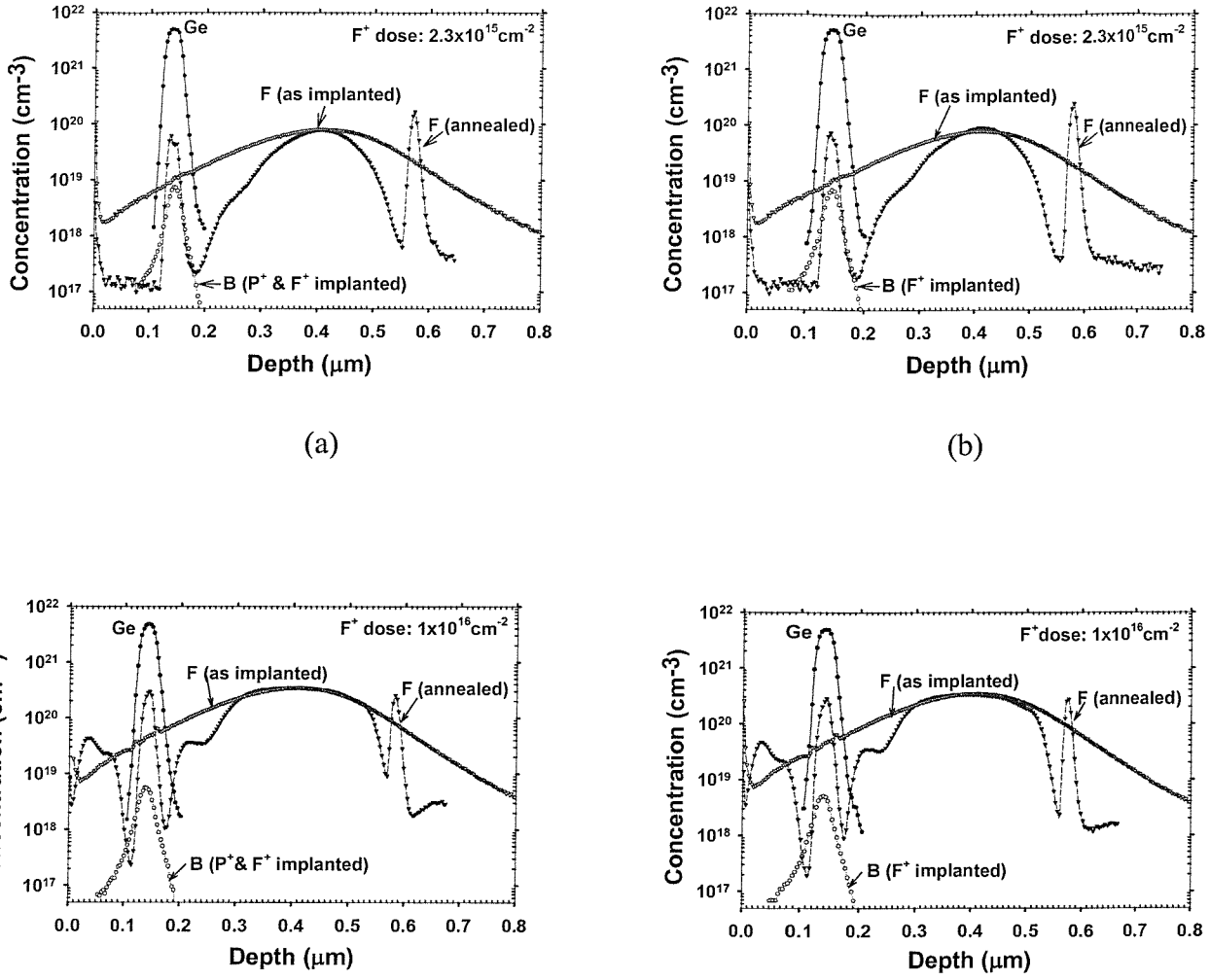

Figure 6.8: Fluorine SIMS profiles before and after anneal for $Si_{1-x}Ge_x$ samples (growth A) implanted with P^+ & F^+ (left) and with F^+ only (right) at F^+ doses of $2.3\times10^{15}cm^{-2}$(a and b), and $1\times10^{16}cm^{-2}$ (c and d). The corresponding annealed germanium and boron profiles are shown for reference.

Table 6.6 shows values of integrated fluorine doses after implant and anneal for F^+ doses in the range of 5×10^{14} cm^{-2} to $1\times10^{16}cm^{-2}$ in samples with and without a P^+ implant (see fluorine profiles in figures 6.7 and 6.8). Total doses after anneal as well as doses in surface peak (0-0.1μm), shallow peak (0.1 to 0.2μm), shoulder (0.2 to

0.28μm) and deep peak (0.28 to 0.7μm) regions are shown. The trends in fluorine dose are very similar for the samples implanted with F^+ only and for samples implanted with both P^+ & F^+, indicating that the P^+ implant has little effect on the fluorine profiles as seen from figures 6.7 and 6.8. The integrated doses after implant are similar to the implanted doses within the SMS dose error range of ±14%. The total integrated doses after anneal all show a loss in fluorine dose during anneal. The loss in fluorine dose decreases as the fluorine implanted dose increases varying from 67% for a 5×10^{14} cm^{-2} F^+ implanted dose to17% for a $1\times10^{16}cm^{-2}$ F^+ implanted dose. This indicates that more fluorine is retained in the samples during annealing as the implanted dose increases. We also notice from the values in table 6.6 that the majority of the fluorine after anneal resides in the deep fluorine peak for all F^+ implanted doses. The shoulder and shallow peak start to appear at the same F^+ implanted dose of 9×10^{14} cm^{-2} and the doses in these regions increase as the implanted dose rises. The surface fluorine peak only appears for the highest implanted dose of $1\times10^{16}cm^{-2}$ and constitutes only 2.8% of the total dose after anneal.

Figure 6.9 shows the as implanted and annealed fluorine SIMS profiles in a $Si_{1-x}Ge_x$ multi-layer structure without any boron marker layer (growth C in table 6.1) after a 288keV, $6\times10^{13}cm^{-2}$ P^+ implant and a 185keV, $2.3\times10^{15}cm^{-2}$ F^+ implant and an anneal of 30s at 1000°C in dry nitrogen. The shallowest $Si_{1-x}Ge_x$ layer lies at a depth of 0.14-0.17μm and shows the presence of a sharp, flat-topped fluorine peak inside the $Si_{1-x}Ge_x$ layer similar to that seen in figure 6.8 (a) for the same F^+ implant dose. The fluorine concentration in the $Si_{1-x}Ge_x$ layer is considerably higher after anneal than after implant, as was also found for the sample with the boron marker layer in figure 6.8 (a). The similarity between the fluorine profiles of samples with and without the boron marker layer indicates that the fluorine peak in the $Si_{1-x}Ge_x$ layer is

not caused by the presence of the boron. The middle $Si_{1-x}Ge_x$ layer lies at a depth of 0.32-0.35μm and again shows the presence of a large fluorine peak with a concentration considerably higher after anneal than after implant. The deepest $Si_{1-x}Ge_x$ layer lies at a depth of 0.51-0.54μm and coincides with the falling edge of the deep fluorine peak (at 0.41μm), which is similar to the deep fluorine peak seen earlier in figure 6.8 (a). The fluorine concentration after anneal remains below that after implant throughout the deepest $Si_{1-x}Ge_x$ layer.

Figure 6.10 compares the annealed fluorine SIMS profiles in $Si_{1-x}Ge_x$ (see figure 6.8 (b)) and Si (see figure 5.5 in chapter 5) samples after a 185keV, $2.3\times10^{15}cm^{-2}$ F^+ implant and an anneal of 30s at 1000°C in dry nitrogen. The fluorine SIMS profile after implant is added for reference. In the silicon sample, a shallow fluorine peak can be seen in a similar position to that in the $Si_{1-x}Ge_x$ sample, but it is considerably broader, extending from about 0.05 to 0.22μm, and at no point is the fluorine concentration higher than the as-implanted fluorine concentration. Whereas, in the $Si_{1-x}Ge_x$ sample the shallow fluorine peak concentration is 8×higher than the concentration after implant at the same depth. This result confirms that the accumulation of fluorine to concentrations much higher than the as-implanted concentration is due to the presence of the $Si_{1-x}Ge_x$ layer.

Implant	SIMS	Total		Surface peak (0-0.1μm)		Shallow peak (0.1-0.2μm)		Shoulder (0.2-0.28μm)		Deep peak (0.28-0.70μm)	
		(cm^{-2})	%	(cm^{-2})	%	(cm^{-2})	%	(cm^{-2})	%	(cm^{-2})	%
$5\times10^{14} + P^+$	6.1×10^{14}	2.0×10^{14}	33	-	-	-	-	-	-	1.9×10^{14}	95
5×10^{14}	6.1×10^{14}	1.9×10^{14}	31	-	-	-	-	-	-	1.8×10^{14}	95
$7\times10^{14} + P^+$	7×10^{14}	3.0×10^{14}	43	-	-	-	-	--	-	2.9×10^{14}	97
7×10^{14}	7×10^{14}	2.9×10^{14}	41	-	-	-	-	-	-	2.8×10^{14}	97
$9\times10^{14} + P^+$	8.8×10^{14}	4.6×10^{14}	52	-	-	6.2×10^{12}	1.3	3.8×10^{12}	0.8	4.5×10^{14}	98
9×10^{14}	8.8×10^{14}	4.4×10^{14}	50	-	-	5.1×10^{12}	1.2	3.0×10^{12}	0.7	4.2×10^{14}	95
$1.4\times10^{15} + P^+$	1.2×10^{15}	7.6×10^{14}	63	-	-	3.9×10^{13}	5.1	1.4×10^{13}	1.8	7.0×10^{14}	92
1.4×10^{15}	1.2×10^{15}	7.8×10^{14}	65	-	-	3.3×10^{13}	4.2	1.1×10^{13}	1.4	7.3×10^{14}	94
$2.3\times10^{15} + P^+$	2.3×10^{15}	1.8×10^{15}	78	-	-	1.3×10^{14}	7.2	4.1×10^{13}	2.3	1.0×10^{15}	89
$1.0\times10^{16} + P^+$	1.0×10^{16}	8.3×10^{15}	83	2.3×10^{14}	2.8	5.7×10^{14}	6.9	4.9×10^{14}	5.9	7.1×10^{15}	86

Table 6.6: A summary of the integrated fluorine doses after implant and anneal for F^+ doses in the range of 5×10^{14} cm^{-2} to $1\times10^{16}cm^{-2}$ in samples with and without a P^+ implant. Total doses after anneal as well as doses in surface peak, shallow peak, shoulder and deep peak regions are shown.

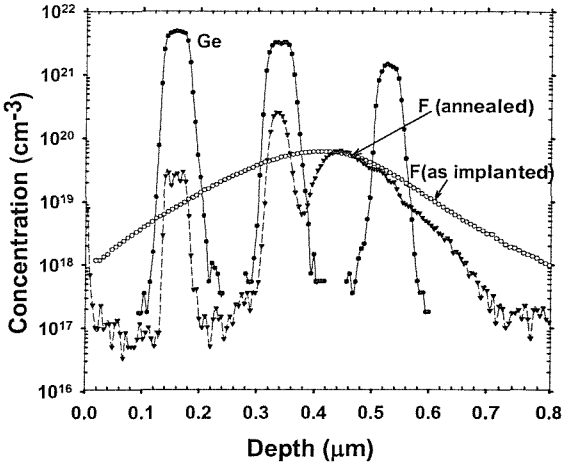

Figure 6.9: Fluorine SIMS profiles before and after anneal for a $Si_{1-x}Ge_x$ multi-layer structure (growth C) implanted with 288keV, $6\times10^{13}cm^{-2}$ P^+ and 185keV, $2.3\times10^{15}cm^{-2}$ F^+ and annealed in nitrogen for 30s at 1000°C.

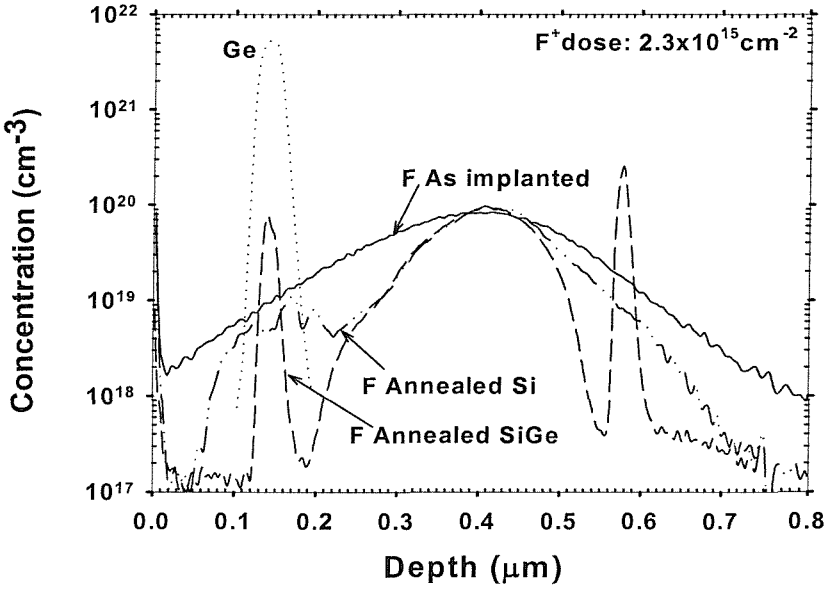

Figure 6.10: Comparison of fluorine SIMS profiles in $Si_{1-x}Ge_x$ and Si samples after a $2.3\times10^{15}cm^{-2}$ F^+ implant and an anneal in nitrogen for 30s at 1000°C.

Figure 6.11 shows a cross-sectional transmission electron microscopy micrograph of a P^+ implanted and annealed (at 1000°C for 30s in nitrogen) $Si_{1-x}Ge_x$ sample (growth A 2Si962 see table 6.1). There are no visible defects in the Si cap, $Si_{1-x}Ge_x$ and Si starter layers.

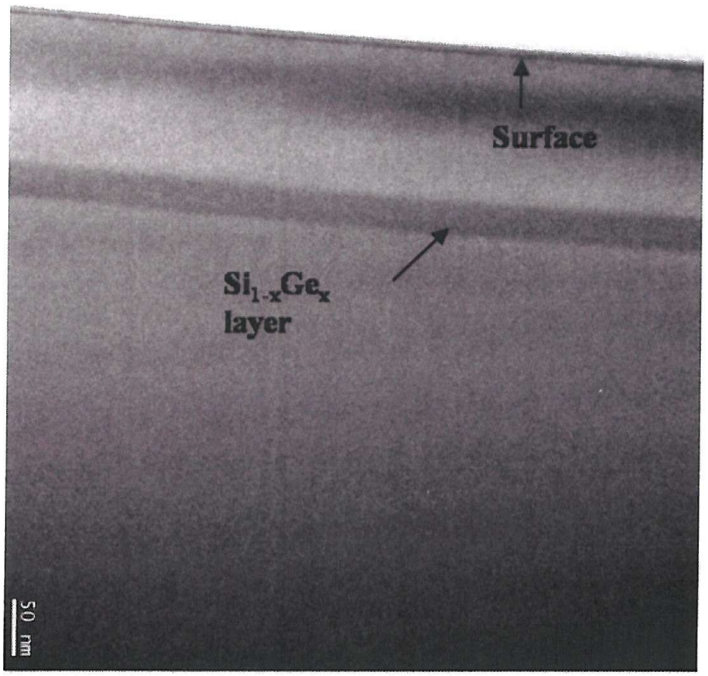

Figure 6.11: A cross-sectional transmission electron microscopy micrograph of a $Si_{1-x}Ge_x$ sample (growth A) implanted with 288 keV, $6x10^{13}cm^{-2}$ P^+ and annealed for 30s in nitrogen at 1000°C.

Figure 6.12 (a) shows a cross-sectional transmission electron microscopy micrograph of a $Si_{1-x}Ge_x$ sample (growth A) implanted with P^+ & F^+ (fluorine implanted dose $5\times10^{14}cm^{-2}$) but not annealed. There is no visible evidence of an amorphous layer. Figure 6.12 (b) shows a diffraction pattern of the same sample, which shows the typical pattern for a crystalline material. Hence, the phosphorus and $5\times10^{14}cm^{-2}$ F^+ implants used did not amorphise the Si and $Si_{1-x}Ge_x$ epitaxial layers.

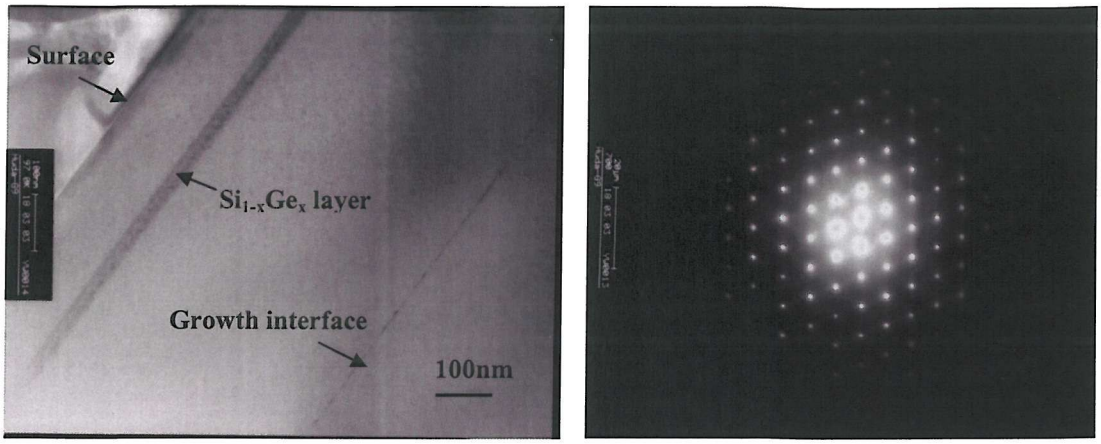

(a) (b)

Figure 6.12: (a) A cross-sectional transmission electron microscopy micrograph of a $Si_{1-x}Ge_x$ sample (growth A) implanted with 288keV, $6x10^{13}cm^{-2}$ P^+ and 185keV, $5\times10^{14}cm^{-2}$ F^+ but not annealed and the corresponding diffraction pattern (b).

Figure 6.13 shows a cross-sectional transmission electron microscopy micrograph of a P^+ &F^+ implanted (fluorine implanted dose $5\times10^{14}cm^{-2}$) $Si_{1-x}Ge_x$ sample (growth A 2Si962) annealed at 1000°C for 30s in nitrogen. The silicon cap layer and the silicon germanium layer appear smooth and defect free, indicating good crystalline quality and no evidence of relaxation within the silicon germanium layer. A band of scattered dislocation loops is seen in the epitaxial silicon layer from a depth of 0.3μm to a depth of 0.51μm. Another band of dislocation loops is seen around the growth interface at a depth of 0.6μm. There are no visible defects beyond 0.63μm. Figure 6.13 (b) is a higher magnification micrograph of the defects regions shown in figure 6.13 (a). The defects consist of dislocation loops with diameters varying from 16nm to 62nm and a defect density of ≈137 defectsμm^{-2}.

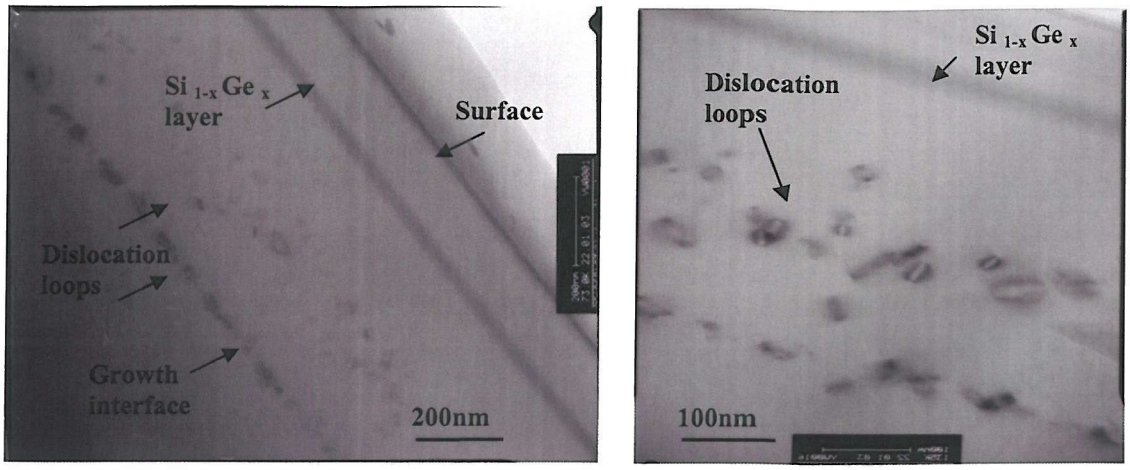

(a) (b)

Figure 6.13: Cross-sectional transmission electron microscopy micrographs of a $Si_{1-x}Ge_x$ sample (growth A) implanted with 288keV, $6x10^{13}cm^{-2}$ P^+ and 185keV, $5\times10^{14}cm^{-2}$ F^+ and annealed for 30s in nitrogen at 1000°C; (a) low magnification, (b) high magnification.

Figure 6.14 shows a cross-sectional transmission electron microscopy micrograph of a $Si_{1-x}Ge_x$ sample (growth A) implanted with P^+ & F^+ (fluorine implanted dose $2.3\times10^{15}cm^{-2}$) but not annealed. There is no visible evidence of an amorphous layer. Hence, the phosphorus and $2.3\times10^{15}cm^{-2}$ F^+ implants used did not amorphise the Si and $Si_{1-x}Ge_x$ epitaxial layers.

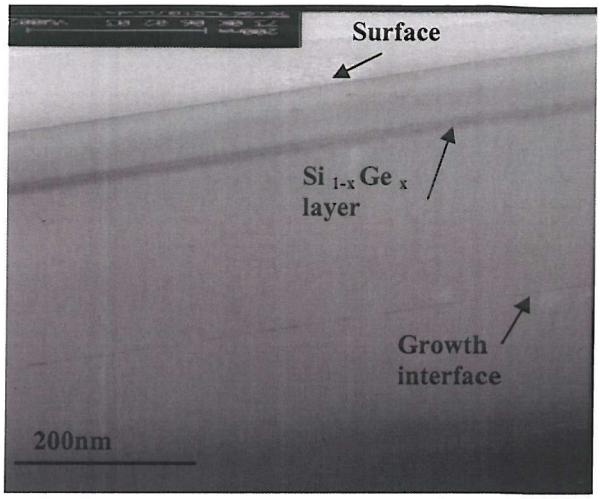

Figure 6.14: A cross-sectional transmission electron microscopy micrograph of a $Si_{1-x}Ge_x$ sample (growth A) implanted with 288keV, $6x10^{13}cm^{-2}$ P^+ and 185keV, $2.3\times10^{15}cm^{-2}$ F^+ but not annealed.

Figure 6.15 shows a cross-sectional transmission electron microscopy micrograph of a P^+ & F^+ implanted (fluorine implanted dose $2.3\times10^{15}cm^{-2}$) $Si_{1-x}Ge_x$ sample (growth A) annealed at 1000°C for 30s in nitrogen. The silicon cap layer and the silicon germanium layer appear smooth and defect free, indicating good crystalline quality and no evidence of relaxation within the silicon germanium layer. A band of high density, with a defect density of ≈375 defectsμm^{-2}, dislocation loops is seen in the epitaxial silicon layer from a depth of 0.28μm to a depth of 0.52μm. Another band of dislocation loops is seen around the growth interface at a depth of 0.6μm. There are no visible defects beyond 0.63μm. Figure 6.15 (b) is a higher magnification micrograph of the defects region. The defects consist of dislocation loops with diameters varying from 16nm to 62nm.

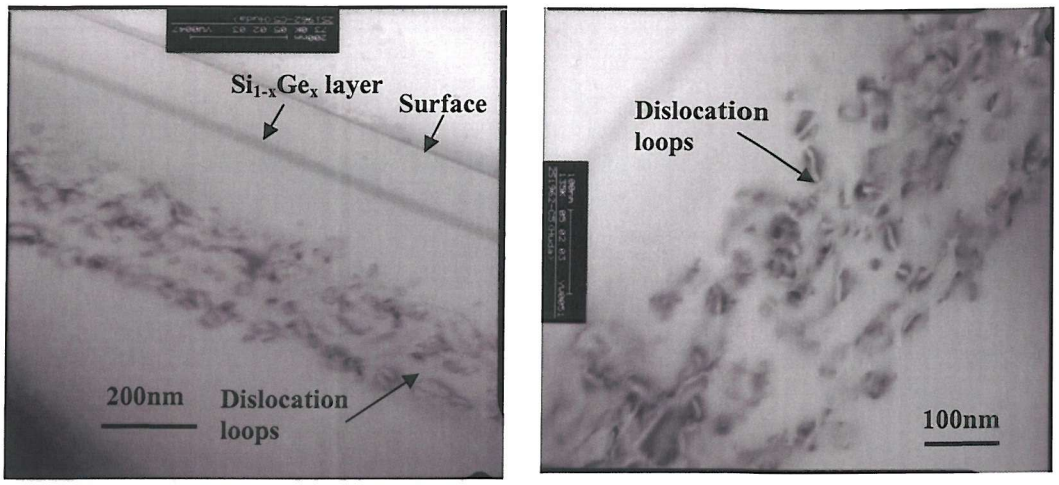

(a) (b)

Figure 6.15: Cross-sectional transmission electron microscopy micrographs of a $Si_{1-x}Ge_x$ sample (growth A) implanted with 288keV, $6x10^{13}cm^{-2}$ P^+ and 185keV, $2.3\times10^{15}cm^{-2}$ F^+ and annealed for 30s in nitrogen at 1000°C; (a) low magnification, (b) high magnification.

Figure 6.16 shows a cross-sectional transmission electron microscopy micrograph of a $Si_{1-x}Ge_x$ sample (growth A) implanted with P^+ & F^+ (fluorine implanted dose $1\times10^{16}cm^{-2}$) but not annealed. There are visible defects in the silicon and silicon germanium layers indicating poor crystalline quality of the as implanted layer. However, there is no evidence of amorphisation, hence, both the P^+ and $1\times10^{16}cm^{-2}$ F^+ implants used did not amorphise the Si and $Si_{1-x}Ge_x$ epitaxial layers.

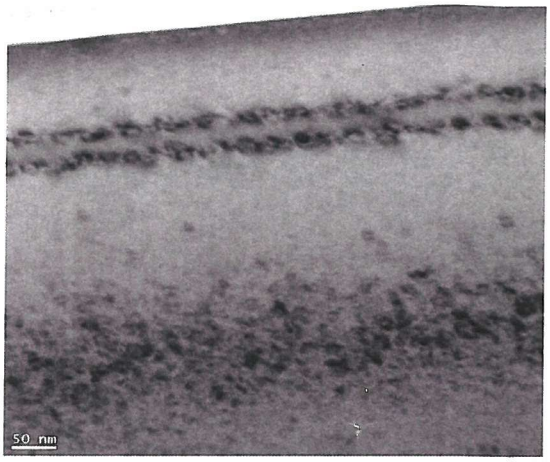

Figure 6.16: A cross-sectional transmission electron microscopy micrograph of a $Si_{1-x}Ge_x$ sample (growth A) implanted with 288keV, $6x10^{13}cm^{-2}$ P^+ and 185keV, $1\times10^{16}cm^{-2}$ F^+ but not annealed.

Figure 6.17 shows a cross-sectional transmission electron microscopy micrograph of a P^+ & F^+ implanted (fluorine implanted dose $1\times10^{16}cm^{-2}$) $Si_{1-x}Ge_x$ sample (growth A) annealed at 1000°C. The silicon cap layer and the silicon germanium layer appear smooth and defect free, indicating good crystalline quality and no evidence of relaxation within the silicon germanium layer. A band of very high density dislocation loops is seen in the epitaxial silicon layer from a depth of 0.28μm to a depth of 0.55μm, almost overlapping with another band of dislocation loops around the growth interface at a depth of 0.6μm (as seen in figure 6.17 (b)). Figure 6.17 (b) is a higher magnification micrograph of the defects region. The defects consist of very high density with a defect density of ≈443 defectsμm^{-2}, dislocation loops with varying shapes and diameters varying from 31nm to 77nm.

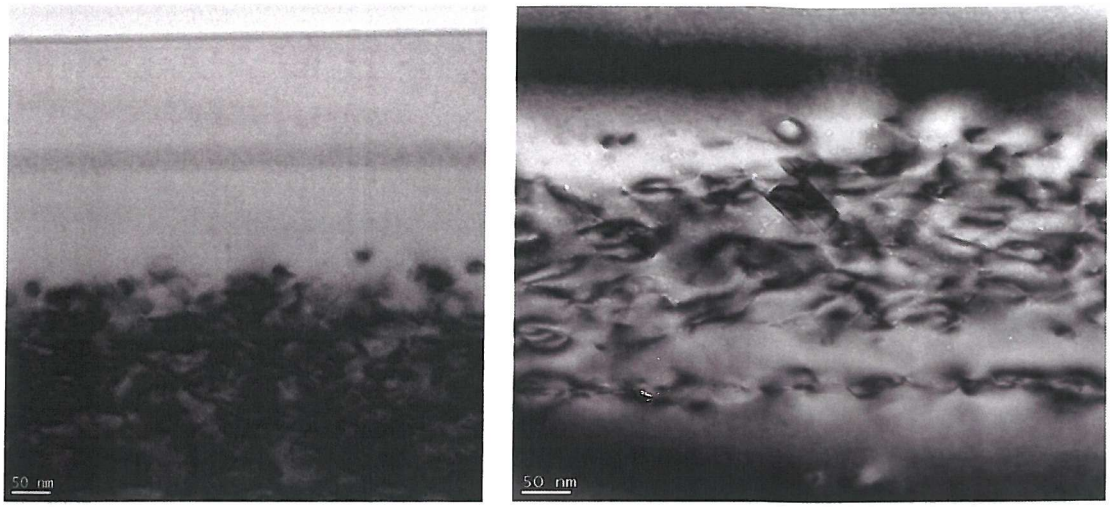

(a) (b)

Figure 6.17: Cross-sectional transmission electron microscopy micrographs of a $Si_{1-x}Ge_x$ sample (growth A) implanted with 288keV, $6x10^{13}cm^{-2}$ P^+ and 185keV, $1\times10^{16}cm^{-2}$ F^+ and annealed for 30s in nitrogen at 1000°C; (a) low magnification, (b) high magnification.

Figure 6.18 shows the cross-sectional transmission electron microscopy micrograph of a P^+ & F^+ implanted (fluorine implanted dose $2.3\times10^{15}cm^{-2}$) $Si_{1-x}Ge_x$ multi layer sample (growth C) annealed at 1000°C for 30s in nitrogen. The silicon cap layer and the first silicon germanium layer (closest to the surface) appear smooth and defect free, indicating good crystalline quality and no evidence of relaxation within the silicon germanium layer. A band of dislocation loops is seen in the epitaxial silicon and silicon germanium layers from a depth of 0.32μm to a depth of 0.68μm. In the second (middle) silicon germanium layer the dislocation loops appear as a confined band along the layer. However, the deepest silicon germanium layer is not clearly distinguished from the adjacent silicon layers. There are no visible defects beyond 0.68μm. Figure 6.18 (b) is a higher magnification micrograph of the defects region. The defects consist of dislocation loops with diameters varying from 16nm to 49nm.

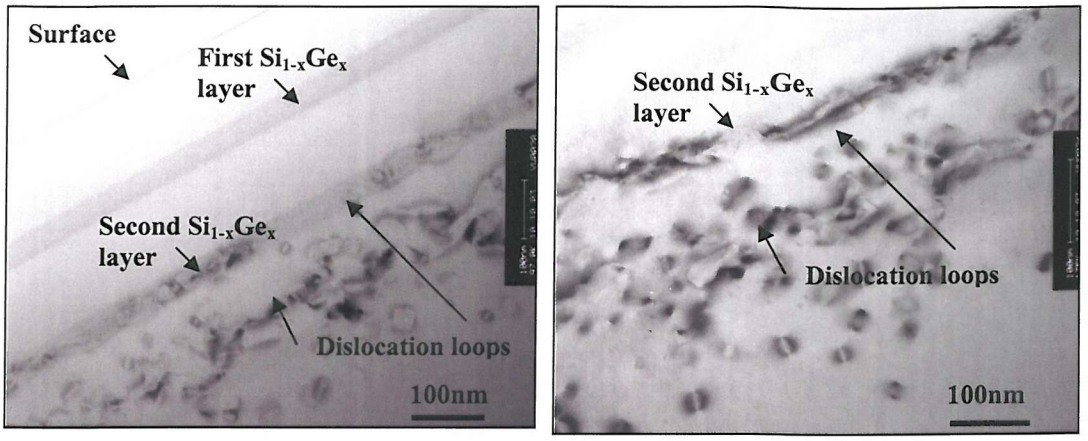

(a) (b)

Figure 6.18: Cross-sectional transmission electron microscopy micrographs of a $Si_{1-x}Ge_x$ multilayer sample (growth C) implanted with 288keV, $6x10^{13}cm^{-2}$ P^+ and 185keV, $2.3\times10^{15}cm^{-2}$ F^+ and annealed for 30s in nitrogen at 1000°C; (a) low magnification, (b) high magnification.

6.4 Discussion

The results in figure 6.1 and 6.2 show a reduction in boron thermal diffusion in $Si_{1-x}Ge_x$ at a F^+ dose of $9\times10^{14}cm^{-2}$. The extracted diffusion coefficients values in table 6.4 and the results in figure 6.6 show that the reduction in boron thermal diffusion in $Si_{1-x}Ge_x$ increases as the F^+ implant dose increases. The reduction factors in boron diffusion coefficients increase from 1.9 to 2.5 and 3.5 (see table 6.4) for F^+ implanted doses of $9\times10^{14}cm^{-2}$, $1.4\times10^{15}cm^{-2}$ and 2.3×10^{15} cm^{-2} respectively. These reduction factors in boron thermal diffusion are comparable to those obtained in silicon 1.9 and 3.7 for F^+ implanted doses of $1.4\times10^{15}cm^{-2}$ and 2.3×10^{15} cm^{-2} respectively (table 5.1 in chapter 5). This indicates the effect of F^+ implantation on the suppression of boron diffusion is similar in Si and $Si_{1-x}Ge_x$. The greater reduction obtained for the 2.3×10^{15} cm^{-2} F^+ implanted dose compared to the 1×10^{16} cm^{-2} F^+

implanted dose may suggest that the fluorine is a little less effective at very high doses, however this result needs further verification.

The results in figures 6.1 and 6.2 for the samples implanted with F^+ show a correlation between a reduction in boron thermal diffusion in $Si_{1-x}Ge_x$ and the appearance, at a F^+ dose of $9\times10^{14}cm^{-2}$, of a shallow fluorine peak in the $Si_{1-x}Ge_x$ layer in figures 6.7 and 6.8. In contrast the results in figures 6.1 and 6.2 for the samples implanted with F^+ and P^+ show that boron transient enhanced diffusion is suppressed for all fluorine doses, even at the lowest fluorine dose of $5\times10^{14}cm^{-2}$ and that only the deep fluorine peak is present at this dose (figure 6.7(a)). It can therefore be inferred that the shallow fluorine peak is responsible for the reduction of boron thermal diffusion and the deep fluorine peak for the suppression of boron transient enhanced diffusion.

The shallow fluorine peaks in the $Si_{1-x}Ge_x$ layer in figure 6.8(b) lie at depths of 0.16 and 0.19μm, which correspond to 0.35 and $0.48R_p$, where R_p is the range of the fluorine implant (0.41μm). Simulations of vacancy and interstitial profiles after implantation [13] [14] have predicted a vacancy-rich region extending from the surface to a depth approaching the implantation range, R_p, and a deeper interstitial-rich region peaking at a depth just beyond R_p. This indicates that the fluorine peaks in the $Si_{1-x}Ge_x$ layer lie in the vacancy-rich region of the damage profile. The TEM micrographs in figure 6.15 (a) show no evidence of defects in the silicon and $Si_{1-x}Ge_x$ layers from the surface to a depth of about 0.3μm and hence any trapping of fluorine at defects in the $Si_{1-x}Ge_x$ layer must be due to defects that are too small to resolve by TEM. There is considerable evidence in the literature for the formation of vacancy-fluorine clusters [7, 15, 16] in silicon, that are too small to be resolved by TEM. The results in this chapter are similar to the results seen in chapter 5, on the effect of

fluorine implantation dose on boron thermal diffusion in Si, where it was shown that vacancy-fluorine clusters were responsible for a reduction in boron thermal diffusion above a critical fluorine dose of 9×10^{14} to $1.4\times10^{15}cm^{-2}$. In this chapter, similar behaviour is seen, although the critical fluorine dose in $Si_{1-x}Ge_x$ is a little lower than that in silicon, lying between 7×10^{14} and $9\times10^{14}cm^{-2}$. Given the similarity of the $Si_{1-x}Ge_x$ results with results in silicon, we conclude that the fluorine peaks in the $Si_{1-x}Ge_x$ layer are due to fluorine trapped at vacancy-fluorine clusters. These clusters would be expected to give rise to a suppression of the interstitial concentration in the $Si_{1-x}Ge_x$ layer, since any interstitials in the $Si_{1-x}Ge_x$ could be annihilated at the clusters. Since boron diffusion in silicon and $Si_{1-x}Ge_x$ is mediated by interstitials, an under-saturation of the interstitial concentration in the $Si_{1-x}Ge_x$ layer would explain the suppression of boron thermal diffusion seen for fluorine doses of $9\times10^{14}cm^{-2}$ and above.

Another possibility is a chemical interaction between the boron and the fluorine, which would explain the presence of the shallow fluorine peak [6, 17]. However, the results in figure 6.9 show a shallow fluorine peak in the $Si_{1-x}Ge_x$ layer closest to the surface, whilst there is no boron in this layer. Hence, the possibility that the shallow fluorine peak is due to a chemical interaction between boron and fluorine can be discounted. This agrees with the results in chapter 5 where a similar conclusion was reached.

The deep fluorine peak (figure 6.8 (a)) lies at a depth corresponding approximately with the range of the fluorine implant and hence is largely in the interstitial-rich region of the fluorine implant damage profile. Thus it is likely that the deep fluorine peak is related in some way to interstitial-fluorine defects. Comparing the fluorine SIMS profiles shown in figure 6.8 (a) with the TEM micrograph shown in figure 6.15 (a) we notice interesting correlations. We notice that the deep fluorine

peak in the P^+ & F^+ implanted sample (figure 6.8 (a)), which extends within a depth range of 0.28μm to 0.55μm, coincides with the first band of dislocation loops seen in figure 6.15 (a) (from a depth of 0.28μm to a depth of 0.52μm). Thus there is a good correlation with the depth of the dislocation loops, indicating that the deep fluorine peak is due to fluorine trapping at the dislocation loops. This 185keV, $2.3x10^{15}cm^{-2}$ F^+ implant does not amorphise the silicon layer, as seen from figure 6.14, and hence these loops are most probably sub-amorphising defects resulting from a super saturation of interstitials in this region [18]. Similar interstitial-type defects were reported due to a 500keV $5x10^{15}cm^{-2}$ F^+ implant where SIMS showed fluorine gettering to the defects [16]. Similar perfect and faulted dislocation loops have also been reported for BF_2^+ implanted and RTA annealed silicon layers [19]. Thus it can be concluded that the deep fluorine peaks seen in figures 6.7 and 6.8 are due to fluorine trapped at interstitial-type dislocation loops.

The generally accepted model for transient enhanced diffusion of boron is that self-interstitials are lost from extended {311} defects by emission of single interstitial atoms [20]. The released interstitials either diffuse to other defects, such as dislocation loops (Ostwald ripening), or to the surface (dissolution). The diffusion of interstitials to the surface gives rise to transient enhanced diffusion in boron layers located near the surface. Comparing the cross-sectional transmission electron microscopy micrographs of the P^+ only implanted and annealed sample shown in figure 6.11 with that of the P^+ & $5\times10^{14}cm^{-2}$ F^+ implanted and annealed sample in figure 6.13, we notice that there are no visible defects close to the implantation range for the P^+ (0.41μm) only implanted sample (figure 6.11). However, there is a band of dislocations loops centred around the implantation range and spreading from a depth of 0.3μm to a depth of 0.51μm in the P^+& $5\times10^{14}cm^{-2}$ F^+ implanted sample (figure

6.13).This indicates that fluorine plays a key role in the formation of the band of dislocation loops. This result suggests that fluorine enhances the Ostwald ripening process, so that self-interstitials lost from {311} defects diffuse to the dislocation loops, rather than to the surface. This mechanism would reduce the backflow of interstitials to the surface and hence would explain the suppression of boron transient enhanced diffusion seen in samples implanted with F^+.

The fluorine profiles in figures 6.7 and 6.8 show the presence of a shoulder on the deep fluorine peak at a depth between about 0.22μm and 0.28μm (0.54 and $0.68R_p$) for fluorine doses at and above $9\times10^{14}cm^{-2}$. Like the shallow fluorine peak, this shoulder also correlates with the suppression of boron thermal diffusion, as it is present at the three highest doses where boron thermal diffusion is suppressed, but is absent at the two lowest doses where the fluorine has no effect on the boron thermal diffusion. This fluorine shoulder could therefore play a role in suppressing boron thermal diffusion in the silicon substrate adjacent to the $Si_{1-x}Ge_x$ layer. There are no visible defects in the Si layers (where the shoulder is seen) from the cross-sectional transmission electron microscopy micrographs in figures 6.15 and 6.17. The shoulder is in the vacancy rich region of the fluorine damage profile. Hence, this shoulder is due to vacancy-fluorine clusters, similar to that seen in the silicon samples in chapter 5.

The fluorine SIMS profiles for the samples implanted with $1\times10^{16}cm^{-2}$ F^+ in figures 6.8(c) and (d) show the presence of an additional surface fluorine peak in the silicon cap layer at a depth between 0.03 and 0.07μm, where no visible damage is seen from the cross-sectional transmission electron microscopy micrograph in figure 6.17. This surface fluorine peak is in the vacancy-rich region of the fluorine damage profile and hence is likely to be due to vacancy-fluorine clusters. The results in

chapter 5 showed that a critical fluorine concentration after implant of 3.6-6.6×$10^{18}$$cm^{-3}$ was needed for vacancy-fluorine clusters to form in silicon. Figure 6.8(c) shows that the fluorine concentration after implant in the vicinity of this additional surface fluorine peak is between 9×10^{18} and 2.4×$10^{19}$$cm^{-3}$$cm^{-3}$, which is well above the critical concentration for vacancy-fluorine cluster formation. The presence of this additional shallow fluorine peak in figure 6.8(c) can therefore be explained by the high fluorine concentration in the silicon cap layer after a 1×$10^{16}$$cm^{-2}$ F^+ implant.

The deep fluorine peak seen for all fluorine doses (figures 6.7 and 6.8) is similar to that seen before in chapter 5. As the implanted F^+ dose increases the peak concentration in deep F^+ peak increases (figures 6.7 and 6.8) this correlates with an increase in dislocation loops density from ≈137 to 375 and to 443 defectsμm^{-2} for F^+ doses of 5×$10^{14}$$cm^{-2}$, 2.3×$10^{15}$$cm^{-2}$ and 1×$10^{16}$$cm^{-2}$ as seen in figures 6.13, 6.15 and 6.17 respectively. This is most evident for the 1×$10^{16}$$cm^{-2}$ F^+ dose where the deep fluorine peak is very broad (figure 6.8(d)) and correlates with a very high density (443 defectsμm^{-2}) and broad dislocation loops band extending from a depth of 0.28μm to a depth of 0.55μm in figure 6.17.

Correlating the fluorine SIMS (figure 6.9) of the $Si_{1-x}Ge_x$ multi-layer structure, with the cross-sectional transmission electron microscopy micrographs in figure 6.18 allows us to explain the origin of the fluorine peaks seen in figure 6.9. The fluorine peak inside the shallowest $Si_{1-x}Ge_x$ layer (figure 6.9) is similar to that seen in figure 6.8 (a) for the same fluorine dose. Figure 6.18 shows no visible defects in the shallowest $Si_{1-x}Ge_x$ layer. This layer lies at a depth of 0.13μm to a depth of 0.19μm ($0.32R_p$ to $0.46R_p$), which is in the vacancy rich region of the fluorine implant. Hence, the peak inside the shallowest $Si_{1-x}Ge_x$ layer (figure 6.9) is due to vacancy-fluorine

clusters. The middle $Si_{1-x}Ge_x$ layer lies at a depth of 0.32μm to a depth of 0.36μm (0.78 R_p to 0.88 R_p) and also shows the presence of a fluorine peak within it. However, there is a band of dislocation loops visible in this $Si_{1-x}Ge_x$ layer, which are similar to those seen in the $Si_{1-x}Ge_x$ layer of the low energy F^+ implanted sample in chapter 4 (figure 4.4), which extended from a depth of 0.064μm to a depth of 0.118μm (0.7R_p to 1.3R_p). This fluorine peak is close to the implant range (0.78R_p to 0.88R_p) and is similar to that seen previously in chapter 4 in the $Si_{1-x}Ge_x$ layer of the low energy F^+ implanted sample (figure 4.3(a)) (0.7R_p to 1.3R_p), which suggests that it is due to fluorine trapping at the interstitial type dislocation loops in this layer resulting from implantation damage. However, further investigation is needed to fully explain this result. The deepest $Si_{1-x}Ge_x$ layer lies at a depth of 0.5μm to a depth of 0.56μm (1.2R_p to 1.4R_p) and the fluorine profile in this layer is very different than those in the two shallower layers. In the deepest $Si_{1-x}Ge_x$ layer, the fluorine concentration remains below the level of the as-implanted fluorine profile throughout the layer, whereas in the two shallower $Si_{1-x}Ge_x$ layers the fluorine concentration rises considerably above the as-implanted concentration. This $Si_{1-x}Ge_x$ layer is not clearly defined in the cross-sectional transmission electron microscopy micrograph (figure 6.18 (a)) as the middle $Si_{1-x}Ge_x$ layer, and the dislocation loops are not confined within it as was the case in the middle $Si_{1-x}Ge_x$ layer. This could be due to the lower Ge content in this layer (3%) compared with the middle $Si_{1-x}Ge_x$ layer (6%), resulting in a layer which is almost like Si and hence no distinct fluorine peak is seen. It can therefore be concluded that there is no evidence of vacancy-fluorine clusters in the deepest $Si_{1-x}Ge_x$ layer. This is as expected, because the deepest $Si_{1-x}Ge_x$ layer (1.2R_p to 1.4R_p) lies well within the interstitial-rich region of the fluorine implant damage.

The evolution of the shapes of the fluorine peaks in the $Si_{1-x}Ge_x$ layer in figures 6.7 and 6.8 with increasing fluorine dose shows some interesting trends. For fluorine doses of 9×10^{14} and $1.4\times10^{15}cm^{-2}$ the fluorine concentration after anneal is much higher at the bottom heterojunction interface than the top interface, as shown in table 6.5. Figure 6.7 shows that the fluorine concentration at the interfaces correlates with the germanium concentrations, which are $2.1\times10^{21}cm^{-3}$ at the bottom interface and $1.6\times10^{21}cm^{-3}$ at the top interface. For a fluorine dose of $2.3\times10^{15}cm^{-2}$, the fluorine concentrations after anneal at the two interfaces are similar, which correlates with very similar germanium concentrations at the two interfaces. This correlation between fluorine and germanium concentrations suggests that the concentration of vacancy-fluorine clusters in the $Si_{1-x}Ge_x$ layer increases with germanium content. The fluorine profiles in figures 6.7 and 6.8 also show that the fluorine concentration in the silicon layers immediately adjacent to the $Si_{1-x}Ge_x$ layer is much lower than in the $Si_{1-x}Ge_x$ layer. The sharpness of the shallow fluorine peak and its presence with in the germanium profile compared to the broadness of the shallow fluorine peak observed in silicon (figure 6.10), also indicates that this is an effect of the germanium. This result implies a transport of fluorine (and possibly also vacancies) during the anneal from the adjacent Si into the $Si_{1-x}Ge_x$ layer, where it accumulates and reaches a level much higher than was present after implant. This result, and the above dependence of fluorine concentration on germanium content, suggests that vacancy-fluorine clusters form more readily in $Si_{1-x}Ge_x$ than in Si, which could be explained by the lower formation energy of vacancies in Ge than in Si, as reported by Dalpian *et al.* [21] or by the selective trapping of vacancies by germanium in silicon reported by Brelot [22]. This might lead to higher concentrations of vacancy-fluorine clusters in $Si_{1-x}Ge_x$ than Si and hence explain the accumulation of fluorine in the $Si_{1-x}Ge_x$ and the lower

critical dose for boron thermal diffusion suppression in $Si_{1-x}Ge_x$, lying between 7×10^{14} and $9\times10^{14}cm^{-2}$, compared to silicon, lying between 9×10^{14} and $1.4\times10^{15}cm^{-2}$.

For devices like $Si_{1-x}Ge_x$ heterojunction bipolar transistors (HBTs), where the boron needs to be confined within the $Si_{1-x}Ge_x$ layer, the above migration of fluorine from the adjacent silicon into the $Si_{1-x}Ge_x$ has important benefits. This mechanism automatically leads to a high fluorine concentration in the $Si_{1-x}Ge_x$ layer, which is precisely where the boron profile is located in a $Si_{1-x}Ge_x$ HBT. The effect of the fluorine in reducing the boron thermal diffusion is therefore automatically maximised. Furthermore, this transport of fluorine into the $Si_{1-x}Ge_x$ layer implies that high concentrations of fluorine can be obtained in the $Si_{1-x}Ge_x$ layer without the need to precisely position the fluorine implant with respect to the $Si_{1-x}Ge_x$ layer.

6.5 Conclusions

A study has been carried out of the effect of fluorine implants with doses in the range of $5\times10^{14}cm^{-2}$ to $1\times10^{16}cm^{-2}$ on the transient enhanced diffusion and thermal diffusion of boron in $Si_{1-x}Ge_x$. A reduction of boron thermal diffusion is observed for F^+ doses at and above a dose of $9\times10^{14}cm^{-2}$, whereas a suppression of boron transient enhanced diffusion is observed for all F^+ doses. This reduction in boron thermal diffusion increases with increase in fluorine dose. The reduction factors in boron thermal diffusion coefficients in $Si_{1-x}Ge_x$ increase from 1.9 to 2.5 and 3.5 for F^+ implanted doses of $9\times10^{14}cm^{-2}$, $1.4\times10^{15}cm^{-2}$ and 2.3×10^{15} cm^{-2} respectively. The reduction of boron thermal diffusion correlates with the appearance of fluorine peaks in the $Si_{1-x}Ge_x$ layer at and above a dose of $9\times10^{14}cm^{-2}$. Cross-sectional transmission electron microscopy micrographs show that there are no extended defects in the Si_{1-}

$_xGe_x$ layer, and hence it is proposed that the fluorine peaks are due to vacancy-fluorine clusters. The reduction in boron thermal diffusion above the critical F^+ dose is then explained by the presence of the vacancy-fluorine clusters, which suppress the interstitial concentration in the $Si_{1-x}Ge_x$ layer. The suppression of boron transient enhanced diffusion correlates with a deep fluorine peak around the range of the fluorine implant and cross-sectional transmission electron microscopy micrographs show that this peak is due to a band of dislocation loops. The suppression of TED by fluorine is then explained by the influence of the loops in suppressing the backflow of interstitials to the surface. Analysis of the SIMS profiles shows that fluorine is transported from the adjacent silicon into the $Si_{1-x}Ge_x$ layer during anneal and reaches concentrations much higher than observed after implant. This mechanism would give benefits in devices like $Si_{1-x}Ge_x$ HBTs, where the boron profile needs to be confined within the $Si_{1-x}Ge_x$ layer, since a high fluorine concentration is automatically obtained in the vicinity of the boron profile, which maximises the effect of fluorine in suppressing boron diffusion.

References

1. R. G. Wilson, "Boron, fluorine and carrier profiles for B and BF_2 implants into crystalline and amorphous Si"; Journal of Applied Physics, vol. 54 (12), pp. 6879-6889, (1983).
2. K. Ohyu, T. Itoga and N. Natsuaki, "Advantages of fluorine introduction in boron implanted shallow p+/n junction formation"; Japanese Journal of Applied Physics, vol. 29, pp. 457-462, (1990).
3. D. Fan, J. M. Parks and R. J. Jaccodine; "Effect of fluorine on the diffusion of through-oxide implanted boron in silicon"; Applied Physics Letters, vol. 59 (10), pp. 1212-1214, (1991).
4. L. Y. Krasnobaev, N. M. Omelyanovskaya, V. V. Makarov, "The effect of fluorine on the redistribution of boron in ion implanted silicon"; Journal of Applied Physics, vol. 74 (10), pp. 6020-6022, (1993).
5. J. Liu, D. F. Downey, K. S. Jones and E. Ishida, "Fluorine effect on boron diffusion: chemical or damage?"; Proceedings International Conference Ion Implantation Technology, pp. 951-954, (1999).
6. L. S. Robertson, P. N. Warnes, K. S. Jones, S. K. Earles, M. E. Law, D. F. Downey, S. Falk and J. Liu. "Junction depth reduction of ion implanted boron in silicon through fluorine ion implantation"; Materials Research Society Symposium Proceedings, vol. 610, pp. B4.2.1-B4.2.6, (2000).

7. T. S. Shano, R. Kim, T. Hirose, Y. Furuta, H. Tsuji, M. Furuhashi and K. Taniguchi, "Realization of ultra-shallow junction: suppressed boron diffusion and activation by optimised fluorine co-implantation"; Technical Digest of the International Electron Devices Meeting IEDM, pp. 37.4.1-37.4.4, (2001).
8. E. Ishida, D. F. Downey, K. S. Jones and J. Liu, "The chemical effect of fluorine on boron transient enhanced diffusion"; Proceedings International Conference Ion Implantation Technology, vol. 2, pp. 909-912, (1999).
9. B. Martinet, H. Baudry, O. Kermarree, Y. Campidelli, M. Laurens, M. Marty, T. Schwartzmann, A. Monroy, D. Bensahel and A. Chantre, "100GHz SiGe:C HBTs using non selective base epitaxy"; Proceedings of the European Solid State Device Research Conference ESSDERC, pp. 97-100, (2001).
10. J. M. Bonar, B. M. McGregor, N. E. B. Cowern, A. Dan, G. A. Cooke and A. F. W. Willoughby, "Furnace and RTA injection of point defects into CVD-grown B doped Si and SiGe"; Materials Research Society Symposium Proceedings, vol. 610, pp. B4.9.1-B4.9.6, (2000).
11. K. Rajendran and W. Schoenmaker, "Studies of boron diffusivity in strained Si_{1-x} Ge_x epitaxial layers"; Journal of Applied Physics, vol. 89 (2), pp. 980-987, (2001).
12. G. H. Loechelt, G. Tam, J. W. Steele, L. K. Knoch, K. M. Klein, J. K. Watanabe and J. W. Christiansen, "Measurement and modelling of boron diffusion in Si and $Si_{1-x}Ge_x$ epitaxial layers during rapid thermal annealing"; Journal pf Applied Physics, vol. 89 (2), pp. 980-987, (2001).

13. M. D. Giles, "Transient phosphorus diffusion below the amorphization threshold"; Journal of the Electrochemical Society, vol. 138, pp. 1160-1165, (1991).

14. A. Sultan, S. Banerjee, S. List, V. McNeil, "An approach using a subamorphizing threshold dose silicon implant of optimal energy to achieve shallower junctions"; Journal of Applied Physics, vol. 83 (12), pp. 8046-8050, (1998).

15. M. Diebel, S. Chakravarthi, C. F. Machala, S. Ekbote, A. Jain and S. T. Dunham, "Investigation and modelling of fluorine co-implantation effects on dopant redistribution"; Materials Research Society Symposium Proceedings; vol. 765, pp. D6.15.1-D6.15.6, (2003).

16. X. D. Pi, C. P. Burrows and P. G. Coleman, "Fluorine in silicon: diffusion, trapping and precipitation"; Physical Review Letters, vol. 90 (15), pp.155901-1 - 155901-4, (2003).

17. A. Dusch, J. Marcon, K. Masmoudi, K. Ketata, F. Olivie, M. Benzohra and M. Ketata, "Influence of fluorine on the simulation of the transient enhanced diffusion of 15keV BF_2^+ ion implantation into silicon"; Nuclear Instruments and Methods in Physics Research B, vol. 186, pp. 360-365, (2002).

18. K. S. Jones, S. Prussin and E. R. Weber, "A systematic Analysis of defects in ion implanted silicon"; Applied Physics A Solids and Surfaces, vol. 45, pp. 1-34, (1988).

19. I-W. Wu, R. T. Fulks and J. C. Mikkelsen Jr., "Optimisation of BF_2^+ implanted and rapidly annealed junctions in silicon"; Journal of Applied Physics, vol. 60 (7), pp. 2422-2438, (1986).

20. B. Colombeau, N. E. B. Cowern, F. Cristiano, P. Calvo, N. Cherkashin, Y. Lamrani, A. Claverlie; "Time evolution of the depth profile of {311} defects during transient enhanced diffusion in silicon"; Applied Physics Letters, vol. 83 (10), pp. 1953-1955, (2003).

21. G. M. Dalpian, P. Venezuela, A. J. R. da Silva, A. Fazzio; "Ab initio calculations of vacancies in Si_xGe_{1-x}"; Applied Physics Letters, vol. 81 (18), pp. 3383-3385, (2002).

22. A. Brelot, "Selective trapping of vacancies", Proceedings Defects in Semiconductors, pp.191-201, (1972).

Chapter 7

Conclusions and Future Work

In this work a growth process suitable for $Si_{1-x}Ge_x$ heterojunction bipolar transistors (HBT) has been developed controlling both n- and p-type dopants in a single growth step. Control of the Si starter (collector) layer doping concentration was achieved by altering the growth temperature and the phosphine gas flow. The boron tailing edge into the Si cap (emitter) was removed by interrupting the growth with a 350sccm hydrogen flow for 5 minutes after the $Si_{1-x}Ge_x$ (base) layer growth but prior to the Si cap (emitter) layer growth. A $Si_{1-x}Ge_x$ HBT structure with a $Si_{1-x}Ge_x$ layer width of 31nm and a boron profile width of 22nm was obtained. The layer thicknesses were compared using three different analytical techniques secondary ion mass spectroscopy (SIMS), transmission electron microscopy (TEM) and spectroellipsometry (SE) and reasonable agreement was obtained.

A study of the effect of varying F^+ implantation energy on boron thermal diffusion and boron transient enhanced diffusion (TED) in $Si_{0.86}Ge_{0.14}$ has been undertaken. It has been shown that a high energy fluorine implant completely suppresses boron transient enhanced at 950°C, whereas a low energy fluorine implant gives no suppression of boron TED. Furthermore, a high energy fluorine implant also suppresses thermal diffusion by 44% at 1025°C. The suppression of boron transient enhanced diffusion and thermal diffusion by a high energy F^+ implant is explained by

the location of the boron marker layer in the vacancy-rich region of the fluorine implant damage profile and the lack of any TED suppression for the low energy fluorine implant is explained by the location of the boron marker layer in the interstitial-rich region of the fluorine implant damage profile. Isolated dislocation loops are seen in the $Si_{0.86}Ge_{0.14}$ layer of the sample given a high energy F^+ implant. These loops are in the vacancy-rich region of the fluorine implant damage profile and we postulate that they are due to partial relaxation of the metastable $Si_{0.86}Ge_{0.14}$ layer.

A study has been made of the effect of a high energy F^+ implant with doses in the range $5\times10^{14}cm^{-2}$ to $2.3\times10^{15}cm^{-2}$ on the diffusion of boron in silicon. In samples implanted with P^+ and F^+, the fluorine ($2.3\times10^{15}cm^{-2}$) completely suppresses boron transient enhanced diffusion. For F^+ doses of $5\times10^{14}cm^{-2}$ and $9\times10^{14}cm^{-2}$ the fluorine implant does not reduce the boron thermal diffusion, whereas for F^+ doses of $1.4\times10^{15}cm^{-2}$ and $2.3\times10^{15}cm^{-2}$ the fluorine reduces the boron thermal diffusion coefficient by factors of 1.9 and 3.7 respectively. This reduction of boron thermal diffusion correlates with the appearance of a shallow fluorine peak (depth = 0.07-0.22μm) in the SIMS profile at the same F^+ dose of $1.4\times10^{15}cm^{-2}$. This peak is present in samples with and without the boron marker layer and hence is not due to a chemical interaction between the fluorine and boron. Cross-sectional TEM micrographs show that there are no extended defects at the depth of the shallow fluorine peak, which indicates that it is due to trapping of fluorine at defects too small to resolve by TEM. The shallow fluorine peak is located in the vacancy-rich region of the damage profile, which suggests that it is due to vacancy-fluorine clusters. Analysis of the SIMS profiles suggests that a fluorine concentration after implant in the range $3.6\text{-}6.6\times10^{18}cm^{-3}$ is needed for the vacancy-fluorine clusters to form. The reduction in boron diffusion resulting from a F^+ implant is explained by the presence of the

vacancy-fluorine clusters, which suppress the excess interstitial concentration in the vicinity of the boron marker layer and hence reduce boron thermal diffusion.

A study has been carried out of the effect of fluorine implants with doses in the range $5\times10^{14}cm^{-2}$ to $1\times10^{16}cm^{-2}$ on the transient enhanced diffusion and thermal diffusion of boron in $Si_{1-x}Ge_x$. A reduction of boron thermal diffusion is observed for F^+ doses at and above a dose of $9\times10^{14}cm^{-2}$, whereas a suppression of boron transient enhanced diffusion is observed for all F^+ doses. For F^+ doses of $1.4\times10^{15}cm^{-2}$ and $2.3\times10^{15}cm^{-2}$ the fluorine reduces the boron thermal diffusion coefficient by factors of 2.5 and 3.5 respectively. The reduction of boron thermal diffusion correlates with the appearance of fluorine peaks in the $Si_{1-x}Ge_x$ layer at and above a dose of $9\times10^{14}cm^{-2}$. TEM micrographs show that there are no extended defects in the $Si_{1-x}Ge_x$ layer, and hence it is proposed that the fluorine peaks are due to vacancy-fluorine clusters. The reduction in boron thermal diffusion above the critical F^+ dose is then explained by the presence of the vacancy-fluorine clusters, which suppress the interstitial concentration in the $Si_{1-x}Ge_x$ layer. The suppression of boron transient enhanced diffusion correlates with a deep fluorine peak around the range of the fluorine implant and TEM images show that this peak is due to a band of dislocation loops. The suppression of TED by fluorine is then explained by the influence of the loops in suppressing the backflow of interstitials to the surface. Analysis of the SIMS profiles shows that fluorine is transported from the adjacent silicon into the $Si_{1-x}Ge_x$ layer during anneal, and reaches concentrations that are much higher than observed after implant. This mechanism would give benefits in devices like $Si_{1-x}Ge_x$ HBTs, where the boron profile needs to be confined within the $Si_{1-x}Ge_x$ layer, since a high fluorine concentration is automatically obtained in the vicinity of the boron profile, which maximises the effect of fluorine in suppressing boron diffusion.

The non selective $Si_{1-x}Ge_x$ heterojunction bipolar transistor epitaxial layers growth process developed in this work has been used to grow $Si_{1-x}Ge_x$ heterojunction bipolar transistors device layers (see Appendices C and D for the process listings). These device layers were then implanted with 288keV, $6\times10^{13}cm^{-2}$ P^+ and 185keV, $2.3\times10^{15}cm^{-2}$ F^+. By using two orthogonal half masks, four different regions were created on each wafer; the first having no implants, the second having both P^+ and F^+ implants, the third having a P^+ implant only and the fourth having a F^+ implant only. This will enable us to the study the effect of fluorine implantation on suppressing boron transient enhanced diffusion and thermal diffusion in $Si_{1-x}Ge_x$ heterojunction bipolar devices. The phosphorus implant will cause boron transient enhanced diffusion resulting in boron out diffusing from the $Si_{1-x}Ge_x$ layer and forming parasitic energy barriers which will reduce the collector current and the gain of the transistor. Fluorine implantation should suppress both boron transient enhanced and thermal diffusion and suppress boron out-diffusion from the $Si_{1-x}Ge_x$ layer and hence eliminate the parasitic energy barriers, increasing the collector current and the gain of the devices and also improving the high frequency performance of the devices. This batch is currently being processed in the INNOS cleanroom. See Appendix E for the batch process listing.

Although this work was aimed at bipolar transistors applications, the fluorine implantation conditions developed in this work could also be extended to metal oxide semiconductor (MOS) field effect transistor applications, with the aim of optimising source, drain and extension regions in PMOS devices and the halo regions in n-channel devices.

This work looked at effect of fluorine implantation on boron diffusion in silicon and silicon germanium. It will also be interesting to look at the effect of

fluorine implantation on boron diffusion in other materials such as silicon germanium carbon, strained silicon and strained germanium, which are all of current interest for MOS and bipolar device applications. This work mainly studied boron diffusion, it would also be interesting to study the effect of fluorine implantation on the diffusion of phosphorus and arsenic, which are of current interest for MOS and bipolar device applications.

We saw that the vacancy-fluorine clusters in silicon start to form at a certain critical fluorine dose. Further studies are needed to look at the formation of these clusters and their thermal stability. This could be done by studying the effect of time and temperature on fluorine SIMS profiles. We also saw from this work that the vacancy-fluorine clusters formation is affected by germanium content. Further studies are needed to quantify this effect by studying fluorine diffusion in silicon germanium layers with different germanium contents.

There is still debate in the literature about the mechanisms by which fluorine suppresses boron diffusion in silicon. This work has opened up new avenues by studying the effect of fluorine implantation on boron diffusion in silicon germanium. Hence, there is a lot of work to be done in characterising the effects by which fluorine suppresses boron diffusion in both silicon and silicon germanium and in developing mathematical models for that.

Appendices

Appendix A

ATHENA input file: B diffusion in Si: Pre-processing

This program converts measured SIMS profiles to the program's mesh co-ordinates.

```
go athena
# define grid structure for substrate
line     x location=0.00 spacing=0.10
line     x location=0.10 spacing=0.10
line     y location=0.00 spacing=0.02
line     y location=0.08 spacing=0.002
line     y location=0.20 spacing=0.002
line     y location=0.80 spacing=0.010
#
# initialize substrate
initialize  silicon orientation=100
profile infile= annealed.txt boron
extract name="asgrown" curve(depth,impurity="boron" material="Silicon"\
  mat.occno=1 x.val=0.05) outfile = "annealed.dat"
quit
```

Appendix B

ATHENA input file:B diffusion in Si: Optimisation

This program extracts boron diffusion coefficient Dix.0.

```
go athena
# define grid structure for substrate
line     x location=0.00 spacing=0.10
line     x location=0.10 spacing=0.10
line     y location=0.00 spacing=0.02
line     y location=0.08 spacing=0.002
line     y location=0.20 spacing=0.002
line     y location=0.80 spacing=0.010
#
# initialize substrate
initialize  silicon orientation=100
profile infile= asgrown.txt boron
extract name="asgrown" curve(depth,impurity="boron" material="Silicon"\

  mat.occno=1 x.val=0.05) outfile = "asgrown.dat"
method full.cpl cluster.dam high.conc
set xdelta=0.0001
# Define diffusion parameters
impurity i.boron acceptor silicon Dix.0=1.7e-16 Dix.E=0.0 Dip.0=0.0 Dip.E=0.0

impurity i.boron acceptor silicon Dim.0=0.0 Dim.E=0.0 Dimm.0=0.0 Dimm.E=0.0

impurity i.boron acceptor silicon Dvx.0=0.0 Dvx.E=0.0
impurity i.boron acceptor silicon Dvm.0=0.0 Dvm.E=0.0 Dvmm.0=0.0 Dvmm.E=0.0

impurity i.boron acceptor silicon Fi.0=0.94 Fi.E=0.0
diffus time=    0.50     temp=  1000
extract name="Si" curve(depth-$"xdelta",impurity="Boron" material="Silicon" \

      mat.occno=1 x.val=0.05) outfile="fit.dat"
quit
```

Appendix C

$Si_{1-x}Ge_x$ HBT device layers epitaxy batch (K2157) process listing

B	R	G	No	1	2	3	4	5	6	ID	Description	Coun
										k2157s	HEM - Bulk SiGe HBT on NonN+ with New Mask	
										r1		
										g1	Test for New Mask, NonN+ LOCOS and EPI SiGe HBT	
			1							P-EM	E-BEAM Mask/Reticle Writing	0
			2							G-S12	Title Page: 12 wafers, MATERIAL:N0n N+, 2-3um	12
			3							G-1P	Lithography Notes	12
			4							G-1	Notebook page	12
			5							W-C1	* RCA clean	12
			6							F5-9002P	* Pad oxidation: 900degC, 20nm+- 5nm, O2 + HCl	12
			7							LN-130	* Deposit Si3N4 130nm+-20nm @ 740degC DCS:NH4 1:4, 2.3nm/m.	12
			8							P-GS1	* STEPPER Photolith: reticle K996r A2, Light Field: nom. 1.1um resist STANDARD	12
			9							G-2	* See Engineer for instructions	12
			10							P-RHBD	* Hardbake for dry etch	12
			11							D-N1E	Etch Si3N4. Anisot. L/F EBMF/OPTICAL resist OPT80+ CHF3+Ar	12
			12							X-T1	Nanospec scribe lanes on ? wafers; flat, middle, curve	12
			13							G-2	* See Engineer for instructions	12
			14							P-RS	* Resist strip	12
			15							W-C2	* Fuming Nitric acid clean, 2nd pot only	12
			16							W-C5	* Full S/P Clean (Sulphuric/peroxide, HF, RCA)	12
			17							F6-0	* Furnace 6: Load in N2: LOCOS field oxidation, 1000degC,400nm	12
			18							X-T2	Nanospec thick field oxide on ? wafers; flat, middle, curve.	12
			19							WH-2D2	Dip etch, 20:1 BHF 25degC. 30 seconds (to remove oxide formed on Si3N4)	12
			20							WN-1	+ Strip/Wet etch Si3N4, Orthophosphoric acid 160degC	12
			21							W-C4	* Sulphuric/peroxide clean	12
			22							X-T1	Nanospec scribe lanes on ? wafers; flat, middle, curve.	12
			23							WH-7D1	Dip etch, 7:1 BHF 25degC. To hydrophobic Si + 20secs. IN SCRIBE LANES FEATURES ONLY	12
			24							W-C6	* Pre-epitaxy clean	12
												0
			25							LE-0	Low Pressure Epitaxy; NSEG 700C,Collector: 200nm,1e17n, Spacer:10%Ge 11nm undoped, base 10%Ge 3e19 p26nm, spacers 10%Ge 11nm undoped, LDE 100nm 1e18 ntype (Epitaxy in Machine 1)	6
			26							LE-0	Low Pressure Epitaxy; NSEG 700C,Collector: 200nm,1e17n, Spacer:10%Ge 11nm undoped, base 10%Ge 3e19 p26nm, spacers 10%Ge 11nm undoped, LDE 100nm 1e18 ntype (Epitaxy in Machine 3)	6
			27							X-0	General inspection stage: Inspect all wafers in Nomarski Contrast	12

Appendix D

$Si_{1-x}Ge_x$ HBT device layers epitaxy batch (K2414) process listing

B	R	G	No	1	2	3	4	5	6	ID	Description	Count
										k2414s	HEM - Second HBT batch with new mask and LOCOS	
										r1		
										g0		
			1							P-EM	E-BEAM Mask/Reticle Writing	0
			2							G-S12	Title Page: 12 wafers, MATERIAL: N on N+ , 2-3um thick top n layer,wafer standard thickness	12
			3							G-1P	Lithography Notes	12
			4							G-1	Notebook page	12
			5							W-C1	* RCA clean	12
			6							F5-9002P	* Pad oxidation: 900degC, 20nm+- 5nm, O2 + HCl	12
			7							LN-130	* Deposit Si3N4 130nm+-20nm @ 740degC DCS:NH4 1:4, 2.3nm/m.	12
			8							P-GS1	* STEPPER Photolith: reticle k996r A2, Light Field: nom. 1.1um resist STANDARD	12
			9							G-2	* See Engineer for instructions	12
			10							P-RHBD	* Hardbake for dry etch	12
			11							D-NO1E	Etch Si3N4+PadSiO2. Anisot. L/F EBMF/OPTICAL resist OPT80+CHF3+Ar	12
			12							X-T1	Nanospec non active area regions on 12 wafers; flat, middle, curve.	12
			13							G-2	* See Engineer for instructions	12
			14							P-RS	* Resist strip	12
			15							W-C4	* Sulphuric/peroxide clean	12
			16							F6-0	* Furnace 6: Load in N2: LOCOS field oxidation, 1000degC, 400nm	12
			17							X-T2	Nanospec thick field oxide on 12 wafers; flat, middle, curve.	12
			18							WH-2D2	Dip etch, 20:1 BHF 25degC. 30 seconds. (To remove oxide formed on nitride)	12
			19							WN-1	+ Strip/Wet etch Si3N4, Orthophosphoric acid 160degC	12
			20							W-C4	* Sulphuric/peroxide clean	12
			21							X-T1	Nanospec active area regions on 12 wafers; flat, middle, curve.	12
			22							WH-20D	Dip etch, 200:1 BHF until hydrophobic in AA (to remove pad oxide from active area)	12
			23							W-C6	* Pre-epitaxy clean Just Before EPI	12
			24							LE-0	Low Pressure Epitaxy; NSEG SiGeC HBT structures on Machine 3	12
			25							X-0	General inspection stage	12

Appendix E

$Si_{1-x}Ge_x$ HBTs with F^+ implantation batch (K2649) process listing

No	ID	Description	Count
	k2649s	HEM - New HBT batch wafers from K2157 and K2414	
	r1		
	g0		
1	P-EM	E-BEAM Mask/Reticle Writing	0
2	G-S12	Title Page: 17 wafers, MATERIAL: n on n+ device wafers: K2157 wafers 1 to 12, K2414 wafers 1-5 + 1 blank Si Check wafers (100) n or p type not critical	18
3	G-1P	Lithography Notes	18
4	G-1	Notebook page	18
5	G-3	* Special Instructions Srcibe wafers	18
6	G-2	* See Engineer for instructions inspect under nomarski all wafers	18
	devicefab	Device Fabrication	
		Emitter Window	17
7	W-C1	* RCA clean	18
8	LO-0	* LPCVD LTO. 100nm +- 20nm at 400deg C , all device wafers + 1 blank Si check wafer	18
9	X-T1	Nanospec scribe lanes on 18 wafers; flat, middle, curve.	18
10	P-GS1	* STEPPER Photolith: K996r reticle EW, Dark Field: nom. 1.1um resist STANDARD	17
11	X-I2	Inspect 17 wafers for resist in windows after development.	17
12	P-RHBW	* Hardbake for wet etch	17
13	D-D60	* Descum: 1 min. For OPTICAL resist Technics uWave Asher	17
14	WH-7E1	+ Wet etch oxide, 7:1 BHF 25degC. To hydrophobic Si + 20secs.	17
15	X-I1	Inspect 17 wafers for residue after wet or dry etch.	17
16	P-RS	* Resist strip	17
17	W-C1	* RCA clean	17
18	WH-2D3	Dip etch, 20:1 BHF 25degC. 5 seconds. (Pre-poly depn), All device wafers, + blank Si check wafer	18
			0
		Emitter Poly	0
19	LP-A20	* Amorphous Si deposition: 200nm +-10nm at 560degC 10nm/min	17
20	X-1	Measure specified areas on 17 wafers; flat, middle, curve.	17
21	IA-0	* Implant As+: 1e16, 70keV	17
22	P-GS2	* STEPPER Photolith: K996r reticle EP, Light Field: nom. 2.2um resist (For Si etch>1um or metal)	17
23	X-I2	Inspect 17 wafers for resist in windows after development.	17
24	P-RHBD	* Hardbake for dry etch	17
25	D-D60	* Descum: 1 min. For OPTICAL resist Technics uWave Asher	17
26	D-SP2S	Etch Poly/AmSi. Anisot. on oxides >15nm SYS90 HBr 2 step. (For LF patterns) 50% over etch ** Rinse Wafers in Super Q Leave resist on Wafers**	17
			0
		Base Poly Implant and Definition	0
27	P-RHBI	* Hardbake for implant	17
28	IB-0	* Implant B+: 5 e15, 80kev, all device wafers	17
			0
29	IF-0	* Implant FLUORINE: 185keV, 2.3e15, K2157 #6	1
			0
30	P-RS	* Resist strip	17
31	P-GS1	* STEPPER Photolith k996r: reticle BP, Light Field: nom. 1.1um resist STANDARD	17
32	G-2	* See Engineer for instructions **Check Epi Layer thickness on wafers**	17
33	X-I1	Inspect 17 wafers for residue after wet or dry etch.	17
34	P-RHBD	* Hardbake for dry etch	17
35	D-D60	* Descum: 1 min. For OPTICAL resist Technics uWave Asher	17
36	G-2	* See Engineer for instructions **Check Epi Layer thickness on wafers**	17
37	D-O1E	Etch 100nm SiO2 . Anisot. For L/F EBMF/OPTICAL resist OPT80+CHF3+Ar , all device wafers	17
38	D-SP2S	Etch ~ 600nm PolySi Anisot. short 10% over etch on oxides >15nm stringer not important! SYS90 HBr 2 step. (For LF patterns) Note: Collector Window Exposed at end of etch -no etch stop ALL DEVICE WAFERS	17
39	X-I1	Inspect 17 wafers for residue after wet or dry etch.	17
40	P-RS	* Resist strip	17
			0
		Collector Plug Implant	0
41	P-GS17	* STEPPER Photolith: reticle K996r, Cl , Dark Field: nom. 1.7um resist (For implant or special)	17
42	X-I2	Inspect 17 wafers for resist in windows after development.	17

B	R	G	No	1	2	3	4	5	6	ID	Description	Coun
			43							P-RHBI	* Hardbake for Implant	17))
			44							IP-0	* Implant PHOS+: 1e16, 60KeV	17))
			45							P-RS	* Resist strip	17))
												0)
											Rapid Thermal Annealing	0)
												0)
			46							W-C1	* RCA clean, K2157 # 1-4, 7,9,10,11,12, K2414 #1-4	13))
			47							LO-600	* LTO deposition: 600nm +- 60nm at 400degC SiH4 and O2 , k2157#1-4,7,9,10,11,12, k2414 #1-4	13))
												0)
			48							P-RF	* Frontspin resist	17))
			49							P-RHB	* Hardbake for D-O or ion-beam mill	17))
			50							D-NOS1	BACK Strip: Si3N4, SiO2 /or PolySi OPT80+ CF4+O2	17))
			51							P-RS	* Resist strip	17))
			52							W-C1	* RCA clean	17))
												0)
			53							RA-0	AG RTA stage : TO BE DECIDED, Wafers k2175 1-6, (n type LDE wafers)	6))
			54							RA-0	AG RTA stage : TO BE DECIDED, Wafers k2175 7-12, K2414 1-5 (p type LDE wafers)	11))
												0)
											STOP TO SEND WAFERS TO BELFAST	0)
			55							G-2	* See Engineer for instructions Wafers: k2157#5,6,8, K2414 #5 to be processed to send to Belfast	4))
			56							W-C1	* RCA clean	4))
			57							LD-N0	PECVD NITRIDE deposition; 250nm	4))
			58							D-N1E	Etch Si3N4. Anisot. L/F EBMF/OPTICAL resist OPT80+ CHF3+Ar	4))
			59							X-I1	Inspect 4 wafers for residue after wet or dry etch.	4))
			60							W-C1	* RCA clean	4))
			61							G-2	* See Engineer for instructions Wafers: k2157#5,6,8, K2414 #5, + blank Si check wafer Send to Belfast	5))
											Contact Windows	0)
			62							P-GS1	* STEPPER Photolith: k996r reticle CW, Dark Field: nom. 1.1um resist STANDARD ALignment Critical (WAFERS NOT SENT TO BELFAST, K2157 #1-4, 7,9,10,11,12, K2414 #1-4)	13))
			63							X-I2	Inspect 13 wafers for resist in windows after development.	13))
			64							P-RHBD	* Hardbake for dry etch	13))
			65							D-O3S	Etch SiO2 Anisot. (For Met to Si conts) OPTICAL resist OPT80+: CHF3+Ar	13))
			66							X-I1	Inspect 13 wafers for residue after wet or dry etch.	13))
			67							P-RS	* Resist strip	13))
												0)
											Metallisation	0)
			68							WH-10D	Dip etch, 200:1 BHF (Pre-metallization)	13))
			69							MS-TNA10	Sputter 1000nm Ti-TiN-Al/Si 1% in TRIKON SIGMA + ARC TIN RESIST PROHIBITED	13))
			70							P-GS2	* STEPPER Photolith: K996r reticle M, Light Field: nom. 2.2um resist (For Si etch>1um or metal)	13))
			71							X-I2	Inspect 13 wafers for resist in windows after development.	13))
			72							P-RHBD	* Hardbake for dry etch	13))
			73							D-MAT1	+ Etch Al, Al/Si and/or Ti . for OPTICAL resist SRS SS1C Cl2+SiCl4+Ar (WHOLE 4" wfrs)	13))
			74							X-I1	Inspect 13 wafers for residue after wet or dry etch.	13))
			75							P-RS	* Resist strip	13))
			76							W-C3	* Fuming Nitric Acid clean, metallised wafers	13))
			77							F9-H42	* Alloy/ Anneal: 30mins H2/N2 420degC 5'N2,30'H2/N2,5'N2.	13))

Appendix F

List of Publications

1. P. Ashburn, H. A.W. El Mubarek, J. M. Bonar, W. Redman-White, "SiGe heterojunction bipolar transistors on insulator"; invited paper, Electrochemical Society Spring Meeting, Washington DC, USA March (2001).

2. H. A. W. El Mubarek, P. Baine, J. M. Bonar, P. Ashburn, H. S. Gamble, S. Hall, "Fabrication and Characterisation of SiGe Heterojunction Bipolar Transistors on wafer bonded SOI"; PREP 2001, Keele, UK, April (2001).

3. S. Hall, A. C. Lamb, M. Bain, B. M. Armstrong, H. S. Gamble, H. A. W. El Mubarek, P. Ashburn, "SiGe HBTs on Bonded Wafer Substrates"; INFOS Italy June 2001, Microelectronic Engineering, vol.59, pp. 449-454, (2001).

4. H. A. W. El Mubarek, P. Ashburn, "Semiconductor Processing", GB patent 0305610.8 (2003).

5. H. A. W. El Mubarek, J. M. Bonar, P. Ashburn, Y. Wang, P. L. F. Hemment, O. Buiu, S. Hall, "Non-selective growth of SiGe heterojunction bipolar transistor layers at 700°C with dual control of n and p type dopant profiles"; presented in the 4th International Conference on Materials for Microelectronics and Nanoengineering MFMN in Espoo, Finland, June 10-12, 2002; Journal of Materials Science: Materials in Electronics, vol. 14, pp. 261-265 (2003).

6. N. Lukyanchikova, N. Garbar, M. Petrichuk, H. A. W. El Mubarek, P. Ashburn, "Noise characterization of bulk and SOI SiGe HBTs"; Symposium on Fluctuation and Noise (FaN'2003), New Mexico, 1-4 June (2003).

7. S. Hall, O. Buiu, A. C. Lamb, H. A. W. El Mubarek, P. Ashburn, "Current crowding effects in SOI-SiGe HBTs with low doped emitters"; Proceedings of the European Solid State Device Research Conference ESSDERC, pp. 303-306, (2003).

8. H. A. W. El Mubarek, P. Ashburn, "Reduction of boron thermal diffusion and elimination of boron transient enhanced diffusion in silicon by high energy fluorine implantation"; Applied Physics Letters, vol. 83 (20), pp. 4134-4136, (2003).

9. H.A.W. El Mubarek, Y. Wang, J. M. Bonar, P. L. F. Hemment, P. Ashburn, "The Effect of Fluorine Implantation on Boron Diffusion in Metastable $Si_{0.86}Ge_{0.14}$"; presented at the 9th International Conference on Electronic Materials, San Francisco, USA, April 12-16, 2004. Materials Research Society Symposium Proceedings, vol. 810, pp. C8.15.1-C8.15.6, (2004).

10. S. Hall, O. Buiu, I. Z. Mitrovic, H. A.W. El Mubarek, P. Ashburn, M. Bain, H. S. Gamble, Y. Wang, P.L.F. Hemment and J. Zhang, "SiGe Heterojunction Bipolar Transistors on Insulating Substrates"; NATO Advanced Research Workshop "Science and Technology of Semiconductor-On-Insulator structures and devices operating in a harsh environment", 25-29 April 2004,

Kyiv, Ukraine, Kluwer Academic Publishers (in press) (2004).

11. H. A. W. El Mubarek, J. M. Bonar, P. Ashburn, "Reduction of boron transient enhanced diffusion in silicon and silicon-germanium by fluorine implantation"; presented at the Silicon Technology and Device Meeting (ISTDM), Frankfurt Oder, Germany, May 16-19th (2004); Materials Science in Semiconductor Processing, ISTDM 2004 special issue, vol. 8, pp.103-109, (2005).

12. H. A. W. El Mubarek, P. Ashburn, "Reduction of boron thermal diffusion and elimination of boron transient enhanced diffusion in silicon-germanium by high energy fluorine implantation"; IEEE Electron Device Letters, vol. 25 (8), pp. 535-537, August (2004).

13. J. H. Neave, X. B. Li, J. Zhang, H. A. W. El Mubarek, P. Ashburn, I. Z. Mitrovic, S. Hall, P. F. Fewster, "GSMBE growth and structural characterisation of SiGeC layers for HBTs"; presented in the International Conference On Molecular Beam Epitaxy, 22-27 August 2004, Edinburgh, UK (2004).

14. "UK technique fixes boron diffusion in $Si_{1-x}Ge_x$"; Electronics Weekly, article 37280, 1st September (2004).

15. O. Buiu, I. Z. Mitrovic, S. Hall, H. A.W. El Mubarek, P. Ashburn, G. D. Dilliway, P.J. Ward, J. Zhang, "Optical characterisation of SiGe and

SiGe(C)alloy layers for heterojunction bipolar transistors: possibilities and limitations"; presented in the Optics and Photonics PHOTON04 conference, 6-9 September 2004, Glasgow Caledonian University, UK (2004).

16. P. Ashburn, H. A.W. El Mubarek, M. N. Kham, "A new approach to boron diffusion suppression in Si and SiGe devices: vacancy cluster engineering using fluorine implantation"; invited paper, 5th International Conference on Materials for Microelectronics and Nanoengineering, 13-14 September, Southampton (2004).

17. J.Zhang, J.H.Neave, X.B.Li, P.F.Fewster, H.A.W. El Mubarek, P.Ashburn, I.Z.Mitrovic, O.Buiu, S.Hall, "Growth of SiGeC layers by GSMBE and their characterization by X-ray techniques"; presented at the Electrochemical Society Meeting: SiGe Materials, Processing and Devices, Honolulu, October 3-8 (2004).

18. H. A. W. El Mubarek, M. Karunaratne, J. M. Bonar, G. D. Dilliway, Y. Wang R. Price, J. Zhang, P. L. F.Hemment, A. F. Willoughby, P. Ward, P. Ashburn, "Effect of fluorine implantation dose on boron thermal diffusion in silicon"; Journal of Applied Physics, vol. 96 (8), pp. 4114-4121, (2004).

19. N. Lukyanchikova, N. Garbar, M. Petrichuk, S. Hall, O. Buiu, I. Mitrovic, H. A. W. El Mubarek, P. Ashburn, "1/f Noise and Generation/Recombination Noise in SiGe HBTs on SOI"; paper submitted to IEEE Transactions on Electron Devices (2004).

20. N. Lukyanchikova, N. Garbar, M. Petrichuk, S. Hall, O. Buiu, I. Mitrovic, H. A. W. El Mubarek, P. Ashburn, "White noise in SiGe HBTs on SOI"; paper in preparation for submission to IEEE Electron Device Letters (2004).

21. I. Z. Mitrovic, O. Buiu, S. Hall, J. Zhang, Y. Wang, P. L. F. Hemment, H. A. W. El Mubarek, P. Ashburn, "Electrical and Material Characterisation of $Si_{1-x}Ge_x$ and $Si_{1-x-y}Ge_xC_y$ Alloys for HBTs"; paper in preparation for submission to Semiconductor Science & Technology (2004).

22. M. Bain, H. A. W. El Mubarek, J. M. Bonar, Y. Wang, O. Buiu, H. S. Gamble, B. M. Armstrong, P. L. F.Hemment, S. Hall, P. Ashburn, "SiGe heterojunction bipolar transistors on bonded SOI incorporating buried silicide layers"; IEEE Transactions on Electron Devices, vol. 52 (3), pp. 317-324, (2005).

23. H. A. W.El Mubarek, M. Karunaratne, J. M. Bonar, G.D.Dilliway, Y. Wang, P. L. F. Hemment, A. F. Willoughby, P. Ashburn, "Effect of fluorine implantation dose on boron transient enhanced diffusion and boron thermal diffusion in SiGe"; paper accepted for publication in IEEE Transactions on Electron Devices (2005).

24. M. N. Kham, H. A. W. El Mubarek, J. M. Bonar and P. Ashburn, "Effect of fluorine on boron thermal diffusion in the presence of point defects"; abstract submitted for The European Materials Research Society (EMRS) conference, France, (2005).

25. I. Z. Mitrovic, O. Buiu, S. Hall, J. hang, H. A. W. El Mubarek and P. Ashburn, "MOS based assessment of SiGeC alloys grown by GSMBE"; abstract submitted to INFOS 2005, (2005).

26. M. N. Kham, H. A. W. El Mubarek, J. M. Bonar and P. Ashburn, "Study of Vacancy-Fluorine Clusters in Silicon by Selective Point Defect Injection"; paper submitted to Applied Physics Letters, (2005).